AQUEOUS TWO-PHASE SYSTEM MICRO-ASSAYS AUGMENTED BY AUTOMATED IMAGE ANALYSIS

A Dissertation
Presented to
The Academic Faculty

By

Cameron Yamanishi

In Partial Fulfillment
Of the Requirements for the Degree
Doctor of Philosophy in Biomedical Engineering

Georgia Institute of Technology & Emory University

December, 2019

AQUEOUS TWO-PHASE SYSTEM MICRO-ASSAYS AUGMENTED BY AUTOMATED IMAGE ANALYSIS

Approved by:

Dr. Shuichi Takayama, Advisor

Department of Biomedical Engineering

Georgia Institute of Technology

Dr. Shu Jia

Department of Biomedical Engineering

Georgia Institute of Technology

Dr.Rabindra Tirouvanziam

Department of Pediatrics

Emory University

Dr. Louise Hecker

Department of Medicine

University of Arizona

Dr. Hang Lu

School of Chemical and Biomolecular Engineering

Georgia Institute of Technology

Date Approved: November 4, 2019

ACKNOWLEDGMENTS

I would like to thank my PhD advisor, Dr. Shuichi Takayama, for providing me with many opportunities to explore open-ended questions, giving me freedom to make and learn from mistakes, and being unendingly optimistic. The research environment of the Shu Lab allowed me to grow as a researcher and to rediscover my curiosity about the inner workings of the world.

I also thank the members of my thesis committee for providing critical insights for many of my projects. Their flexibility and collaborative approach helped smooth my transition when I came to Georgia Tech with the Shu Lab from Michigan.

I would like to thank my co-authors on the papers presented in this thesis. Chapter 1: Ryan Oliver, Taisuke Kojima, Shuichi Takayama. Chapter 2: Joyce Han-Ching Chiu, Shuichi Takayama. Chapter 3: Lisa Eiden, Shuichi Takayama, John Dishinger. Chapter 4: Mintra Tongdee, Midori Maeda, Taisuke Kojima, Rattikan Chantiwas, John Dishinger, Shuichi Takayama. Chapter 5: Stephen Robinson, Shuichi Takayama. Chapter 6: Shuichi Takayama.

I thank all of the people who mentored me and taught me how to approach research questions and perform experiments. In particular, my undergraduate advisor, Dr. Daniel Kamei, played a key role in guiding me to the PhD path. The lessons I learned from him in research professionalism, problem solving, thermodynamics, and mass transport have all permeated into my graduate work. Dr. John Frampton, Dr. David Lai, and Dr. Sasha Cai Lesher-Perez taught me microfluidic fabrication. Although, I strayed away from classical microfluidic channels, the principles I learned in that process led me in new and exciting directions. Dr. Brendan Leung and Dr. Joseph Labuz introduced me to cell culture and biofabrication. Dr. Ryan Oliver taught me a great deal about optics and how to write

software. He also did a considerable amount of the intellectual heavy lifting for our microscope paper.

I thank Mintra Tongdee and Lisa Eiden for their skill and patience pipetting for ELISAs. I also thank all of the students who worked with me while they were undergraduates – Tasdiq Ahmed, Saswat Sahoo, and Alec Pfeffer. Although much of that work did not amount to a publication, they explored interesting ideas with me and many of the concepts tangentially helped with the work presented in this dissertation.

I would like to thank my fiancée, Sarah Deslate, and my family – Pam, Frank, Courtney, and Candace. Their emotional support and regular phone calls helped keep me steady through the ups and downs of disproving hypotheses that I liked or troubles with cells and software not behaving.

I thank my coworkers and the staffs at the University of Michigan, Ann Arbor and Georgia Institute of Technology. They made both places enjoyable, friendly atmospheres to explore scientific ideas. In particular, Kathy McCrumb and Aeryal Herrod kept me and the lab well supplied.

Lastly, I would like to thank all of the funding sources that paid for lab materials, equipment, and my living costs: the Defense Threat Reduction Agency, the National Science Foundation Emergent Behaviors of Integrated Cellular Systems Training Program, the Cellular Biotechnology Training Program, the Graduate Assistance in Areas of National Need Fellowship, the Rackham Biomedical Engineering Fellowship, and Pam & Frank Yamanishi.

TABLE OF CONTENTS

LIST OF TABLES

LIST OF FIGURES

LIST OF SYMBOLS OR ABBREVIATIONS

α-SMA	alpha smooth muscle actin
ALI	Air-liquid interface
ANOVA	Analysis of variance
ATPS	Aqueous two-phase system
BSA	Bovine serum albumin
cAb	Capture antibody
CCD	Charge-coupled device
CMOS	Complementary metal-oxide semiconductor
CV	Coefficient of variation
D	Diffusivity
dAb	Detection antibody
DEX	Dextran
DLCO	Carbon monoxide diffusion capacity
DMEM	Dulbecco's Modified Eagle's Medium
DNA	Deoxyribonucleic acid
ECM	Extracellular matrix
EDTA	Ethylenediaminetetraacetic acid
ELISA	Enzyme-linked immunosorbent assay
FBS	Fetal bovine serum
FDA	Food and Drug Administration
FGM	Fibroblast growth media
FGM-SF	Fibroblast growth media, serum free
FITC	Fluorescein isothiocyanate
FPIA	Fluorescence polarization immunoassay
FRET	Fluorescence resonance energy transfer

FVC	Full vital capacity
FWHM	Full width at half maximum
IC50	Half maximal inhibitory concentration
IFN-γ	Interferon gamma
IgG	Immunoglobulin G
IL	Interleukin
IPF	Idiopathic pulmonary fibrosis
HRP	Horseradish Peroxidase
H_2SO_4	Sulfuric acid
L	Length
LOB	Limit of blank
LOCI	Luminescent oxygen-channeling immunoassay
LOD	Limit of detection
LPS	Lipopolysaccharide
λem	Emission wavelength
λex	Excitation wavelength
MEM	Modified Eagle's Medium
MMP	Matrix metalloproteinase
MWCNT	Multi-walled carbon nanotubes
NaOH	Sodium hydroxide
NHLF	Normal human lung fibroblasts
OCT	Optical coherence tomography
PBS	Phosphate buffered saline
PDGF	Platelet-derived growth factor
PDMS	Polydimethylsiloxane
PEA	Proximity extension assay

PEG	Polyethylene glycol
PIV	Particle image velocimetry
PLA	Proximity ligation assay
PMA	Phorbyl 12-myristate 13-acetate
PVDF	Polyvinylidene fluoride
PSF	Point spread function
qPCR	Quantitative polymerase chain reaction
RMS	Root mean square
ROI	Region of interest
ROS	Reactive oxygen species
RPM	Rotations per minute
RPMI	Roswell Park Memorial Institute
SD	Standard deviation
SLAS	Society for laboratory automation and screening
S/N	Signal to noise ratio
τ	Diffusion time
TGF	Transforming growth factor
TIMP	Tissue inhibitor of metalloproteinase
TNF	Tumor necrosis factor
WEKA	Waikato Environment for Knowledge Analysis

SUMMARY

Aqueous two-phase systems (ATPS) are a quirk of thermodynamics, wherein two immiscible solutions separate into stable liquid phases, containing primarily water. Conveniently, some biomolecules partition favorably into one phase or the other. Recently, these properties have been used for many applications, including micropatterning, purification, target concentration, and reagent segregation.

In this work, we examined a previously under-appreciated property of ATPSs – the spontaneous generation of circulating fluid flow with ATPS micro-droplets. First, we developed and validated a novel imaging modality, stigmatic microscopy, to perform the first 3D measurements of ATPS micro-droplet self-driven circulation. This technique borrows concepts from super-resolution microscopy to identify the 3D positions of fluorescent microbeads from individual image frames. Specifically, the use of a toroidal lens shifts the x-focal plane apart from the y-focal plane, enabling determination of z-position from the point-spread function of the image. We designed the microscope using optical modeling to determine usable lens strengths and distances. After constructing the microscope, we developed software to determine 3D positions of fluorescent micro-beads and link the positions from time frame to time frame to track flow.

Second, we enhanced the performance of an ATPS multiplex immunoassay. In previous work from our lab, antibody pairs are spotted in ATPS micro-droplets to co-localize them, preventing crosstalk between incorrect antibody pairs. We advanced this assay from a manually spotted method to a pre-dried format, wherein one phase of the ATPS is rehydrated by the other. We demonstrated that antibody segregation is maintained throughout the rehydration process. With further consideration of self-driven flow, we reduced assay incubation time drastically, first in a two-wash format and subsequently in a one-wash format. Further examination of the competing ATPS

parameters identified an optimal medium between viscosity, partition behavior, and convective flow.

Third, we extended another ATPS bioassay from our lab – collagen microgel contraction to facilitate research on pulmonary fibrosis, a deadly disease with no effective treatments. The collagen gel contraction assay is a helpful measurement of the wound healing activity of fibroblasts. However, current formats use large numbers of cells, restricting their use with primary lung fibroblast cells, which have limited growth capacity. To address the issue, our lab previously used ATPS to generate microscale bioprinted collagen gels and demonstrated proof-of-concept with cell lines. However, the behavior of primary cells proved more difficult to study, due to small effect sizes. To overcome this obstacle, we incorporated higher throughput and use continuous imaging (as opposed to end point assays). This yielded a markedly more reliable assay, which we used to observe the effects of current and potential therapeutics. Notably, we identify differences between normal and diseased fibroblasts in their contraction kinetics at moderate doses of anti-fibrotic drugs.

CHAPTER 1: Stigmatic microscopy enables low-cost, 3D, microscale particle imaging velocimetry in rehydrating aqueous two-phase systems

1.1 INTRODUCTION

Aqueous two-phase systems (ATPS) can form when immiscible polymers are mixed in water. In these systems, many cells and biomolecules partition preferentially and predictably into one phase or the other (10). These characteristics enable separation and compartmentalization of biomolecules (11-13). ATPS-assisted immunoassays have harnessed these characteristics to address several emerging applications such as reagent delivery to cells (14), bacterial patterning (15), and sensing (16), and selective immuno-staining of cells (17). They have been designed using dehydrated reagents, which initiate the assay upon rehydration (18, 19). The rehydration process of ATPS droplets may dictate reagent mixing and influence the overall assay performance (20, 21). However, the dynamic behavior of the convection in and out-of-equilibrium in ATPS rehydrating micro-droplets has been difficult to measure (22, 23). Due to this, many ATPS-assisted applications remain in the nascent development phase, lacking consensus design principles. The ability to measure internal convective flow would prove important in the process of forming these principles, thereby enabling many applications to mature.

Flow tracking approaches have been explored for other applications such as particle image velocimetry (PIV), optical coherence tomography (OCT) and confocal microscopy. PIV has been utilized to deduce the trajectory of a 2d flow by tracking beads within the flow as they are scanned using a light sheet (24). Two-camera PIV further enables 3D tracking, though it is somewhat limited by the necessary multiple viewing angles. At higher resolution, μPIV has been integrated into microscopy systems, but it requires an additional prism system to enable 3D tracking (25). OCT measures the back scattering of coherent light to produce high resolution 3D images (21, 26). Confocal microscopy can produce high resolution 3D images, but the z-

scanning method requires long image acquisition times (27). Spinning disk confocal has somewhat reduced that time. These techniques have all produced remarkable advances in many fields, however it would be attractive to collect 3D information about flow dynamics from a single image on a simple, low-cost laboratory setup.

To address this need we have developed a microscopy technique called stigmatic microscopy which separates the sagittal and tangential focal planes. This is achieved by introducing an astigmatism into the microscopy system. This concept was first proposed by Huang et al. who utilized it to improve reconstruction in super-resolution microscopy (28). We proposed that the optical concept could be adapted at a lower magnification and combined with three-dimensional flow tracking software to study and optimize the flow dynamics in ATPS rehydrating droplets for ATPS-based applications. Here we present the design and validation of the stigmatic microscope, then describe our insights into the flow dynamics of rehydrating ATPS droplets and finally apply this technique to illustrate flow dynamics in a cell exclusion assay (29) and a fast enzyme-linked immunosorbent assay (ELISA) system that we have previously demonstrated for multiplex readouts (19).

1.2 MATERIALS AND METHODS

1.2.1 Modeling stigmatic microscope parameters

As introduced before, it would be attractive to measure the convective mixing inside of a rehydrating droplet in real time. This would enable the indirect measurement of the forces in the droplet that drive convective rehydration. These forces cannot currently be measured. Here we introduce stigmatic microscopy, a microscopy technique in which astigmatic aberrations in the imaging system are used to determine the vertical position of an object relative to the focal plane (Figure 1.1A). When combined with bead tracking in the x- and y- directions, we can track a bead in three-dimensions as it is carried by flow inside a droplet.

Astigmatism occurs when an oblique bundle of rays impinges a lens that does not have a symmetrical front (30). The resulting image appears foreshortened in the

plane of incidence (tangential plane) and elongated in the sagittal plane. The difference between the image points in the tangential and sagittal planes is the astigmatic difference or the aberration called astigmatism. If the astigmatic difference is large, then the image of a bead will appear elongated in the sagittal plane above the focal plane and elongated in the tangential plane below the focal plane. Here we demonstrate that by designing an infinity corrected microscope with a prescribed astigmatism, we can derive a relationship between the position of the bead in the z direction relative to the x-y focal plane and the image of the bead.

Most modern microscopes are designed using an infinity corrected design (30). This term implies that the objective projects the bundle of rays it has imaged as parallel rays. In an ideal system, these would travel to infinity if not for the tube lens, which focuses these rays onto an eye piece or camera (charge-coupled device (CCD), complementary metal-oxide semiconductor (CMOS), or other). To convert an infinity corrected design into a stigmatic microscope, a toroidal lens is inserted between the objective and the tube lens (Figure 1.1A). Because a toroidal lens has different focal lengths in the sagittal and tangential directions, it will introduce an astigmatism into the final image.

As shown in Figure A.1.1A, the paraxial layout establishes the focal lengths and overall size of the microscope. The lens system is composed of two lens groups, the objective (Nikon 4X CFI Achromat, NA 0.1) and tube lens (Thorlabs, LJ1516RM), with a stop in between them and an entrance pupil (20 mm) controlled by the objective. There is also a doublet relay lens (Thorlabs, AC254-050-A) to alter the magnification of the image onto the camera. Here f1 is the focal length of the objective, f2 is the distance between the tube lens and the relay lens, f3 is the distance between the relay lens and the camera, and *d* is the distance between the objective and the tube lens. They are arranged such that the objective is one focal length (50 mm) away from the substrate and the camera is 86.7 mm away from the tube lens. Without the relay lens this distance would be one tube lens focal length (154 mm). To introduce astigmatism,

a half round toroidal lens was inserted into the system 3 mm in front of the tube lens and the system was re-focused using the root mean square (RMS) centroid spot size (49.7 mm). These elements were used as the basis of our idealized model of the optical system.

The paraxial model of the microscope was developed in the optical design software ZEMAX (31). It is important to note that some prescriptions of optical components used in experiments are proprietarily held by Nikon and data on them is unavailable, so the model presented here is for an idealized infinity corrected microscope. As an example of the contribution to astigmatism by the toroidal lens, Figure 1.1B shows the shape of a bead above and below the focal plane when a 1000 mm toroidal lens is used. We demonstrate how the strength of the toroidal lens can be mapped to the distance between the best focus for the sagittal and tangential directions (Figures A.1.1D, A.1.1E). This data is necessary to calibrate the microbead z-position from the image (Figure 1.1C).

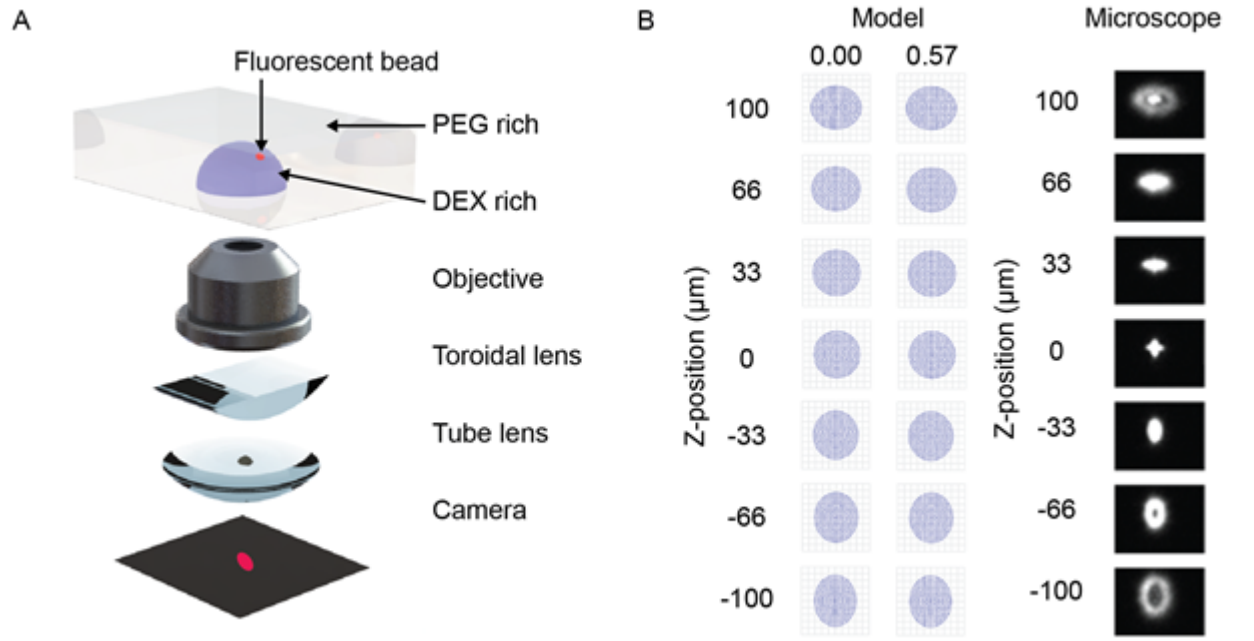

Figure 1.1. Stigmatic microscopy design and model. (A) Diagram showing microscope components. Adapted from Huang 2008 Science. (B) ZEMAX model of stigmatic control under microscope design for two fields (0.00, 0.57) (C) Confirmation of stigmatic imaging on a 3 μm bead when the bead is between -100 μm and 100 μm above and below the focal plane of the microscope.

1.2.2 Constructing stigmatic microscope

For our test microscope, we adapted an inverted Nikon TS100 microscope by inserting off the shelf components from Thorlabs (TTL, a 200 mm tube lens and LJ1703RM, a 1000 mm toroidal lens) as guided by the model. The focal length of the tube lens was chosen to match the Nikon 200 mm focal lengths specified by the company. The microscope was constructed by unthreading the Nikon tube lens and replacing it with the Thorlabs toroidal and tube lenses respectively. The toroidal lens was placed 3 mm in front of the tube lens. Note that the rotational alignment of the toroidal lens with the camera is critical for subsequent analysis.

1.2.3 Calibrating microbead z position

To calibrate the microbead z position from a captured image we measured the astigmatic aberration using an algorithm in Python and the library OpenCV (Figure 1.2A) (32). A single 3 μm yellow-green fluorescent bead was placed in a 96-well plastic

microplate inside a droplet and allowed to settle to the bottom of the well (Figure 1.2B). Images were taken at 5.5 μm intervals from -200 μm below the bead to 200 μm above the bead, then fed into the software algorithm.

The z-calibration loop collected particle height and width for each image, then appended the particle dimensions to an array labeled by z-stack position, as follows. For each image, a threshold was used to generate a binary image. From the binary image, a bounding ellipse was fit to the bead dimensions to find the center of the bead using the built-in functions in OpenCV (33). The particle was found using blob detection and a region of interest (ROI) was used to extract just the particle from the image, as depicted in Figure 1.2B. A line histogram was applied along the x and y axes of the image to project the 2D point spread function of the bead. A spline was fit to the full width at half maximum (FWHM) of the data. The line histogram data was filtered to only include lines two sigma from the mean to filter noise. The distance between the roots of the spline provided the width and height of the bead. This algorithm enables simultaneous detection of multiple beads at multiple z heights from the same image but overlapping beads can interfere with each other.

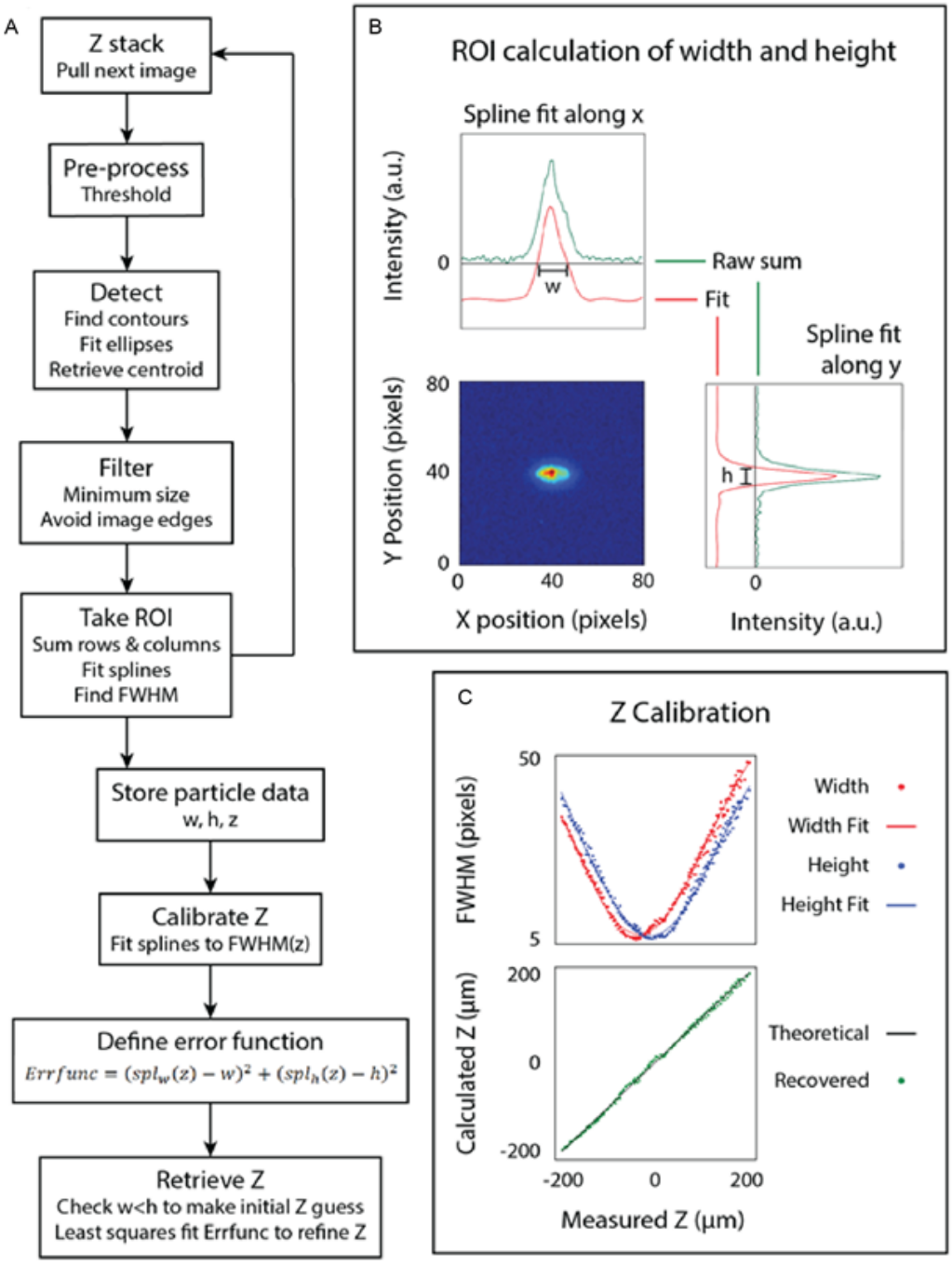

Figure 1.2. Calibration of the microscope. (A) The algorithm used to calibrate the microscope. (B) The point spread function (measured and fit) of a bead. (C) The bead dimensions plotted against the focus position (z) and the final calibrated relationship.

This same technique was applied after imaging at intervals above and below the focal plane to produce a scatter plot of the width and height of the bead at different z positions. The result of fitting a spline to this data is the calibrated relationship of the point-spread function (PSF) of the bead to its position relative to the focal plane of the objective. The z position of an unknown bead can then be calculated using a least-squares fit on the calibrated relationship, which attempts to minimize the error between both the width and height of the bead to the calibrated model. Note that the least-squares fit on the spline function is somewhat sensitive to initial z estimate, so we pre-filtered the z estimate by fitted ellipse area and by width to height ratio. Finally, we plot the measured z-position of several beads to the known z-position of those beads that were back calculated, as shown in Figure 1.2C.

1.2.4 Preparation of DEX – PEG aqueous two-phase systems

Two aqueous two-phase systems were selected, based on prior experience in ATPS micropatterning. Our group has previous published work on the multiplex ELISA and cell exclusion assay using polyethylene glycol (PEG) (MW 35,000, Sigma) and dextran (DEX) (MW 500,000, Sigma) (18, 29). Flows in a PEG and Ficoll (MW 400,000, Sigma) system were also examined. We generated phase diagrams for both systems using a conventional dilution method (34). Briefly, we prepared concentrated polymer solutions in phosphate buffered saline (PBS) (20 % w/w polymer) and mixed the biphasic solutions in a range of different volume ratios. The resulting cloudy mixtures (two-phase) were diluted by a PBS solution until the binodal point where the mixtures turned transparent (one-phase). A univariate spline was fit to the resulting set of points to indicate the binodal curve (34). Separate solutions above the tie-line were prepared to measure the resulting top phase/bottom phase volume ratio. Using the conservation of mass, the volume ratio can be calculated from the ratio of distances between the bulk concentration and either intersection of the tie-line with the binodal curve. Tie-lines were fit to the phase diagram using a custom Python script. A least-squares fit was used to find the slope of the tie-line that matched the volume ratio calculated by

the relative tie-line lengths to the measured volume ratio. The intersection of the tie-line with the binodal curve was found by least-squares fitting between the binodal spline and the tie-line with a fitted slope that passed through the bulk concentration point. Note that the univariate spline does not accurately describe the binodal curve at near-zero values of the independent variable, so an inverse spline was also found and used for the opposite end of the binodal curve, i.e. y(x) for low values of y and x(y) for low values of x. Phase diagrams are included in Figure A.1.2.

We measured convection in rehydrating ATPS that mimics the situation seen in the multiplex immunoassay format (18, 19) and cell exclusion patterning (29). Solutions of the DEX phase in deionized-water were spotted in 1 µL droplets in a clear, flat-bottom 96-well microplate with 3 µm yellow-green fluorescent polystyrene beads (polysciences), diluted to approximately 10-20 particles per µL. The plates were dried in a vacuum desiccator overnight prior to rehydration. DEX microdroplets were rehydrated on the stigmatic microscope with indicated concentrations of PEG in PBS and imaged over indicated times. For flow exclusion studies, beads were diluted to 10-20 particles per µL in the PEG-rich phase to track flow outside of the rehydrating droplet.

1.2.5 Flow tracking

Time course images were collected using Nikon NIS Elements and saved as 16-bit .nd2 files. These files were converted to 8-bit .tiff images, conserving the low intensity region of the data using a FIJI macro. We wrote analysis in Python to calculate 3D bead positions and track their movement (Figure 1.3).

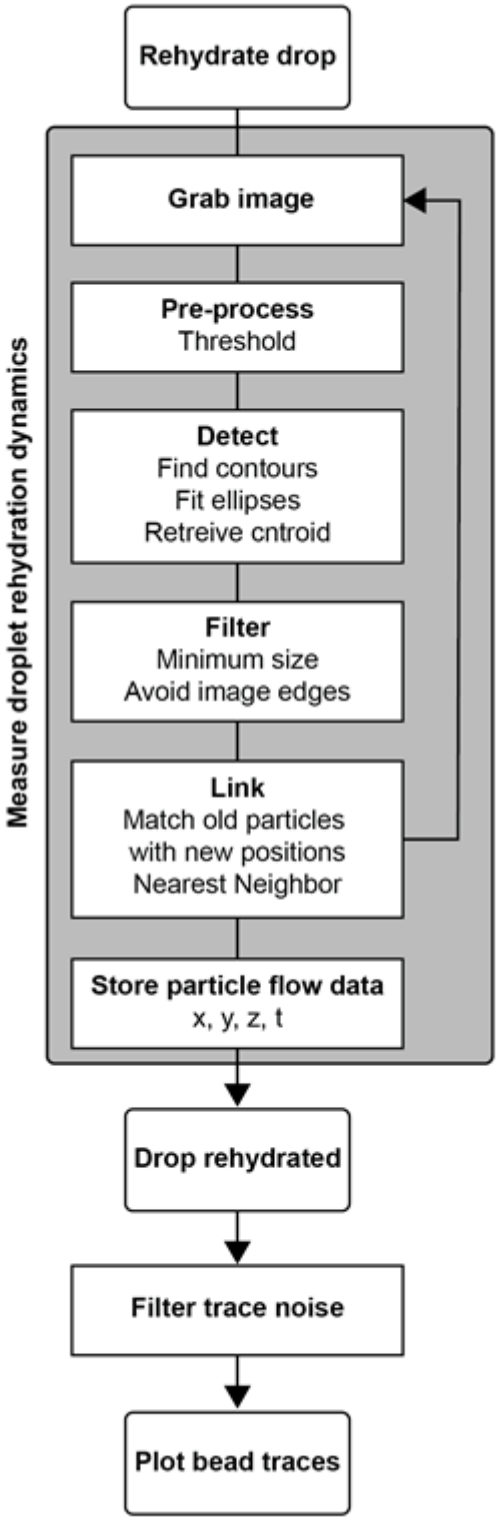

Figure 1.3. Algorithm for measuring droplet rehydration dynamics in stigmatic microscopy. The process for measurement involved rehydrating the drop under microscopic imaging, during which the particles were tracked, and their X, Y and Z positions were reported.

The image thresholding and bead position calculation followed the same algorithm as in the calibration protocol. For each period t, several bead positions were calculated and indexed. Each existing bead was then compared to beads in frame t+1 and linked to the nearest neighbor by x, y, z distance in microns, checking against a maximum travel distance threshold. If a match was found, that bead pair was removed from subsequent matching to prevent flow traces from artificially merging. The remaining beads from period t were similarly matched to the remaining beads in frame t+1. Any beads that were not matched were held for five time frames before terminating that bead path. The resulting flow trace matrix contained x, y, z positions, time points, and bead identity indices. Traces containing fewer than five hundred time points were eliminated as noise.

For flow exclusion studies, the field of view was aligned to contain the outer edge of the droplet. To view the flow at the droplet interface, a 400 pixel (600 μm) slice was taken by filtering the trace data in the y-dimension. The traces were then projected to the x-z plane. Flow traces originating within the general droplet area, defined as a rectangle in the bottom right corner of the x-z plot, were marked as "inside" and pseudo-colored blue. All other traces were pseudo-colored red.

Flow traces were imported to MATLAB and smoothed using a Loess filter in x, y, and z. Once smoothed, the time derivative of 3D distance traveled could be calculated numerically to find particle speed. For the 15-minute traces, the root-mean-square of the speed was calculated for each particle to find a general metric for mixing efficiency. To distinguish between the fast mixing eddy regions and the larger central flow, flow traces were plotted in a 3D interactive diagram using open-source plotly functions, color-coded by time, and examined for annotation. To determine droplet rehydration height, traces were examined in the interactive plots, as well as using x-z projections.

1.2.6 Cell Exclusion

Cell exclusion assays were performed by rehydrating 1 µL DEX drops in which the PEG phase also contained MDA-MB-231 cells (ATCC) to observe if the DEX spotting would exclude the cells from adhering to the spotted region. Three conditions were studied, including a 2.5% PEG-6.4% DEX (w/w) ATPS system, a 2.5% (w/w) PEG only system and Dulbecco's Modified Eagle's Medium (DMEM) system. The DEX was prepared first at 6.4% (w/w) in DMEM F12 (Invitrogen) labelled with fluorescein isothiocyanate (FITC)-DEX (0.1% w/w, Sigma). Each solution was filtered (0.22 µm polyvinylidene fluoride (PVDF) syringe filter) in a sterile environment after the reagents had been prepared and dissolved. The 2.5% PEG-6.4% DEX system was pre-equilibrated by centrifugation at 25°C, 3000 rotations per minute (rpm) for 15 minutes, and the top phase was extracted for cell exclusion experiments.

The DEX solution was spotted in 1 µL drops into clear, flat-bottom 96-well tissue culture microplate using an Integra Biosciences Viaflo 96-well pipetting robot (pipet function, speed 8 with a Z height of 11.2 for the receiving plate) and were dried overnight in the incubator to maintain sterility. The top phase of the 2.5% PEG-6.4% DEX solution or the 2.5% PEG only or DMEM solutions were prepared in DMEM F12 as described above. Cells were resuspended in these solutions at a concentration of 400,000 cells/mL, then added to the dried DEX spot plate to rehydrate the DEX. The cells were stained with NucBlue Live (Thermofisher) according to the manufacturers protocol. The plates were incubated for 2 hrs at 37 °C to allow cell settling, then imaged.

1.2.7 ATPS ELISA

The current work adapts the protocol from our group's previous publication (19) using a human interleukin (IL)-8 DuoSet kit (R&D Systems). ELISAs were performed in custom 96-well injection molded plates with 1.7 mm diameter microbasins (9 per well) (Xcentric Mold & Engineering). Plates were washed with ethanol and distilled water, then dried overnight in a desiccator. Capture antibody (cAb) solutions at the manufacturer recommended concentration in PBS (4 µg/mL) were applied in 1 µL

spots to the microbasins. The plates were sealed and incubated for 90 min to allow adsorption. Free capture antibody was then washed 3x using 200 µL wash buffer (0.05% Tween 20 in PBS), followed by addition of 100 µL of 5% sucrose (Sigma) in PBS for 1 hour to block unused surfaces. The sucrose was emptied, and the plates were dried in a vacuum desiccator for 40 minutes. Once dry, 5% bovine serum albumin (BSA) in PBS was spotted 1 µL per microbasin on top of the IL-8 cAb spots to further block reaction surfaces. The BSA was dried in the vacuum desiccator for 40 min. Detection antibody (dAb) was mixed in solutions of 5% (w/w) DEX MW 500,000 in water (Sigma). These dAb solutions were then spotted 1 µL per microbasin and dried in a vacuum desiccator overnight.

To run the assay, IL-8 standards from the kit were diluted in an assay buffer consisting of 5% (w/w) or 10% (w/w) PEG glycol MW 35,000 (Sigma), 0.05% Tween 20 (Sigma), and 0.5% BSA (Sigma) in PBS (Gibco). An 8-point standard curve was generated with 2-fold dilutions from 2,000 pg/mL in quadruplicate. To avoid biasing the plate by sample addition order in the fast ELISA, samples were loaded onto a feeder plate in a randomized plate layout. The samples were then simultaneously transferred from the feeder plate to the assay plate using the Viaflo 96-well robotic pipet. The assay was initiated upon addition of the PEG-sample solutions, which immediately began to rehydrate the dried DEX and antibody reagents. Samples and standards were incubated in the dark at room temperature for 15 minutes. The plates were washed 6 times with wash buffer to clear out the viscous ATPS components. Streptavidin-horse radish peroxidase (HRP) conjugate (R&D Systems) was added at the manufacturer's recommended concentration and incubated for 20 min. Plates were washed 3x, then filled with SuperSignal ELISA Femto Maximum Sensitivity Substrate (ThermoFisher) and the plates were imaged using a BioRad ChemiDoc MP+ chemiluminescent blot reader.

ELISA plate images were analyzed using a custom ImageJ plugin to outline microbasin regions and calculate chemiluminescent intensity. The standard curve was

plotted using the ggplot2 library in CRAN-R. Analysis of variance (ANOVA) was used to test effects of row, column, ATPS condition, and IL-8 concentration in a randomized plate design with a confidence interval of 95%. Following ANOVA, a posthoc Tukey test was performed with a 95% confidence interval. A linear model was used to fit the data and remove effects from row and column location within the plate to plot the standard curve.

1.3 RESULTS & DISCUSSION

1.3.1 Stigmatic microscope validation

Z-stacks from an individual fluorescent bead indicated that the stigmatic microscope transformed the PSF as expected (Figure 1.2B, Figure A.1.1B). Figure 1.1B shows sample images taken along a stack of z positions, where the spread of light follows the shape predicted in the spot diagram. The 3 μm bead diameter corresponds to 2 pixels in image-space, making it a reasonable approximation for a PSF. Smaller beads were also examined, but the tradeoff between fluorescent intensity and size led to the selection of the 3 μm bead. The 3 μm beads are expected to respond to gravitational force for sedimentation (35) and other forces for convection (36). Generally, smaller beads will be less sensitive to gravitational effects and therefore better for flow tracking. However, small beads contain less dye and have low fluorescent intensity, requiring longer exposure times to capture the shape of the PSF. Exposure can be further tuned to sacrifice depth of field for imaging frequency. For applications examining shallower flows, smaller beads may still be appropriate. In this work, a 500 ms exposure provided sufficient detail about the shape of the PSF to detect z-position within at least the calibrated 400 μm range. Faster flows requiring shorter exposure can be detected by decreasing the exposure time and sacrificing z-range or by introducing a photo-multiplier tube into the system.

After performing the calibration outlined in Figures 1.2A, 1.2B on 3 different beads, the images were fed back into the z-retrieval algorithm to recover z-position. Figure 1.2C indicates accurate recovery of the z-position.

1.3.2 Rehydration dynamics of rehydrating ATPS droplets

Three primary types of flow dynamics emerged during the rehydration process (Figure 1.4A). The first was the volcano current, in which direction of flow is up the center of the droplet. The second is the inverse volcano, in which the current flows down the center of the droplet. We also observed transient micro eddies in high mixing regions where particles would rapidly rotate near the bottom, outer edge of a droplet.

Volcano currents were observed in Ficoll-based ATPS drops while both volcano and inverse volcano currents were observed in DEX-based ATPS drops, depending on specific ATPS composition. Interestingly, the micro eddies were only present in the DEX ATPS drops. Figures 1.4B, 1.4C show an example of a DEX-driven inverse volcano. Fig 1.4B shows the isometric view of particles being tracked in the droplet over fifty minutes. Fig 1.4C shows the side view of the same droplet in which individual beads show a uniform current around the drop. This is just an example of the measurements that are observed using the stigmatic microscope system.

For many applications, knowing the velocity of the current and the cycling rate of the fluid in the drop may be useful for optimizing conditions. Fig 1.4D shows an example of the flow dynamics of a bead in the fluid. The z position of the bead in this example increases in both amplitude and period with time. Moreover, the velocity of the bead shows a double peak pattern after reaching the peak of the drop. The maximum z-position the particle reaches increases with time in this case from 50 μm to 75 μm, and it is inversely proportional to the maximum velocity per flow cycle, as the droplet becomes more well-mixed and loses some of the chemical potential gradient that may be driving flow.

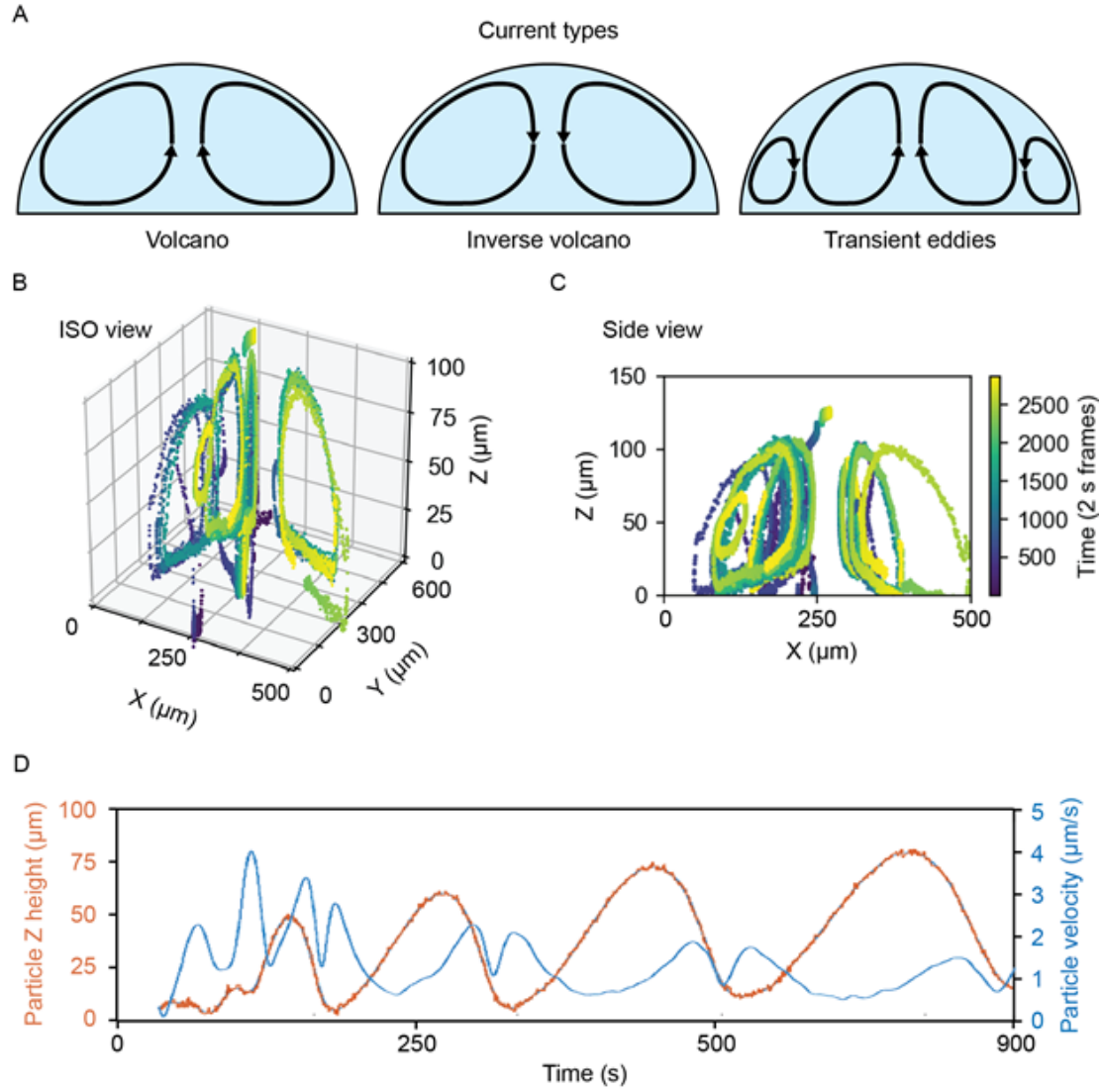

Figure 1.4. Flow dynamics and rates of rehydrating ATPS droplets. (A) Examples of observed flows inside of rehydrating ATPS droplets. (B) 3D plot showing the flow dynamics of an exemplary rehydrating Ficoll-rich droplet. (C) 2D slice of the center of the same Ficoll drop over several flow cycles. (D) Dynamics and rate of rehydration as measured for a drop showing particle positions over time (red) and particle velocity over time (blue) in the drop.

1.3.3 Cell Exclusion

The correlation between flow behavior and rehydrated ATPS cell exclusion patterning was examined. Previously reported experiments indicated a change in cell exclusion efficiency depending on the composition of the ATPS. Therefore, three ATPS conditions were tested (Figure 1.5A): 1 – the extracted top phase from the 2.5% PEG-6.4% DEX system, 2 – a sub-critical ATPS, made of 2.5% PEG, and 3 – cell culture media alone. Note that the sub-critical ATPS contains a small overall concentration of DEX from the dried 1 µL DEX spot. However, that overall concentration of DEX (0.064%) does not bring the total system above the binodal curve. For imaging, the field of view was shifted to include the edge of the droplet to see flow behavior at that region of interest during rehydration, as indicated in Figure 1.5B.

Visual examination of the flow both inside and outside of the droplet added new explanation to the success of cell exclusion patterning. In the two-phase condition, flow tracking within and around the rehydrating droplet indicates a volcano-pattern circulation within the droplet, and a downward/outward flow in the surrounding media (Fig 1.5B). This generates a small stagnant zone at the center of the droplet, which corresponds to the typical location of cells that evade exclusion and attach near the center of the droplet (29). This experiment indicates that convective flow is present and may help drive cell seeding away from the droplet, in addition to the previously hypothesized interfacial exclusion.

In sub-critical ATPS, there is a transient flow exclusion for ~1 hour, while the DEX-rich phase is at a transient, locally high concentration. Over time, the DEX may be diffusing into the bulk phase while the DEX-rich phase is also diluted by infiltrating osmosis, reducing the local concentration below the binodal curve. Temporal analysis of the convective flow paths shows that after ~1 hour, beads settle through the area previously obstructed by the temporary phase boundary. In the absence of PEG, flow consists only of settling straight downward (Figure 1.5B).

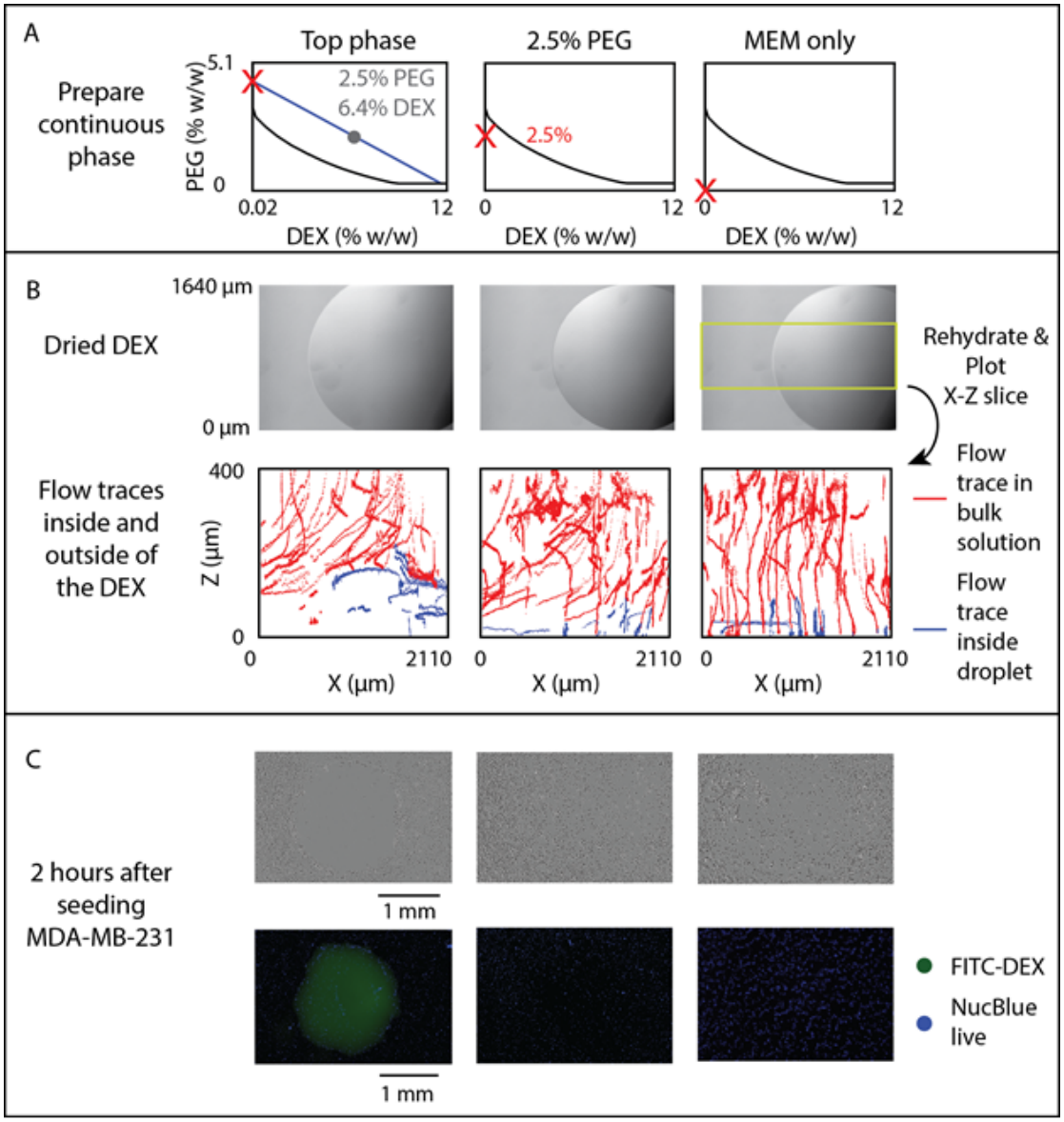

Figure 1.5. Effect of rehydration dynamics on cell exclusion. (A) ATPS solutions indicated by red Xs were used to rehydrate DEX droplets, shown prior to rehydration in panel (B). (B) Flow traces, labeled by trace starting position (inside blue, outside red) were measured and 3D sections indicated by the yellow box were projected to the X-Z plane. (C) Cell exclusion was imaged two hours after seeding MDA-MB-231 cancer cells using phase contrast (top) and fluorescent imaging with FITC-labeled DEX and NucBlue Live Stain (bottom).

The efficacy of cell exclusion correlates with the flow profiles (Figure 1.5C). Representative brightfield and fluorescence images indicate near total cell exclusion in the two-phase condition, but no noticeable exclusion in the sub-critical ATPS or the media-only control. The lack of cell exclusion in the sub-critical ATPS result indicates either that convection alone was insufficient to direct cell patterning, or that cell settling continued to occur beyond the 1 hour of transient exclusion flow.

The difference between the pre-equilibrated two-phase condition and the sub-critical ATPS emphasizes the need for clarity in ATPS research when communicating ATPS concentrations, particularly near the critical point. Some papers describe the overall concentration (mid-tie-line, as in this experiment), while others describe the resulting phases used along the binodal curve.

1.3.4 ATPS ELISA

The impact of ATPS composition on ELISA performance could arise from a variety of factors. These include partition behavior, volume ratio, convective mixing, and viscous limitations on diffusion. The partition coefficient and volume ratio determine the concentrating effect from ATPS (37). Partition coefficients and volume ratios further from unity cause higher concentrations of reagents into one phase, in this case the DEX phase. Techniques already exist to determine partition coefficients, volume ratios, and viscosity, but internal convective mixing has been difficult to measure.

The stigmatic microscope presented here can add missing information regarding convective mixing and transient volume ratio in non-equilibrium ATPS. We examine two ATPS conditions, with low or high PEG concentrations (5% or 10% w/w, respectively) to rehydrate a dried 1 µL droplet of 5% DEX, for overall ATPS consisting of 5% PEG and 0.05% DEX or 10% PEG and 0.05% DEX. We will refer to these conditions as 5% PEG-5% DEX and 10% PEG-5% DEX, respectively. Recent work suggests that convection in non-equilibrium ATPS is driven by a chemical potential gradient (23). The chemical potential gradient is higher for the higher concentration

PEG, which lies on a longer tie-line. However, the resulting concentrations of PEG and DEX in the top and bottom phases are also higher, leading to higher viscosity and associated drag on convective flow.

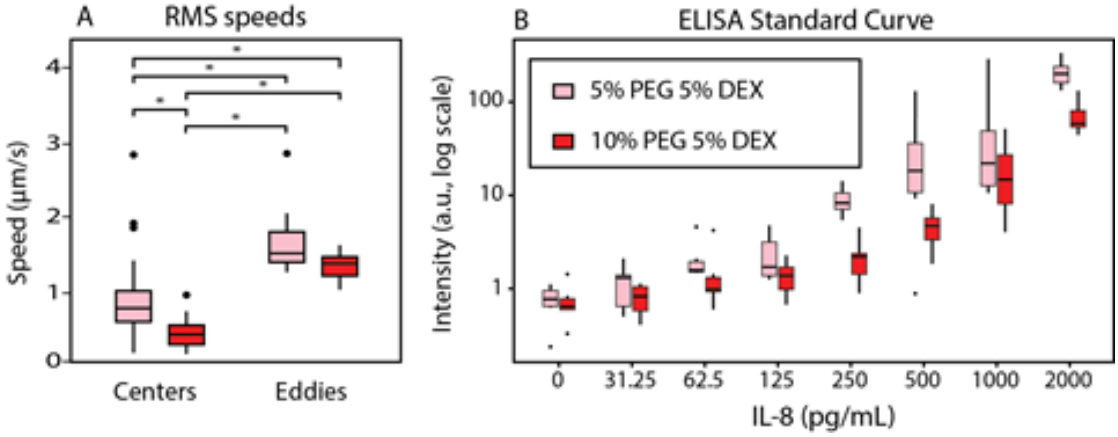

Figure 1.6. Effect of rehydration dynamics on ELISA performance between 5% PEG – 5% DEX (pink) and 10% PEG – 5% DEX (red). (A) Individual speed traces were summarized using their root-mean-square (RMS) values, then plotted in boxplots. *Significant at 95% confidence interval. (B) The standard curve for the row-column-corrected IL-8 ELISA was determined. The difference in signal intensity between 5% PEG-5% DEX and 10% PEG-5% DEX was statistically significant at 95% confidence interval by ANOVA with a posthoc Tukey test.

We quantified spontaneous convective mixing in rehydrating ATPSs. As depicted in Figure 1.4D, flow traces were smoothed in x-, y-, and z- dimensions as functions of time for numerical differentiation to find the speed over time. Speed was then quantified using the RMS velocity to summarize each flow trace into a single measurement. The flow traces were visually examined to annotate each trace as a short eddy or a larger, center flow. The RMS speeds were analyzed between conditions using ANOVA, followed by a posthoc Tukey test at a 95% confidence interval. The center flow was significantly faster for the 5% PEG-5% DEX compared to the 10% PEG-5% DEX, while the difference between eddies did not meet the 95% confidence interval (Figure 1.6A). We suggest that the additional drag effects from viscosity in the 10% PEG-5% DEX condition seem to outweigh its higher chemical potential gradient driving forces.

Overall droplet height was roughly identical for the 5% PEG and 10% PEG conditions (Figure A.1.3). The indistinguishable droplet heights do indicate that potential differences in volume ratio between ATPS conditions are not present. Therefore, differences in ELISA signal may be attributed primarily to differences in convective mixing.

The extensive mixing effect seen in the 5% PEG condition correlated with higher signal intensity in the standard curve of a rehydrated ATPS ELISA for human IL-8. ANOVA with posthoc Tukey test indicated significant that the 5% PEG-5% DEX condition gave higher intensity than 10% PEG-5%DEX at a 95% confidence interval. The row-column corrected standard curve is shown in Figure 1.6C. We suggest that this result occurs because greater internal convection provides more binding opportunities between the detection antibodies confined within the DEX droplet and the IL-8 sample in the bulk PEG-rich phase. The convection also allows additional binding opportunities for the IL-8 sample to the capture antibody on the microplate surface.

Furthermore, we have shown an ELISA with only a 15-minute incubation, 16 times faster than our previously reported protocol (10). This study demonstrates the ability to measure convective mixing using stigmatic microscopy, which will be critical for further analysis and optimization of this short incubation ELISA. These studies will include analysis of other ATPSs and their impact on signal intensity and variation.

1.4 CONCLUSION

The design of the microscope is both simple and flexible, enabling it to be integrated into most off the shelf microscope systems without a deep knowledge of optics. The principle is that a weak cylindrical or toroidal lens (1000 mm or greater) will introduce enough astigmatism to enable stigmatic microscopy but will not interfere significantly with the imaging performance of the system. This provides complementary advantages over other methods (PIV, OCT, Confocal) in that the temporal detail is only limited by the exposure time of a single image. With our particular microscope system,

this worked for 500 ms exposures, but shorter exposures should be possible with a photo-multiplier tube or more sensitive camera. Moreover, because no scanning of a laser or light sheet is necessary, the rate of capture may ultimately be much faster.

The results shown for both ELISA and cell exclusion demonstrate that insights into the performance of ATPS driven assays can be captured using stigmatic microscopy. In ELISA, we found that viscous effects outweigh driving forces, while cell exclusion was found to be controlled by choosing either a critical or sub-critical ATPS condition. Moreover, we demonstrated immunoassay incubation times 16x faster than those previously demonstrated by our group.

Future work will further explore the application of stigmatic microscopy to multiplexed ELISA and will enable the derivation of complete flow fields of the droplet over time. We also believe additional work will enable accurate detection of the droplet shape and morphological changes as required by new applications.

In conclusion, we present a stigmatic microscope designed to enable facile measurement of convective mixing both inside and outside of ATPS droplets. The specific observations as well as general methodology should aid in the development of design principles for various ATPS applications. The ability to conveniently image 3D flows in the μm-mm regime is also envisioned to be useful in understanding the forces and dynamics that drive a number of microfluidic and droplet-based systems beyond ATPS systems.

Chapter adapted from Yamanishi C, Oliver CR, Kojima T, Takayama S. Stigmatic Microscopy Enables Low-Cost, 3D, Microscale Particle Imaging Velocimetry in Rehydrating Aqueous Two-Phase Systems. Front Chem. 2019;7:311 under the creative commons license.

CHAPTER 2: Systems for multiplexing homogeneous immunoassays

2.1 Introduction to multiplex homogeneous immunoassays

The National Institute of Health defined protein biomarkers as “key molecular or cellular events that link a specific environmental exposure to a health outcome.” Understanding the interactions of multiple protein biomarkers of disease will play an integral role in drug screening, in biological pathway analysis, and in disease diagnosis (38). Single-analyte detection has provided high accuracy results, but in a limited scope. Multiplex detection methods, i.e. measurement and analysis of multiple biomarkers together, provide a view of the entire system. Current protein biomarker discovery techniques use mass spectrometry on pooled patient samples, because it provides high-throughput results (39). However, validation of biomarker targets and clinical diagnoses are performed using sandwich immunoassays, due to their high sensitivity and specificity (40). Discrepancies between the two techniques and general challenges associated with performing large scale clinical validations limit the translation of discovered targets to clinical practice (41), resulting in fewer than 2 new protein biomarkers approved by the Food and Drug Administration (FDA) per year (42). Therefore, reliable multiplex immunoassays are needed.

Due to their high sensitivity, specificity, and procedural convenience, this article will focus on homogeneous sandwich immunoassays. Sandwich immunoassays come in two formats: heterogeneous and homogeneous. The standard ELISA is heterogeneous, with cAb immobilized onto a microtiter plate. The addition of dAb forms the antibody-antigen-antibody sandwich complex (43). The requirement for both the cAbs and dAbs to bind to the target reduces noise from non-specific binding (44), making the sandwich format more specific than label-free methods (45-52), which only use one antibody. Unlike heterogeneous immunoassays, homogeneous sandwich immunoassays use both the cAb and the dAb in solution, typically conjugated to an identifiable (encoded) marker. Binding in solution, rather than at a surface, drastically

reduces the distance that antigens must diffuse to reach the antibodies. Combined with the elimination of washing steps, this reduces assay time, making homogeneous assays more suitable for biosensors and assays used in field applications. Additionally, the absence of washing steps allows antibodies with relatively low affinity to be used, because unbinding events do not result in loss of antigens. The soluble format can also provide a more native reaction environment for the antibodies than the surface-bound format, as proteins have been shown to undergo conformational changes when they adsorb to non-native surfaces (53). Most homogenous sandwich immunoassays to date, however, have a major limitation. Because both capture and detection antibody reagents are freely diffusing in solution, it has been difficult to perform spatially segregated reagent multiplexing when performing homogenous immunoassays. The goal of this article is to review the latest methods and techniques to overcome this limitation to enable multiplex homogenous sandwich immunoassays.

Bead-based systems fit in between heterogeneous and homogeneous. These assays replace the planar surface of standard ELISA with microbeads, encoded with identifiers. Bead assays still have faster mixing than standard ELISA, because diffusion time scales as $\tau \approx \frac{L^2}{D}$, where L is the characteristic length and D is the diffusivity; the characteristic length between particles in solution is much smaller than the length between the bulk solution and the surface. However, large beads diffuse more slowly than free antibodies. The Stokes-Einstein relation describes the diffusivity as inversely proportional to radius at constant temperature and viscosity. Immunoglobulin G (IgG) antibodies have radius ~5 nm (54). Adding a bead 1 μm in diameter will therefore reduce the diffusivity by 100-fold.

For the purpose of this review, we strictly define homogeneous immunoassays as those containing all antibodies and antigens in solution, with no washing between antibody-antigen binding steps. This definition will exclude pseudo-homogeneous bead-based assay formats, such as the Luminex xMAP system, which employs

suspension microbeads as a solid phase replacement for planar surfaces (Bead sources). The Luminex system retains some of the assay time advantages of homogeneous systems, but the wash step precludes low affinity antibodies from being used in assays. This is not a problem for biomarkers with well-established antibody libraries, but finding high affinity antibodies for obscure or recently discovered proteins can be difficult. Our selection criteria also exclude microfluidic platforms despite their capacity for automation of washing steps or their shared advantages with homogeneous sandwich immunoassays, including reduced diffusion distances and small sample volume consumption (55-58).

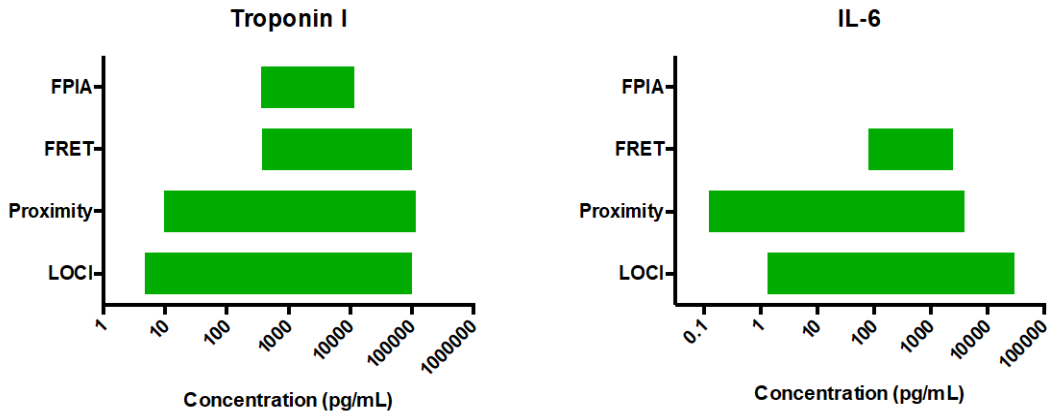

Figure 2.1. Quantitative ranges for homogeneous multiplex assays, compiled from various sources: Troponin I fluorescence polarization immunoassay (FPIA) (59), Flourescence resonance energy transfer (FRET) (60), Proximity (61), and luminescent oxygen-channeling immunoassay (LOCI) from Perkin-Elmer's website; IL-6 FRET from Cisbio Assays' website, Proximity (62), and LOCI from Perkin-Elmer's website.

In this report, we primarily review techniques for multiplexing homogeneous sandwich immunoassays, highlighting the merits and demerits of each. Fluorescent polarization immunoassay employs only the cAb but is included in this scope due to the fact that it is an established and commercially available homogeneous assay. Without performing cross-platform comparison experiments in the same lab, evaluating parameters such as sensitivity and dynamic range can be inconsistent; immunoassay performance depends heavily on user skill and sample handling (63).

However, even comparisons between different labs can provide general metrics of an assay. To normalize as much as possible, we compare assay performance for the same protein targets: troponin I and IL-6, as shown in Figure 2.1.

2.2. Homogeneous multiplex sandwich immunoassay formats

2.2.1. Fluorescence polarization immunoassay

Fluorescence polarization immunoassay (FPIA) is a form of competitive immunoassay. When incident light excites a fluorescently tagged stationary molecule, the resulting emission will be on the same polarized plane as the light source. Conversely, light from a rotating fluorescent molecule will be emitted in a rotated plane. In a free floating solution, large molecules experience less rotation and motion during excitation, and will therefore give off a smaller depolarization whereas small molecules will have larger depolarization. As fluorescent target molecules bind with the antibody, the difference in depolarization can be measured. The immunoassay uses antibodies alongside fluorescently labeled antigen, also known as. tracer. When the tracer binds with antibodies, the whole fluorophore complex is stabilized, thereby reducing motion and allowing for greater polarized emission (64-66). When test samples such as patient plasma or serum are introduced to the system, the patient's target antigen will compete with tracer molecules for the antibodies. The technique is by nature homogenous and compatible with automated detection for high-throughput analysis. However, it is limited to small molecule applications because more dramatic changes in depolarization may be observed with small molecules.

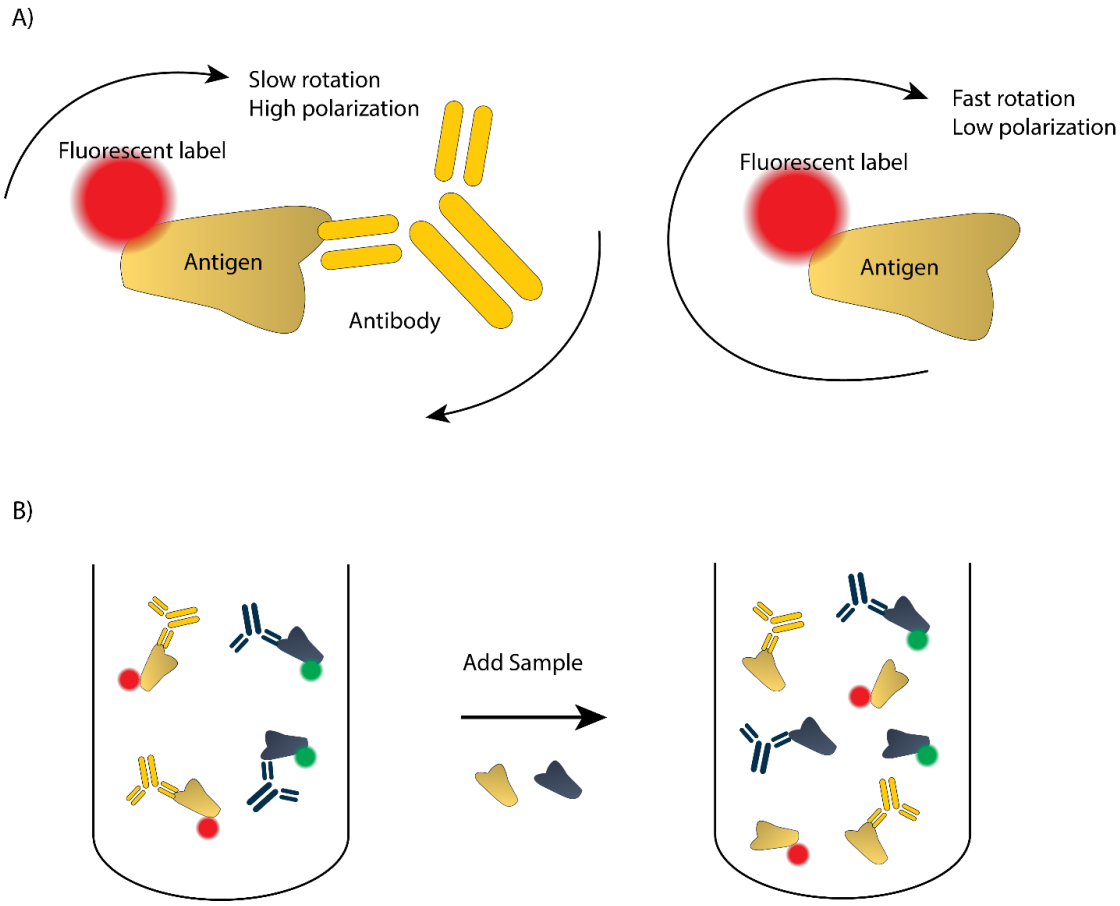

Figure 2.2. Fluorescence polarization immunoassay (FPIA). (A) Polarization intensity in relation to molecule complex size and rotation speed. Figure adapted by author from (66) (B) Schematic representation of multiplex fluorescence polarization adapted by author from (67).

Multiplex FPIA can be achieved by utilizing multicolor quantum dots with narrow emission bandwidths that can be cleanly resolved. This format uses the same principle as single-plex FPIA, wherein the antibody stabilizes the quantum dot to polarize the light. Specifically, a two-plex assay was designed with red and green quantum dots conjugated with tumor biomarkers. The target protein can be identified by the color of the quantum dot, as shown in Figure 2.2. In this method, centrifugation with ultracentrifuge filters of serum samples prior to the assay was necessary to remove matrix proteins to reduce matrix interference. The results of this multiplex assay were shown to have clinical diagnostic value comparable to commercial ELISA (67).

2.2.2. Fluorescence resonance energy transfer

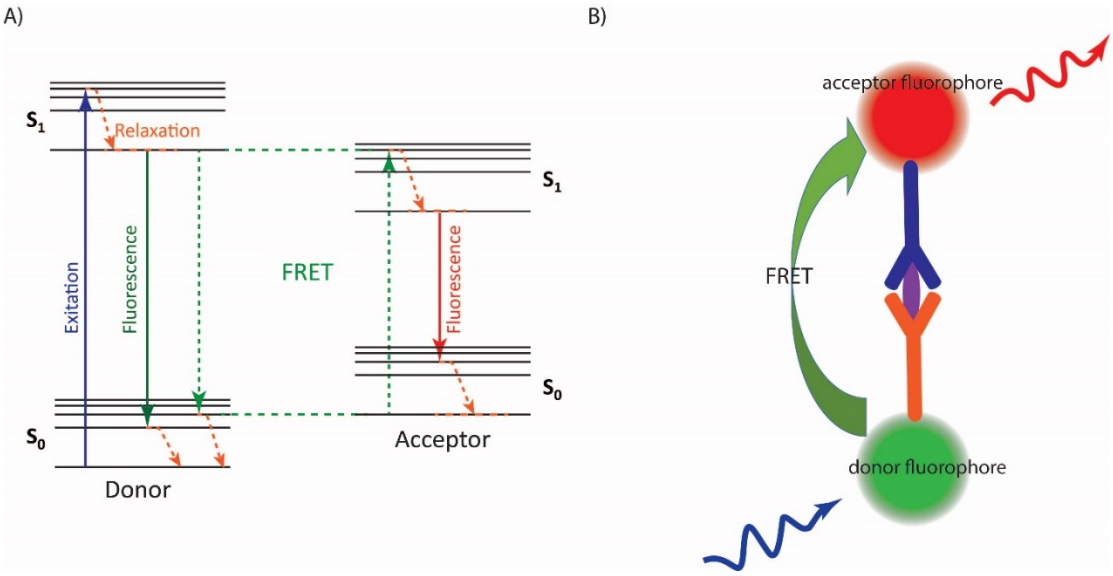

Figure 2.3. Fluorescence resonance energy transfer (FRET) (A) Resonance energy transfer between donor and acceptor (B) FRET applied to immunochemistry. Figure adapted by author from (68).

Fluorescence resonance energy transfer (FRET) based immunoassays utilize a donor-acceptor system, as illustrated in Figure 2.3. When a laser excites the donor fluorophores, the resultant fluorescent energy is transferred from the donor fluorophore to the nearby acceptor molecule, which will subsequently release photons of a different wavelength for detection. The donor and acceptor molecules are both attached to antibodies specific to the target protein. If the target is present, the antibodies can form sandwich complexes with the target, keeping their respective donor and acceptor tags in close proximity. Because the efficiency of energy transfer decreases rapidly as the distance between the donor and acceptor pair increases, the fluorescent signal corresponds to the presence of the target. However, this distance dependence also limits the sensitivity of sandwich immunoassays, due to the relatively large distance across the antibodies and antigens in a sandwich complex (69).

Considerable progress has been made to improve FRET efficiency. The important parameters for FRET efficiency are the quantum yield, extinction coefficients, and spectral overlap (68). The quantum yield and extinction coefficients of both the donor and the acceptor should be high to maximize efficiency. Using

genetic engineering of fluorescent proteins, donor-acceptor pairs can be tuned with large overlap between donor emission and acceptor absorption spectra to increase energy transfer efficiency. On the other hand, undesirable overlap between the donor emission and acceptor emission spectra can be minimized to avoid optical crosstalk.

Although FRET based assays are traditionally built with fluorescent dyes, current research on FRET based immunoassays is dominated by nanostructures made up of nanorods, nanoshells, and quantum dots. These nanostructures make use of the surface plasmon resonance effect to increase FRET signal for higher detection sensitivities. Zhang et al. engineered a quantum dot and gold nanorod two-plex assay to maximize FRET yield (70). Gold nanorods have two distinct plasmon resonances, corresponding to their two dimensions, longitudinal and transverse. Because both dimensions are tunable, gold nanorods are ideal acceptors for multiplex assays. Two different sizes of quantum dots (Cadmium Telluride/Cadmium sulfide core/shell) with two different emission wavelengths were tailored to maximize the overlap of quantum dot donor emission and self-assembled gold nanorods acceptor absorption spectra. This system exhibited high specificity between the two targets, indicating the utility of the FRET pairs in the multiplex system.

2.2.3. Fluorescent Quantum Dots-Graphene Immunoassay

Graphene quenching provides an alternative to FRET. Graphene sheets efficiently quench fluorescence from quantum dots when the two are in close proximity. Therefore, in contrast to FRET, a decrease in fluorescence corresponds to presence of targets in the sample. The primary disadvantage of assays based on energy transfer between quantum dots and nanostructure systems lies in the required donor and acceptor dipole-dipole distance which is limited to 10-100 Å (69). However, graphene sheets are shown to overcome this restriction (71). Compared to a quantum dot-quantum dot pair, the two-dimensional graphene sheets have more possible spatial arrangements in which parts of the sheet are close enough to the spherical quantum

dots to cause quenching, as seen in Figure 2.4. This platform increased the effective distance between the quantum dot anchor and the grapheme anchor from 100 Å up to 223 Å. This distance increase enables greater sensitivity in the sandwich assay formats that use the antigen as a bridge to bring the dAb-coated quantum dot close to the cAb-coated graphene surface.

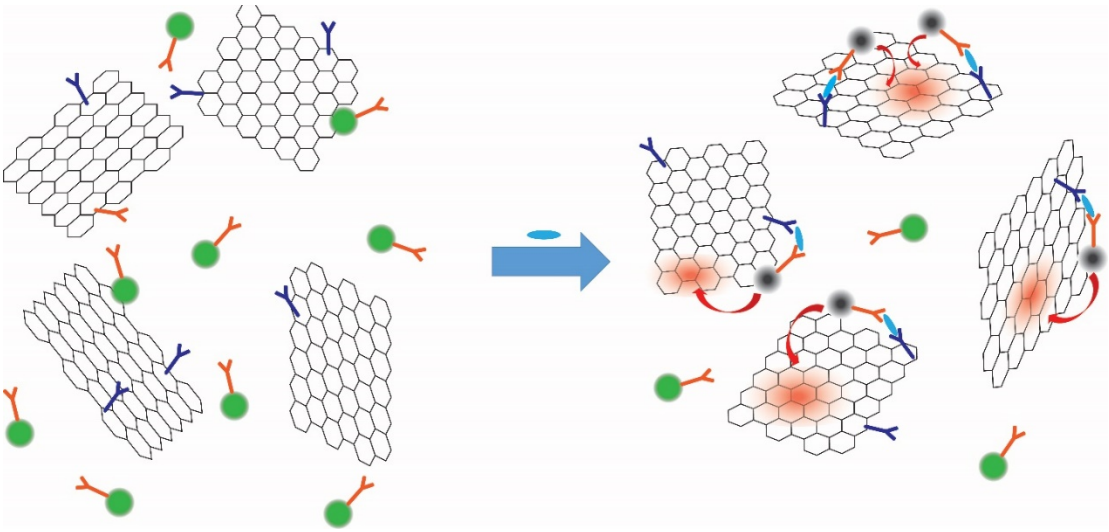

Figure 2.4 Quantum dots and graphene sheets sensor utilizing the fluorescence quenching ability of the graphene sheets to overcome distance dependent limitation of energy transfer techniques. Figure adapted by author from (71).

2.2.4. Luminescent Oxygen-Channeling Immunoassay

The luminescent oxygen channeling immunoassay (LOCI), commercially available as AlphaLISA, from PerkinElmer, uses donor and acceptor beads (250-350 nm diameter) (72). When the donor beads are excited by 680 nm light, they release reactive singlet oxygen. This activated singlet oxygen decays back to its ground state quickly in solution. However, if acceptor beads are nearby, the singlet oxygen molecules can transfer their energy to the chemiluminescent compound in the acceptor beads, triggering the acceptor beads to emit light at 615 (72), as depicted in Figure 2.5. In a sandwich assay format, capture antibodies attached to acceptor beads bind to target proteins in solution. Biotinylated detection antibodies sandwich the target

proteins. Streptavidin-coated donor beads then bind to the detection antibodies to complete the complex. The presence of the target protein thus determines how many donor-acceptor pairs are in close proximity, where they can produce the chemiluminescent signal. The LOCI can perform two-color multiplex immunoassays using a second acceptor bead that is also excited by singlet oxygen and emits at 545 nm. The second donor bead is functionalized with the appropriate antibodies, but contains the same light-sensitive compound as the first donor bead.

The LOCI format is fairly convenient for bench-top research. LOCI assays can be read using a microplate reader equipped with the proper fluorescent channels. For these readers, high laser power is recommended for optimal signal. Additionally, the LOCI format has intrinsic advantages for accuracy. Because LOCI employs a shift from a high wavelength excitation to a lower wavelength emission, it eliminates noise from autofluorescence. Compared to the other optical detection assays, the AlphaLISA assay has a relatively wide dynamic range and low limit of detection for the detection of IL-6 and troponin I, as shown in Figure 2.1.

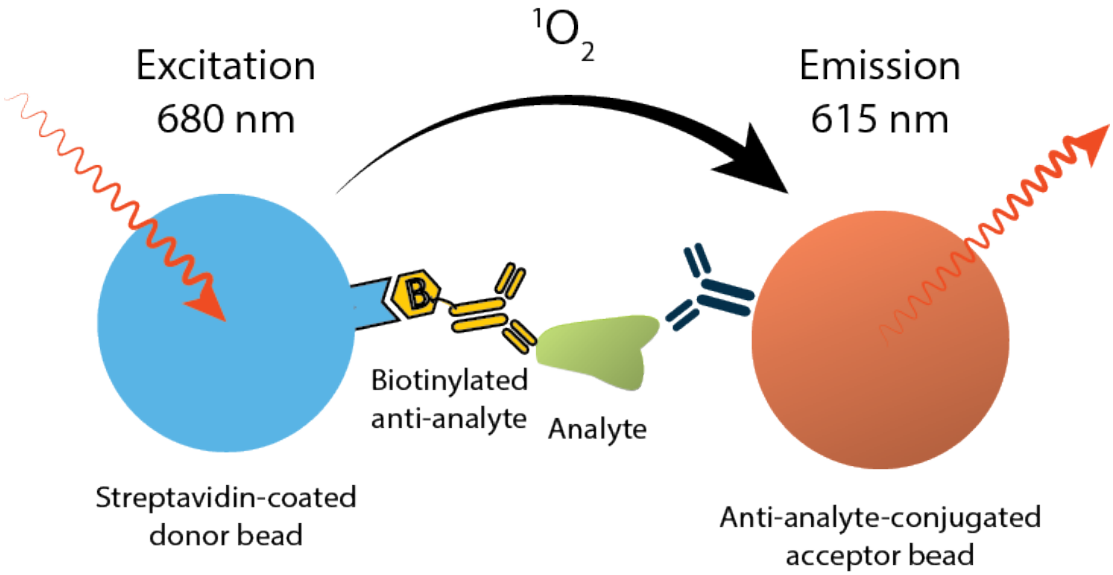

Figure 2.5. Luminescent oxygen-channeling immunoassay (LOCI). In the LOCI format, donor beads are excited by 680 nm light and release singlet oxygen. Acceptor beads in the vicinity emit 615 nm light in response to the singlet oxygen. Figure adapted by author from (73).

Although the commercially-available PerkinElmer system is currently limited to two-plex using chemiluminescence at two different emission wavelengths, higher multiplexing has been demonstrated by spatially arraying reagent solutions using ATPS (74). When two immiscible polymers are mixed in an aqueous solution at appropriate concentrations, they cause separation of the resulting aqueous solution into two phases. These systems are mild to biomolecules, making them appropriate for use in immunoassays. In a PEG-DEX ATPS, antibodies and beads partition preferentially into the dextran phase, allowing spatial confinement of different AlphaLISA bead pairs within different phase-separated droplets within a single well, as demonstrated in Figure 2.6.

The ATPS reagent localization strategy marks a promising development for multiplex assays. The technique is theoretically compatible with other homogeneous immunoassay formats that have not yet been multiplexed, including simple bead agglutination. Additionally, the spatial localization eliminates the possibility of crosstalk between unmatched antibody pairs. Therefore, assay validation does not require the extensive combinatorial screening that many other multiplex techniques must undergo. However, the ATPS method has some drawbacks. The polymers involved are viscous, lowering the diffusivity of reagents and requiring slightly longer assay time. This method also requires specialty plates with topographical features within each well to position the reagent microdroplets from moving within the well. The published 4-plex AlphaLISA assay plate was designed to be compatible with conventional 1536 well format AlphaLISA readers.

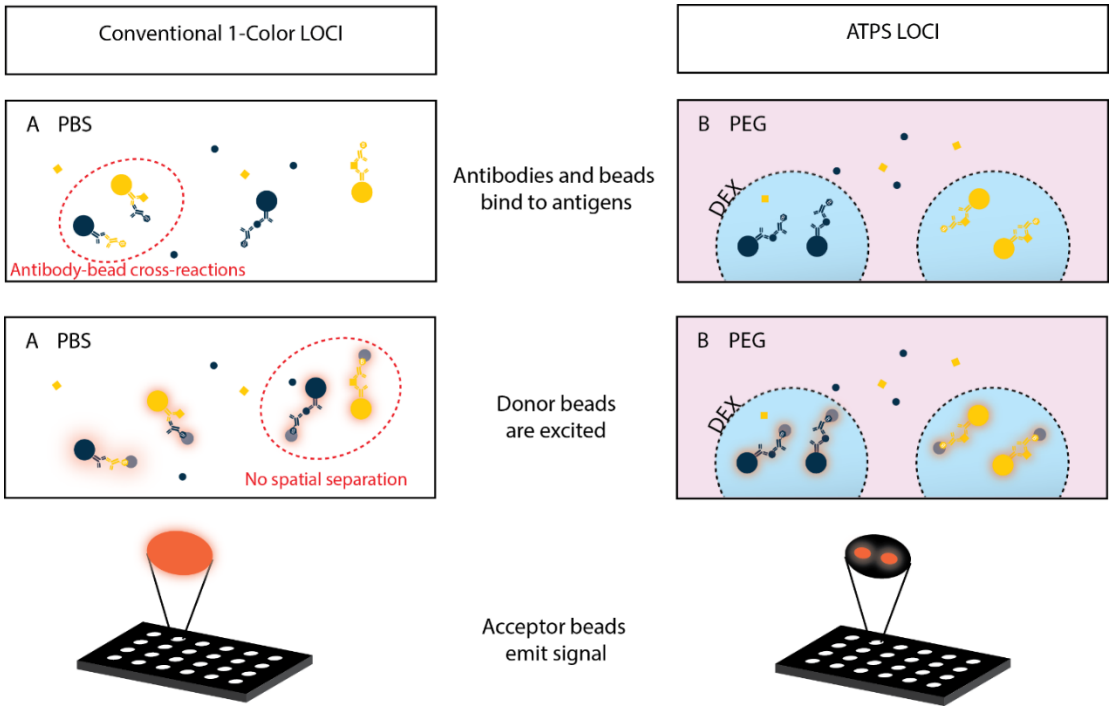

Figure 2.6. ATPS ELISA colocalizes donor-acceptor pairs within dextran (DEX) microdroplets, enabling spatially distinct multiplex detection with a single color. Figure adapted by author from (74).

2.2.5. DNA Proximity

Proximity multiplex formats use deoxyribonucleic acid (DNA) oligomers to encode antibodies. Taking advantage of existing DNA sequencing techniques, the proximity extension assay (PEA) (62) uses antibody pairs attached to DNA oligonucleotides. As shown in Figure 2.7, when the antibodies sandwich the target protein, the DNA oligonucleotides come into close proximity, where the DNA strand from one antibody can hybridize with its complementary DNA strand on the partner antibody. This hybridization allows a DNA polymerase to extend the DNA at both ends. The resulting oligonucleotides can be subsequently amplified by quantitative polymerase chain reaction (qPCR). Only the completed DNA strands, i.e. those which had hybridized and been extended by the DNA polymerase, can be amplified by PCR. Thus, DNA detected by qPCR reflects the presence of the target protein. In multiplex PEA, distinct DNA sequences are used to identify each antibody pair. The PEA

technology is available from Olink, and has been demonstrated in a 96-plex assay (62).

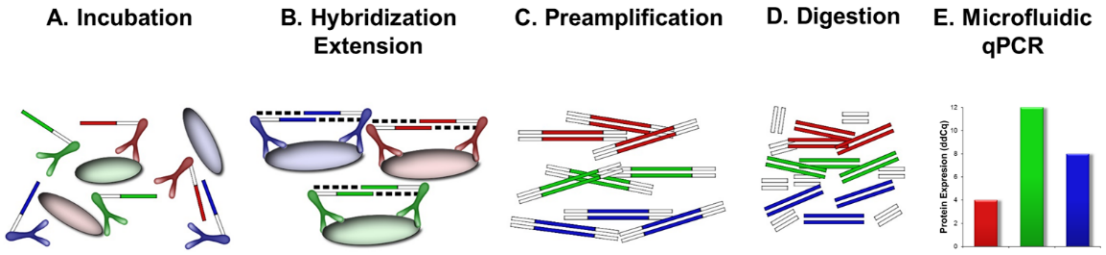

Figure 2.7. DNA proximity assays (A) The proximity extension assay uses antibodies with oligonucleotides in a sandwich format. (B) DNA strands are hybridized with nearby complementary strands. (C-E) Through qPCR, dNA hybridization can be quantified. Reprinted under the Creative Commons Attribution license from (62) (c) 2014 Assarsson et al.

In a similar format to PEA, the PLA (75, 76) also uses DNA oligomers to encode antibody pairs. Whereas the DNA oligomers in PEA are complementary to each other, the DNA oligomers in PLA do not hybridize with each other. Rather, a third DNA oligomer is added to the solution to bridge the DNA on the antibody pair. To increase the specificity of the assay, one study attached an antibody to the third DNA oligomer (77).

Proximity multiplex immunoassays provide an additional level of protection against cross-reactions because both of the antibodies in the pair contain specific labels, unlike AlphaLISA, which uses the same type of donor bead for both acceptor beads. The proximity immunoassays, however, contain specific oligonucleotides on both the capture and the detection antibodies. Therefore, both specific antibodies must be present to generate a signal. For IL-6, the proximity extension assay has a limit of detection of 0.12 pg/mL. Although Olink offers a 96-plex cardiovascular disease panel, troponin I is not included. However, the proximity ligation assay has been demonstrated to have a limit of detection of 0.4 pM for troponin I. The accuracy advantages of DNA proximity assays come at the cost of increased assay time and complexity. The 96-plex assay required an overnight sample incubation, followed by

DNA hybridization and the qPCR steps. The Olink company has addressed many of the added steps by incorporating their qPCR process into the Fluidigm automated microfluidic PCR reader, the BioMark HD.

2.3. Assay validation

Before implementation, new immunoassays must be validated for their analytical performance, then for clinical validation (78). Such is true for singleplex assays, but there are even more considerations that a multiplex assay must take into account. Potential cross-reactions between both endogenous and exogenous antibodies and proteins may result in over- and under-estimation of protein concentrations and should be screened out. Polyclonal antibodies that are multivalent can compensate for low affinities, but the high specificity of monoclonal antibodies are preferred for reduced crosstalk (79-82). Validation for multiplex assays often involved comparisons with its singleplex counterparts for quality references, but for high number multiplex, other analytical methods, such as batch sampling, have to be employed (44, 62). Intra-assay variability, matching wide dynamic ranges and limit of detections also required careful investigations (83, 84).

Another important consideration for immunoassays is matrix interference. Matrix interference refers to the effect resulted from all sample components had on the analytical quality. This effect can be observed by dilutions of samples with different dilution factor and diluents. Investigation of minimum dilution factor is necessary to avoid quantification errors (85-87). This is especially true in no-wash sandwich immunoassays, where the hook effect, or prozone phenomenon occurs (88). As higher concentrations are measured, the signal will increase, plateau, then decrease in a hook shape. The decrease results from target proteins saturating both the detection antibodies and the capture antibodies, preventing formation of the sandwich complex. The hook effect may be addressed by diluting the sample into the monotonic range of the assay (89). Alternatively, Weinstock et al. have demonstrated that addition of eythylenediaminetetraacetic acid (EDTA) to serum can reduce the hook effect, by

inhibiting the activity of calcium-dependent matrix proteins, such as the complement system (90).

Multiplex immunoassays are particularly susceptible to false positives arising from cross-reactivity (91). Cross reaction can occur in several different ways: antibody-antibody, antibody-antigen, and antigen-antigen. In single-plex ELISAs, antibody pairs are carefully screened and selected, but the number of necessary tests rapidly increases with plexing. Juncker and coworkers performed a combinatorial analysis of possible cross reacting pairs in a sandwich multiplex format (44), and found that the number of liable pairs scales as 4N(N-1), in an N-plex assay. Although these types of reactions may be rigorously screened and eliminated, the upper limit of screening at reasonable cost has been estimated at 50 (92). To address cross-reactivity in planar arrays, aqueous two-phase systems have been employed to confine detection antibody solutions to the volume directly above their corresponding capture site (74).

Some patient samples contain human heterophilic antibodies, i.e. antibodies that bind to many of the animal IgGs used in immunoassays (93). These heterophilic antibodies interfere with the immunoassay to cause non-linearity. Classically, this is detected by measuring serial dilutions to check for linearity. However, protections from heterophilic antibody interference can be built into the assay. These measures include PEG precipitation (94), specialized antibodies (95), and blocking additives (94).

2.4. Conclusion

In this review, we described the principles and state-of-the-art of multiplexing homogeneous sandwich immunoassays: methods of encoding and quantification for FRET, AlphaLISA, and DNA proximity assays. We discussed the need for multiplexing to increase throughput of immunoassays for biological studies and disease diagnosis, as well as the advantages multiplexing provides in sample and reagent consumption. On the other hand, we also acknowledged some of the remaining challenges in the field of multiplex immunoassays: high-throughput validation, matrix interference, cross-reactivity, and some of the workarounds to address these issues. The growing field of

multiplex immunoassays offers many promising methods for high-throughput protein screening, and we expect multiplex immunoassays to assume a significant role in biology and healthcare.

Chapter adapted from Bioanalysis. (2015) 7(12), 1545-1556 with permission of Future Science Group.

CHAPTER 3: Aqueous two-phase system rehydration of antibody-polymer microarrays enables convenient compartmentalized multiplex immunoassays

3.1. Introduction

In multiplex immunoassays, the requirement for reliable reaction compartmentalization often conflicts with the need for convenient sample and reagent dispensing at the point-of-use. Many conventional planar (96-98), bead-based (98-100), and microfluidic (101) multiplex immunoassays resort to bath application of cocktails of all dAb reagents to provide convenience at the cost of higher background signals from potential antibody cross-reactions. Indeed, this disadvantage complicates assay validation procedures and hinders multiplex ELISA from becoming more widely used in clinical settings (78, 91, 102). Water-in-oil droplet systems (103), slip chips (104), colocalization arrays (105), tape array technology , and some microfluidic platforms (106, 107) provide reliable reaction compartmentalization, but require special devices and unconventional, and often inconvenient, sample and reagent handling procedures because these systems are actually performing multiple singleplex reactions.

Recently, the use of water-in-water biphasic systems was demonstrated as a way to compartmentalize immunoassay reagents without using physical walls (18, 74). However, the procedure required tedious dispensing of individual droplets containing detection antibody reagents during the assay at the point-of-use (a 4-plex assay in a 96-well format would require 384 pipetting steps from the user for dAb application alone). Here, we describe a microwell-based multiplex immunoassay where cAb is immobilized and dAb reagents, together with an ATPS-forming polymer, are prearrayed in their dried state. To perform the assay, samples are diluted in a solution containing a second ATPS-forming polymer and are added to prespotted microwells. The sample solution rehydrates each reagent spot to autonomously form an array of

water-in-water droplets. After washing away unbound reagents, microwells are ready for signal readout.

Figure 3.1A illustrates the successful phase separation of a solution including PEG (clear solution) and DEX (blue solution). In Figure 3.1B, this concept of in-well prearraying and storage of dried reagents in DEX (blue spots, top), as well as convenient autonomous formation of compartmentalized water-in-water droplet arrays upon sample solution addition (blue droplets, bottom left), is demonstrated. Notably, reagents and reactions are compartmentalized within each droplet (containment of blue reagent) when ATPS-forming PEG diluent is used (bottom left), but not in its absence (bottom right). The PEG-DEX system was chosen for use with our assay platform because it is well-studied for a variety of separation and purification applications and provides a gentle and stabilizing environment for biological materials (108, 109). Factors influencing the distribution of the different materials are, among others, size and hydrophobicity. As determined by Frampton et al. and Simon et al., the partitioning coefficients for both their protein antigens and antibodies in this water-in-water droplet array system favor the DEX phase (18, 74). This partitioning behavior enables a multiplex ATPS ELISA limiting unwanted dAb interactions during the length of an assay. Additionally, a report from Lee et al. using time-lapse optical coherence tomography to monitor PEG-DEX ATPS droplet rehydration showed that rehydration occurs relatively quickly (21).

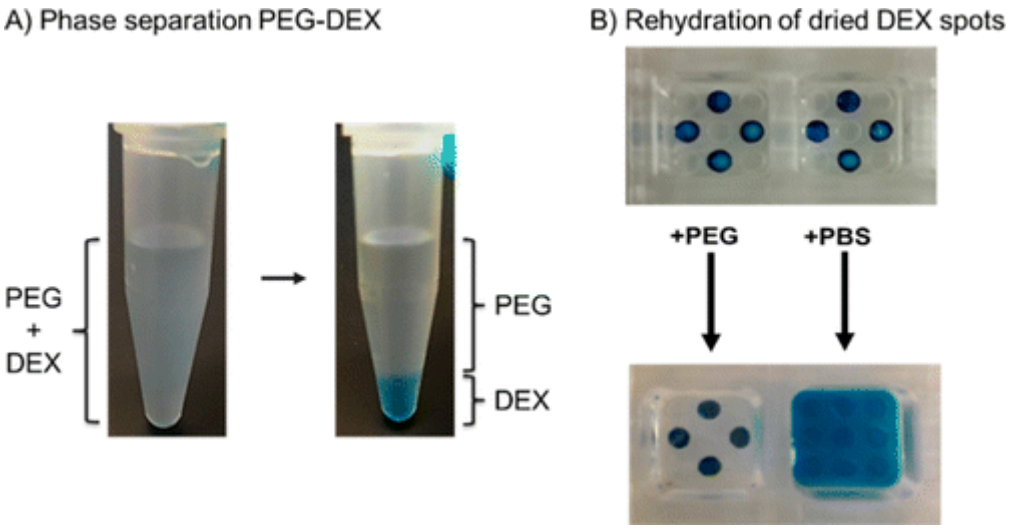

Figure 3.1. Phase separation and rehydration of dried reagent spots to form an array of water-in-water droplets. In a 1.5 mL microtube, a mixture of 9% PEG and 1.5% blue DEX separates into a top (clear PEG) and bottom phase (blue DEX) (A). On a 32-well microplate, blue DEX was arrayed at the bottom of two wells and dried overnight in desiccant (B, top). A solution containing the ATPS-forming polymer PEG was added to the left well which rehydrated the DEX spots and retained the blue DEX in droplets (B, bottom left). The right well was filled with PBS only and was unable to form an ATPS, resulting in a uniform blue color (B, bottom right).

The prespotting of both cAb and dAb required for sandwich assays, together with the ATPS-forming and reagent-stabilizing DEX, provides a robust multiplex immunoassay that reduces unwanted antibody cross-reactions and saves expensive assay reagents. Additionally, end-users are provided a significant convenience through the reduction of pipetting steps. The utility of this platform is demonstrated through quantitative analysis of cytokine [IL-1β, IL-6, IL-8, IL-10, and tumor necrosis factor (TNF)-α] secretions from lipopolysaccharide (LPS)-stimulated ThP-1 cells. The monocytic cell line ThP-1 is a commonly used model system for studying systemic inflammatory response that can differentiate into a macrophage-like state (110, 111).

3.2. Materials and methods

3.2.1. Reagents

All antibodies, protein standards, and streptavidin-HRP were purchased from R&D Systems (human IL-1β DuoSet DY201, human IL-6 DuoSet DY206, human IL-8

DY208, human IL-10 DY217B, and human TNF-α DY210). Chemiluminescence substrate (SuperSignal ELISA Femto Maximum Sensitivity Substrate) was acquired from Thermo Fisher Scientific. Buffers and other reagents were mixed in-house from bulk containers of PBS pH 7.4 (Gibco, Life Technologies, 10010-049), ultrapure distilled water (DNase and RNase free, Invitrogen, Life Technologies, 10977-023), 5× StabilCoat immunoassay stabilizer (SurModics), d-sorbitol (Sigma), dextran (DEX, MW 500 000 g/mol, Pharmacosmos), poly(ethylene glycol) (PEG, MW 35 000 g/mol, Aldrich), Tween 20 (Sigma), and BSA (Fraction V, Fatty-Acid Free, Nuclease and Protease Free, CalBiochem, Millipore).

3.2.2. Multiplex Assay Plate Preparation Procedure

All experiments were performed using custom-designed, 32-well clear polystyrene plates (Figure A.3.1A). Well layout and spacing was based on 96-well microplate standards from the Society for Laboratory Automation and Screening (SLAS). A 32-well design was chosen to reduce costs for initial method development and proof of concept work. In this design, each well bottom contains nine microbasins in a 3 × 3 array (0.35 mm depth and 1.7 mm diameter) that assist with droplet segregation during assays. Additionally, having fixed droplet locations (and analysis regions) facilitates data analysis by keeping spot alignment consistent from well to well and across plates.

Prior to immobilization, cAb stocks were diluted to working concentrations in PBS. Determination of optimal cAb concentrations is described in the Results and Discussion section. For antibody immobilization, 1 µL of each cAb solution was placed in a different microbasin for each well (Figure A.3.1B). Plates were then sealed and incubated in the dark for 90 min. After incubation, 0.5 µL droplets of 3× StabilCoat (diluted from 5× stock with distilled water) were deposited onto all existing cAb droplets. Plates were then placed under a fan to dry for 20 minutes. After dehydration of the cAb/StabilCoat mixture, 1 µL droplets of a solution containing 5% sorbitol and

15% DEX in PBS were placed in every microbasin containing cAb. After this addition, plates were placed under a fan for another 30 min for a second dehydration step. A final microbasin coating consisted of 0.5 µL droplets of a solution containing detection antibody at working concentration (IL-1β, 200 ng/mL; IL-6, 50 ng/mL; IL-8, 20 ng/mL; IL-10, 75 ng/mL; TNF-α, 400 ng/mL), 10% sorbitol, and 16.67% DEX in 1.67× StabilCoat. Finished plates were stored in a desiccator before use the following day.

All liquid deposition steps were performed with either an electronic pipet (Repeater Stream, Eppendorf) for 1 µL volumes, or a Hamilton syringe (25 µL, model 1702RN, 7654-01) for 0.5 µL volumes. Hamilton syringes were equipped with PB600-1 repeating dispensers (Hamilton, 83700) and 1-in., 26s gauge small hub removable needles (Hamilton, 8646-02).

3.2.3. Cell Culture and Supernatant Preparation

Human monocytic ThP-1 cells, a gift from Dr. Peter Ward, University of Michigan, Ann Arbor, were grown in Roswell Park Memorial Institute (RPMI) 1640 medium (Gibco, Invitrogen) with 50 µM 2-mercaptoethanol (Gibco, Invitrogen) and 10% fetal bovine serum (FBS, Gemini Bioproduct), referred to as “media”. For pro-inflammatory stimulation, the protocol from Lund et al. was followed (110). ThP-1 cells were differentiated with 25 nM phorbyl 12-myristate 13-acetate (PMA, Sigma) in media for 48 hours, which induced the cells to adhere to the tissue culture flask. After PMA differentiation, cells were washed with fresh media and incubated 24 hours. ThP-1 cells were then detached using TrpLE (Thermo Fisher) for 30 min, followed by gentle scraping. Subsequently, cells were seeded in tissue culture plates at a density of 1 million cells/mL in media, and given 2 h to rest. For stimulated ThP-1 cells, lipopolysaccharide from *s. Enterica* (LPS, Sigma) in PBS was added to cell cultures at a final concentration of 100 ng/mL, and incubated for 7 hours. An equal volume of PBS was added to nonstimulated cell media. Cell culture supernatants were collected and

centrifuged at 200 × *g* for 5 min to remove cells, and then frozen at −80 °C for future analysis.

3.2.4. Multiplex Assay Procedure

Sample and calibration diluents contained 9% PEG, 0.5% BSA, and 0.25% Tween 20 in PBS. For assay calibration, a 7-step curve consisting of 1:3 serial dilutions from a “high” standard were prepared. To determine assay sensitivity, a high standard of 1.2 ng/mL was used for each biomarker. For the analysis of cell culture samples, the high standard contained 12 ng/mL IL-8 and 4 ng/mL of each of IL-1β, IL-6, IL-10, and TNF-α. Additionally, these standards contained 10% cell media to reduce any potential bias in the calibration curve caused by matrix effects. Cell culture supernatant samples were thawed, diluted 1:10 in sample diluent just before use, and run in quadruplicate.

To start the assay, calibration standards and samples were added to prespotted wells (80 µL per well). Plates were then sealed and incubated in the dark at room temperature for 4 hours. During sample incubation, spotted DEX/antibody mixtures rehydrate and form a stable ATPS in PEG while antigens in the sample partition into the droplets, allowing for parallel immunoassays in a single well. After sample incubation, wells were washed eight times with 0.05% Tween 20 in PBS. After washing, 80 µL of streptavidin-HRP (diluted from a 200× stock in PBS containing 1% BSA) was added to each well and incubated in the dark for an additional 20 min. After HRP incubation, wells were washed another four times before 100 µL of chemiluminescent substrate (prepared according to manufacturer’s instructions) was added to each well prior to plate imaging.

For antibody diffusion experiments, wells were blocked with 1% BSA in PBS for 1 hour and then washed three times with PBS containing 0.05% Tween 20. Microbasins were spotted with 1 µL of a solution containing 1.67× StabilCoat, 10% sorbitol, 2 µg/mL rhodamine-labeled antibody, and 16.67% DEX and dehydrated

overnight. To visualize antibody diffusion, DEX droplets were rehydrated with either a 9% PEG solution or PBS only while fluorescence images were collected at t = 0 minutes, 15 minutes, 1 hour, and 4 hours using a ChemiDoc MP imaging system (Bio-Rad).

3.2.5. Singleplex Assay Procedure

Singleplex experiments were performed using the custom-designed 32-well plates and the same antibody pairs as described previously. cAb solutions were diluted to working concentrations in PBS (concentrations as determined in titration experiments for the multiplex assay), and 1 µL was spotted into the center microbasin of each well. The plate was covered and incubated overnight at room temperature in the dark. Wells were then washed three times with 200 µL of PBS with 0.05% Tween 20 for each well. Next, plates were blocked with 100 µL of 1% BSA in PBS per well for 1 hour. After plates were washed again, 80 µL of sample was added to each well. Duplicate 7-step calibration curves were created, using 1:3 serial dilutions with a high standard concentration of 1200 pg/mL prepared in 1% BSA in PBS. Protein samples were incubated for 2 hours and then removed using the previously described washing procedure. Detection antibody solutions for each biomarker were diluted to working concentrations (Table A.3.1) in 1% BSA in PBS, and 100 µL was added to each well. After a 2 hour incubation, dAb solutions were removed, wells were washed, and 80 µL of a streptavidin-HRP solution (diluted in 1% BSA in PBS) was added to each well. After a 20 minute incubation, the plate was washed a final time, and 100 µL of chemiluminescence substrate was added to each well before imaging.

3.2.6. Analysis

A Q-View Imager LS (Quansys Bioscience) was used for plate imaging with an exposure time of 400 seconds. Q-View software (Quansys) was used for initial image collection. For image analysis, ImageJ was used to extract signal intensities from each

microbasin, which were used to generate calibration curves. Data was then exported into Prism (Graphpad) and fit to a four-parameter, variable slope curve for calculation of unknown samples. The limit of detection (LOD) was calculated as described in Armbruster et al. (112). Signal to noise ratios (*S*/*N*) are calculated by dividing the mean signal from the high standard (1200 pg/mL) by the mean of the blank.

3.3. Results and Discussion

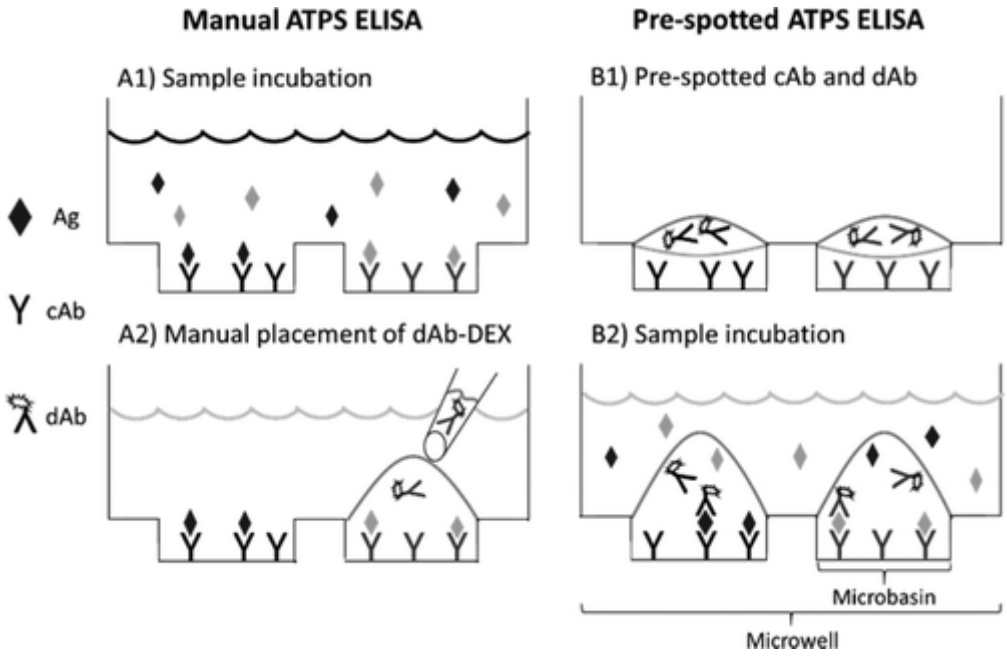

Figure 3.2. Comparison of manual and prespotted ATPS multiplex ELISA methods. Black and gray diamonds represent different analytes (Ag). The hydrated ATPS method involves overnight cAb immobilization and sample incubation (A1) followed by washing and blocking steps. After the analyte has bound to the cAb, wells are filled with a PEG solution, and droplets of dAb/DEX are manually placed on top of each microbasin (A2). The dehydrated ATPS method involves a plate preparation step yielding preapplied and dehydrated cAb and dAb in each microbasin (B1). Sample in a PEG solution can then be added to wells, allowing an ATPS to be formed after the dAb/DEX droplets rehydrate (B2). Antigens partition from the PEG phase into the DEX phase and bind to available antibodies.

Frampton and Simon et al. reported the first planar multiplex immunoassay platforms that effectively prevent reagent-driven cross-talk (18, 74). To accomplish this, dAb incubation was performed using a PEG-DEX ATPS water-in-water droplet

array format rather than the traditional bath, or cocktail, application (Figure 3.2A). Although this allows segregation of antibody pairs, elimination of antibody cross-talk, and generation of a highly reliable assay, it is tedious and difficult for a user to accurately place ~1 μL dAb-DEX droplets in appropriate locations. Here, we describe the preparation and use of an improved ATPS multiplex ELISA procedure in which an assay plate with prespotted and dehydrated reagents is used to simplify assay procedure and reduce potential for user error (Figure 3.2B).

For assay plate preparation, cAb was arrayed and immobilized in wells prior to the addition of a stabilization and blocking additive (Figure 3.3A, 3.3B). Titration experiments were performed to determine optimal cAb concentrations. Specifically, cAb concentrations ranging from 0.5 to 12 μg/mL were immobilized in microwells prior to performing ATPS ELISA. In these experiments, dAb and reference analyte concentrations remained constant (Table A.3.1). Sample results for the cAb optimization tests, shown in Figure 3.3H (TNF-α only), illustrate the typical trend observed in these experiments. Signal increases as more cAb is used because the polystyrene surface is not yet saturated with antibodies, and additional cAb immobilization allows a higher number of antigen molecules to bind. Curves reached an apex before a decrease in signal was observed at higher concentrations. This decrease in signal is likely caused by excess, nonimmobilized antibody that is competing with immobilized cAb for antigen binding. Titration curve apexes were used to determine the optimal cAb concentration for each biomarker, yielding 2 μg/mL for IL-1β, 4 μg/mL for IL-8 and TNF-α, and 6 μg/mL for IL-6 and IL-10.

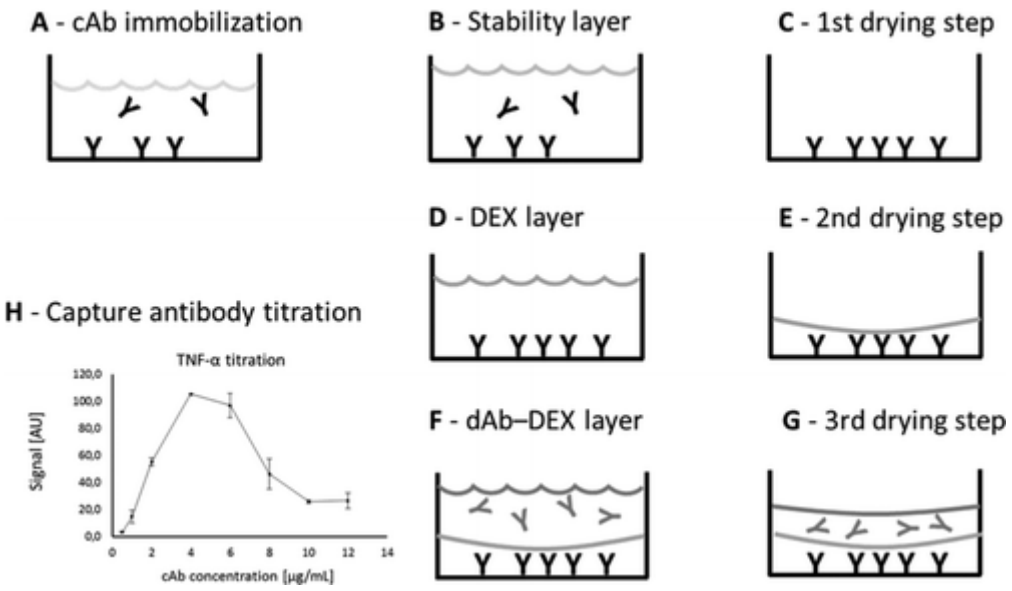

Figure 3.3. Plate preparation procedure and assay optimization results for the prespotted ATPS multiplex ELISA method. Panels A–G represent the different steps performed in a single microbasin prior to running an assay. After cAb (Y) diluted in PBS (gray --) is immobilized at the microbasin bottom (A), stability reagent (gray --) is added (B). The two solutions mix and are dehydrated under a fan (C). A layer of dextran and sorbitol in PBS (gray --) is added (D), which is also dehydrated, indicated by the change in curvature (E). The final coat (gray --) contains dAb (gray Y), sorbitol, and dextran (F), and dehydration occurs in a desiccator overnight (G). Sample data used to determine optimal cAb concentrations shows mean chemiluminescence signal, and the error bars are standard deviations (H). The results (showing only TNF-α cAb titration) are exemplary for all cAb titrations performed which each show an apex between 2 and 6 µg/mL.

The remaining steps illustrated in Figure 3.3 involve the layering of DEX and dAb components. Figure 3.3D illustrates the addition of a DEX solution on top of the cAb/StabilCoat layer. This step provides separation between the already dehydrated cAb and the final dAb/DEX coat to avoid premature cAb/dAb mixing and nonspecific binding potentially causing a decrease in assay performance. The final microbasin coating (Figure 3.3F), consisting of dAb and DEX, also includes sorbitol to prevent aggregation and retain antibody activity after rehydration (113-115). In this study, five spots are in each well and are rehydrated with 80 µL of a 9% PEG solution to give a final DEX concentration of 1.5% in the aqueous system. This combination is above the binodal curve of the PEG and DEX system which is normally required to form the

ATPS(34). After separation the volume ratio of the two phases is 11:1 for the PEG-rich:DEX-rich phases (Figure 3.1A).

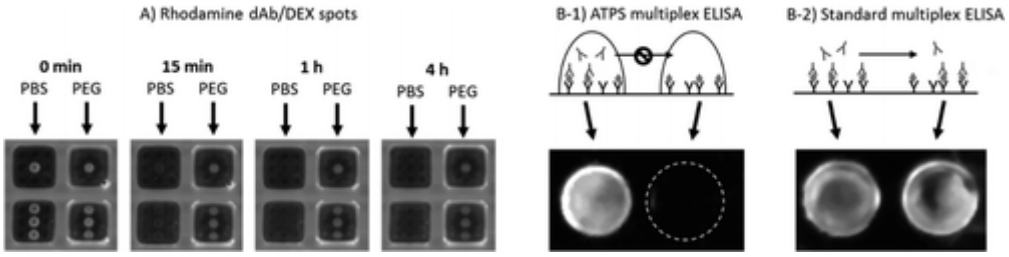

Figure 3.4. Dried and rehydrated DEX phase retains the ability to prevent antibody cross-talk. In a fluorescently tagged antibody diffusion experiment (A), all microbasins that were spotted with rhodamine-dAb produce a fluorescence signal at t = 0. At t = 15 minutes, rhodamine-dAb spots remain clearly visible in the wells with PEG solution added, while those in PBS wells are very faint. After a 1 hour incubation, no spots are visible in the PBS wells. Wells with PEG solution continue to show a strong, confined signal up to 4 hours, corresponding to the assay time for ATPS multiplex ELISA. In a dehydrated ATPS assay (B-1), the left microbasin contained cAb (Y), dAb (gray Y), and dextran, while the right microbasin contained only cAb and dextran. Antigen (gray ⧫) binds to cAb in both microbasins (B-1, top), but signal is only generated from the one that included dAb (B-1, bottom). The standard multiplex ELISA assay (B-2) does not utilize ATPS; bath-applied dAb binds on all available antigen in either microbasin (B-2, top). This leads to a readout in which both cAb spots produce detectable signal (B-2, bottom), illustrating antibody cross-talk.

A key advantage in using ATPS to perform multiplex ELISA is the elimination of antibody cross-talk, as previously demonstrated (18, 74). In the method presented here, ATPS is again used to prevent antibody cross-talk; however, one key difference is that components of the system are dehydrated during preparation and then rehydrated during the assay. To determine effects of the dehydration/rehydration procedure on the ability to confine antibodies to specific droplets and eliminate cross-talk, two different experiments were designed. To confirm dAb confinement, 1 μL droplets of a rhodamine-labeled antibody/DEX mixture were placed in microbasins, dehydrated, and then rehydrated with either PBS or 9% PEG in PBS. Fluorescence images were then taken at t = 0 minutes, 15 minutes, 1 hour, and 4 hours (Figure 3.4A). After 4 hours of incubation, fluorescent dAb was clearly compartmentalized

within rehydrated DEX droplets in wells containing PEG, and had diffused away in wells rehydrated with just PBS.

To specifically confirm elimination of antibody cross-talk using rehydrated ATPS, adjacent microbasins in a single well were prepared with the aforementioned cAb/DEX/dAb layering procedure (Figure 3.3A–F). One spot contained both cAb and dAb/DEX, while the other included only cAb and DEX without dAb. After rehydration and completion of an assay, signal was only detected from the microbasin with both cAb and dAb (Figure 3.4B-1). When a traditional ELISA protocol was performed (involving bath application of dAb) using the same antibody pairs and arrangement, signal was produced by both microbasins (Figure 3.4B-2). These results demonstrate that, after rehydration of DEX, dAb remains confined within the microbasin for the entire duration of the assay, and any small amount of dAb partitioning into the PEG phase is insufficient for creating false positive signals in adjacent microbasins. Furthermore, signal intensity in the positive microbasin was comparable between ATPS and standard bath methods, despite the need for 80× more dAb by mass in the standard ELISA protocol.

To test the utility of this method, quantitative analysis of five cytokines (IL-1β, IL-6, IL-8, TNF-α, and IL-10) was performed. This panel was chosen because these cytokines are involved in a variety of immune system functions, and have been linked to a range of diseases such as cancer (116-118), psoriasis (116, 118, 119), and rheumatoid arthritis (116, 118). Sample calibration data for this assay is shown in Figure 3.5A–E. LOD and *S*/*N* values for this new spotting procedure were compared to the manual multiplex ATPS method described by Frampton et al (18) as well as singleplex ELISA (curves not shown) for each biomarker (Table 3.1). The LOD is comparable between the three methods for all five cytokines in this study. A decrease in signal-to-noise ratio was observed for IL-1β and IL-8 using dehydrated ATPS compared to that of previously reported methods. The change in *S*/*N* comes from

increased background signal that may be the result of unwanted antibody denaturation or aggregation occurring during the dehydration step.

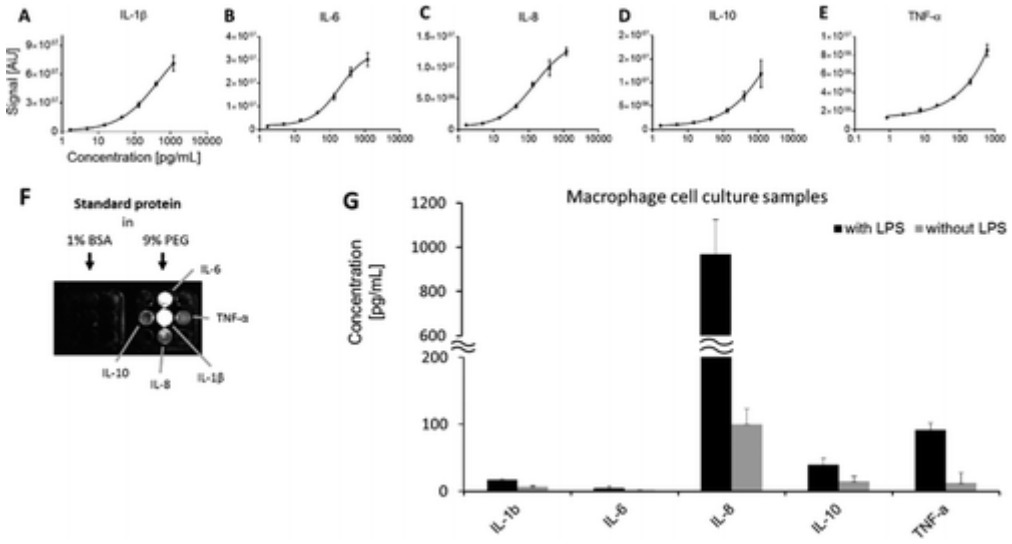

Figure 3.5. Calibration data and results for analysis of cytokines in two sample diluents and macrophage cell culture supernatant. Calibration curves for IL-1β (A), IL-6 (B), IL-8 (C), IL-10 (D), and TNF-α (E). Data shown are mean chemiluminescence signals from two replicates, and error bars are standard deviations (SDs). A comparison of prespotted wells filled with standard proteins diluted in 1% BSA in PBS to wells filled with proteins prepared in diluent containing 9% PEG shows no signal from any biomarker if PEG is not present (F). Results from macrophage cell culture samples with (black ■) and without (gray ■) LPS treatment are shown in G. IL-8 displayed a 10-fold increase in concentration for LPS-stimulated cells compared to nonstimulated cells. Similarly, a 7-fold increase was observed for TNF-α, and 2-fold increases for IL-1β and IL-10. *n* = 4 replicate measurements, error bars are standard deviations.

Table 3.1. Comparison of Limit of Detection (LOD) and Signal to Noise Ratio (*S*/*N*) for Singleplex ELISA, Manual Multiplex ATPS, and Prespotted Multiplex ATPS ELISA

	IL-1b	**IL-6**	**IL-8**	**IL-10**	**TNF-a**
			LOD [pg/mL]		
singleplex	2.69	<4.94	1.02	<4.94	<1.65
manual ATPS	<1.65	1.40	1.87	2.81	0.52
prespotted ATPS	2.05	<1.65	2.72	3.40	1.67
			S*/*N		
singleplex	171.9	10.8	138.7	10.4	4.1
manual ATPS	224.8	51.9	85.5	40.2	25.3
prespotted ATPS	64.8	30.2	19.3	16.4	7.6

Non-ATPS multiplex assays were also attempted using identical plate layout and reagent amounts. For this, plates were prepared and dehydrated using previously described methods. Instead of rehydrating this plate with the ATPS-forming PEG diluent, however, we used a sample diluent consisting of 1% BSA in PBS. Resulting signal from this non-ATPS protocol could not be distinguished from background, suggesting diffusion and loss of dAbs into bulk solution. This again confirms the benefits of an ATPS method in providing dAb reagent savings, as a conventional, plate-based multiplex ELISA using these dAb amounts would not give signals. A comparison between signal produced from dehydrated ATPS multiplex and non-ATPS multiplex assays is shown in Figure 3.5F. At the time of plate imaging,

chemiluminescence signal is generated at HRP molecules conjugated to detection antibodies that have bound with antigen and are no longer free to diffuse. No ATPS is present at this step, and signal location and intensity represents the degree of antigen–antibody binding.

This 5-plex cytokine test was then used to analyze cell culture supernatant from LPS-stimulated human ThP-1 cells. Stimulation with LPS simulates a Gram-negative bacterial infection and can be used to study a pro-inflammatory response with the ThP-1 cell line (111). Calibration data from this experiment is shown in Figure 3.5A–E, and results are shown in Figure 3.5G. Interestingly, data showed a 10-fold increase in IL-8 secretion from stimulated cells compared to nonstimulated cells (Table A.3.2). Additionally, we observed a 7-fold increase in TNF-α levels, and a 2.5-fold increase in IL-10 and IL-1β in stimulated versus nonstimulated data sets. IL-6 levels also increased to detectable levels whereas controls were below the detection limit. Results from *t* tests (Table A.3.2) show statistically significant differences between the stimulated and nonstimulated samples. Importantly, the observed changes in cytokine levels found here complement trends found in other studies investigating LPS-stimulated ThP-1 cells (111, 120).

3.4. Conclusions

In this report, we demonstrated the utility of a user-friendly multiplex ATPS-format ELISA test for cytokines in cell culture supernatant. The formation of microdomains with ATPS enables compartmentalization, concentration, and storage of molecules. In this method, all multiplex ELISA reagents are prespotted and dehydrated on a multiwell plate prior to the assay, vastly reducing user pipetting steps at the point-of-use. The spotting of both cAb and dAb required for a sandwich assay exploits the benefits of an ATPS for preserving reagents in the dextran phase during dehydration, as well as after spontaneous rehydration during the assay.

Although a 5-plex analysis is demonstrated here, higher plexing is possible. The upper limit of plexing is controlled by ATPS formation and PEG/DEX ratios, as

well as the ability to reproducibly create small droplets to increase the number of analyses per well. This method also provides significant reagent savings, as orders of magnitude less dAb is used per analyte compared to other multiplex ELISA platforms generating strong signals and comparable LODs. Although plate preparation for this method includes a high number of pipetting steps, droplet placement is less specialized, and these steps can be easily automated with a liquid handling station. Importantly, this technology should be applicable to a broad combination of biomarkers including “incompatible” combinations that show reagent related cross-talk in conventional ELISA where dAb is applied as a mixture or cocktail.

Chapter adapted with permission from Eiden L, Yamanishi C, Takayama S, Dishinger JF. Aqueous Two-Phase System Rehydration of Antibody-Polymer Microarrays Enables Convenient Compartmentalized Multiplex Immunoassays. Anal Chem. 2016;88(23):11328-34. Copyright 2016 American Chemical Society.

CHAPTER 4: One-Incubation One-Hour Multiplex ELISA Enabled by ATPS

4.1. Introduction

ELISAs enable selective quantification of a variety of analytes, including small molecules, proteins, viruses, and bacteria, by employing an enzyme linked antigen or antibody as a marker for the detection of specific analytes (121). When appropriate antibodies are available, ELISA can provide high sensitivity and high specificity (122). However, this technique can involve time-consuming procedures and tedious washing processes. Moreover, it is normally limited to only one target at a time (122, 123). Contemporary studies have shown that many diseases and biological processes involve multiple different proteins, highlighting the need for measurement of multiple targets within the same sample (124-126).

Recent advances have enabled multiplex ELISA, allowing for simultaneous detection of multiple targets, conserving time and reagents, thus enabling analysis of more complex biological processes (75, 105, 127, 128). However, the typical multiplex sandwich ELISA assay involves three separate incubation steps for three different protein-ligand interactions, as in Figure 4.1A: (i) binding of analyte to capture antibody (cAb), (ii) binding of detection antibody (dAb) to cAb-bound analyte, and (iii) binding of streptavidin-HRP to the analyte-bound dAb through a biotin-streptavidin interaction (129-131). Note that each incubation step is also followed by wash steps. To enable ELISA multiplex detection, cAbs for different targets can be arrayed within single microwell. However, this strategy quickly becomes susceptible to unintended cross reactions between antibody reagents (91).

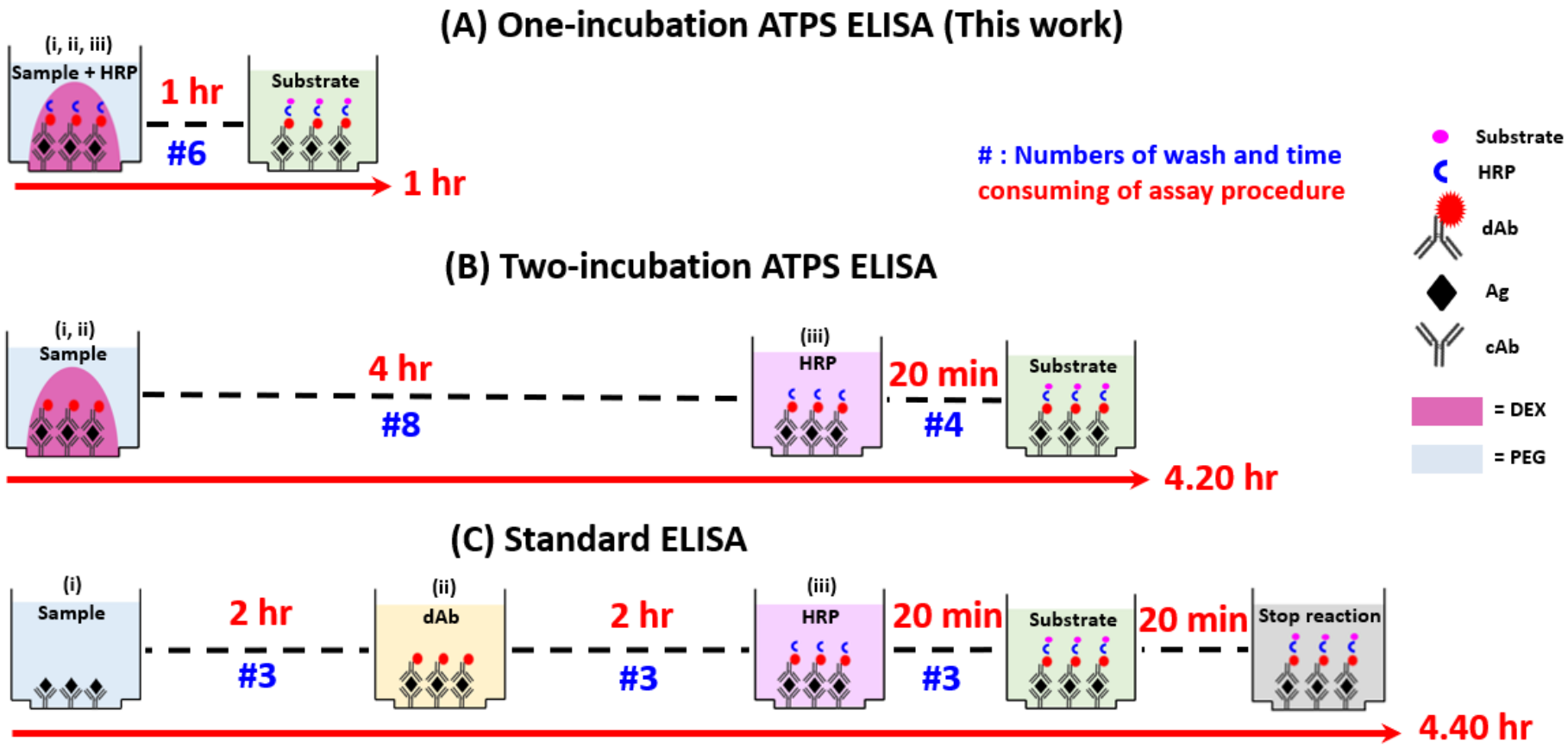

Figure. 4.1. Schematic of ELISA procedure: (A) Standard ELISA for singleplex detection, (B) Two-incubation ATPS ELISA and (C) One-incubation ATPS ELISA for multiplex detection.

An aqueous two-phase systems (ATPS) approach was developed previously to enable to protect cross-reaction in multiplex ELISA (18). Antibodies remain confined to their designated locations within dextran microdroplets during the detection antibody binding step. Table 4.1 summarizes previous reports of multiplex ELISA detection of cytokines by employing ATPS; assay information is given such as assay time, numbers of incubation, wash, material, types of plate, microbasin, working range, S/N and LOD. Our group previously demonstrated that these cross-reactions can be avoided by using ATPS to co-localize correct antibody pairs (18, 74). More recently, our group showed that the ATPS ELISA technique could be used with dehydrated reagents, allowing the dAb microarray to be in place before the user adds sample (19). In that technique Figure 4.1B, dAb in a dextran (DEX) solution is microarrayed over corresponding cAb-coated microbasins followed by dehydration. Sample aliquot was diluted into a poly (ethylene glycol) (PEG) solution and added into the well. Water from the PEG solution rehydrates the DEX microdroplet, while maintaining phase separation and antibody confinement. Target proteins, however, are able to penetrate into the DEX phase for binding in the sandwich assay. Thus, the first two binding steps (i, ii) are integrated into one step which took 4 hours. Subsequent washing, 20 minutes incubation with streptavidin-HRP, washing, and addition of HRP substrate generate ELISA signals.

Table 4.1. Previous ATPS ELISA method of cytokine detection (singleplex and multiplex), assay information included; assay time, numbers of incubation, wash, material, types of plate, microbasin, working range, S/N and LOD.

Cytokine detection	Assay time	Numbers (incubation, wash)	Material, type of plate, microbasin	Working range (pg/mL)	S/N	LOD (pg/mL)	Ref.
Singleplex* (Standard ELISA)	4 hr, 40 min	(Two, 9)	Polystyrene, clear plate, clear microbasin	3.91-2,000	IL-6 = 30.1 IL-10 = 15 TNF-α = 10.1 IL-1β = 30.1 IL-8 = 33.2	IL-6 = 9.38 IL-10 = 31.2 TNF-α = 15.6 IL-1β = 3.91 IL-8 = 7.81	Commercial R&D ELISA kit
Singleplex (ATPS ELISA)	15 min	(Two, 9)	Polystyrene, black plate, black microbasin	31.25-2,000	N/A	N/A	(132)
Multiplex (AlphaLISA ATPS ELISA)	2 hr	N/A	Polystyrene, black plate, white microbasin	1-1,200	N/A	IL-6 = 6.2 IL-8 = 20.6 CXCL9 = 20.1 CXCL10 = 11.8	(74) (18)
Multiplex (ATPS ELISA)	5 hr	(Two, 18)	Polystyrene, clear plate, clear microbasin	1-10,000	N/A	HGF = 96 Elafin = 1437 ST2 = 103 TNFR1 = 87	(18, 74)

Table 4.1. (Continued).

Multiplex (ATPS ELISA)	4 hr, 20 min	(Two, 12)	Polystyrene, clear plate, clear microbasin	1-1,200	IL-6 = 30.2 IL-10 = 16.4 TNF-α = 7.6 IL-1β = 64.8 IL-8 = 19.3	IL-6 = <1.65 IL-10 = 3.40 TNF-α = 1.67 IL-1β = 2.05 IL-8 = 2.72	(19)
Multiplex (ATPS ELISA)	1 hr	(One, 6)	Polystyrene, black plate, black microbasin	1-2,000	IL-6 = 30.3 IL-10 = 10.1 TNF-α = 27.2 IL-1β = 43.06 CCL18 = 43.52	IL-6 = 1.82 IL-10 = 4.89 TNF-α = 2.41 IL-1β = 7.63 CCL18 = 3.65	This work

*Non ATPS: This assay is for method comparison
N/A: Not available

In this work, we report an additional evolution of the ATPS ELISA where the HRP reagent is already included in the sample PEG solution so that after pipetting samples to the plate pre-spotted with antibodies and DEX polymer there is only one washing procedure before signal readout. The plate leads to all three-binding interactions (i, ii, iii) occurring in a single step, 1-hour incubation, as shown in Figure 4.1C. This procedure reduces total time for the ELISA by 5-fold, while also minimizing wash steps. In addition to user convenience, this new assay maintains previously-reported advantages of ATPS-ELISA, such as two orders of magnitude lower consumption of dAb and minimizing dAb cross-reactions due to ATPS confinement. Furthermore, through consideration of ATPS composition, we achieve favorable sensitivity and high assay performance compared to our previously reported method (19), and to singleplex methods. Another substantial improvement over our previous report is the use of a black rather than clear plastic microwell plates to reduce optical cross-talk through the plastic. Lastly, we perform analyses of THP-1 macrophage secreted cytokines using this convenient one-incubation ELISA and characterize M1 and M2 polarized cells. This rapid, one-incubation ELISA moves the ATPS ELISA method closer to clinical utility, where it could aid in diagnosis of infections or other diseases (133).

4.2. Materials and methods

4.2.1. Chemicals and reagents

ELISA DuoSet kits for human IL-6 (DY206), human IL-10 (DY217B-05), human TNF-α (DY210), human IL-1β (DY201) and human CCL18 (DY394-05) were acquired from R&D Systems. Each DuoSet kit contains cAbs, dAbs, antigen standards and 40× streptavidin-HRP. SuperSignal™ ELISA Femto Substrate (product no. 37075) was purchased from Thermo Fisher Scientific (Rockford, IL, USA). All cAbs were diluted in 1×PBS pH 7.4 (10010-023) from Gibco, Life Technologies. Other reagents were prepared in buffers containing indicated amounts of distilled water (Gibco, Life Technologies, 15230-170), 5×StabilCoat (SurModics, Eden Prairie, MN, USA), DEX

MW 500,000 g/mol, PEG MW 35,000 g/mol, Tween 20 (Sigma, St. Louis, MO, USA), and bovine serum albumin (BSA) (Millipore, Burlington, MA, USA).

4.2.2 Fluorescence image detection of FITC-dAb DEX for optimal conditions of one-incubation assay

Fluorescent stereo microscope (Leica M165 FC, Leica Microsystems) was used for all bright field and fluorescence imaging (λex: 490 nm, λem: 520 nm). Investigation of conditions for one-incubation assay: selection of ATPS system (i.e. ATPS condition) and blocking buffer were carried out by using custom 96-well injection molded black plates with 1.7 mm diameter microbasins (9 per well) (PHASIQ, Ann Arbor, Michigan).

Selection of ATPS condition: Investigation of FITC-dAb retention in DEX was studied, concentration of PEG-DEX (%w/w) is provided following; (a) 9%-9%, (b) 5%-9%, (c) 9%-5%, (d) 5%-5%, (e) 3%-5%, (f) 5%-3% and (g) 3%-3% as shown in Fig 1(B). Dedicated DEX concentrations were spotted on the black plate (1uL/1 microbasin) by (Repeater®, Eppendorf, Hauppauge, NY, USA). The plate was dried in desiccator for 1 hour. Next, dedicated PEG concentration were added into each well. After 1 hour, the plate was imaged by the fluorescence microscope.

Selection of blocking buffer: Five types of blocking buffer (3× StabilCoatTM, 1× StabilCoatTM, 5% BSA, 5% goat serum, and 0.1% ChonblockTM with 0.05% goat serum) were spotted on the black plate (1uL/1 microbasin). The plate was dried in a desiccator for 1 hour. Then, 1 μL of 5% DEX was placed on dried cAb spots. After 1 hour, the plate was imaged by the fluorescence microscope.

4.2.3 Singleplex detection by standard ELISA procedure

Singleplex ELISA was performed according to manufacturer instructions from R&D DuoSet ELISA at room temperature (25 ^{o}C). Briefly, transparent microwell plate was prepared as follows: 100 μL of the working dilution of cAbs was coated on each well of 96-well microplate and incubated overnight. The plates were washed sequentially 3 times with 400 μL of 0.05% Tween 20 in PBS each, then blocked with

300 µL of 1% BSA in PBS (1×, pH 7.4) for 1 hour. After blocking, the plate was repeated washed sequentially 3 times. Next, antigen standards or sample (prepared in 1%BSA in PBS in a two-fold dilution series) were added at 100 µL per well and the plate was incubated for 2 hours at room temperature in the dark. The plate was washed and incubated with 100 µL of appropriate dAb per well for 2-hour incubation. Following additional 3× washing, 100 µL of streptavidin-HRP was added to each well at the manufacturer's recommended concentration and the plate was incubated for 20 minutes in the dark. After a final wash, 100 µL of enzyme substrate peroxidase chromogen was added into each well. After 20 minutes of incubation in the dark, 50 µL of 0.18 M H_2SO_4 was added into each well to stop the reaction. Lastly, a BioTek Synergy H4 microplate reader was used to measure absorbance at 450 nm.

4.2.4 Multiplex detection by ATPS ELISA procedure

Two multiplex detection methods of ATPS ELISA (i.e. One-and two-incubations) were performed by employing custom 96-well injection molded black plates. Microplates were washed prior to immobilization step by spraying with ethanol and followed by distilled water, the washed plated was kept a desiccator for drying and storing until needed.

4.2.4.1 One-incubation ATPS ELISA procedure

Firstly, cAb were arrayed at indicated concentrations by pipetting of 1.0 □L (Repeater®, Eppendorf, Hauppauge, NY, USA) into appropriate microbasins within each microplate well. The arrayed plates of cAb immobilization were covered and stored under dark condition at room temperature for 90 minutes. After that the plates were washed three times with wash buffer (i.e. 0.05% Tween 20 in PBS) to remove all unbounded cAb. Then, 100 µL of 5% sucrose in PBS was added into each well to block remaining binding surfaces and to stabilize the cAbs against denaturation during dehydration. After removing of sucrose, plates were dried in a desiccator for 40 minutes to facilitate accurate microarraying in subsequent steps. To more thoroughly cover binding surfaces, indicated blocking buffers were arrayed into every microbasin

containing cAb by Eppendorf repeater pipette, followed by an additional 40 minute drying step. Detection antibody was prepared in distilled water with DEX with various desired concentrations (i.e. 9%, 5% and 3%w/w). These dAb solutions were spotted at 1 µL per microbasin and dried in a vacuum desiccator overnight. Next, antigen standards were diluted 1:1 serial dilution between solution containing indicated concentrations of PEG, 0.05% Tween 20, 0.5% BSA, and indicated concentrations of streptavidin-HRP in PBS, along with antigen standards or samples. A 7-point standard curve was constructed with 2-fold dilutions from 2,000 pg/mL in triplicate. After adding 100 µL of standard solution in each well, plate was incubated for 1 hour. And then, plates were washed 6 times with wash buffer to remove all unbounded proteins. These additional wash steps were necessary to remove viscous ATPS components. Finally, 100 µL of the chemiluminescence substrate was added into each well before taking images using a BioRad ChemiDoc MP+ Western Blot reader with an exposure time of 40 seconds.

4.2.4.2 Two-incubation ATPS ELISA procedure

The two-incubation ELISA was different from the one-incubation ELISA with the following changes. For assay procedure of two-incubation ELISA, there is no streptavidin-HRP in PEG solution. Thus, 100 µL of streptavidin-HRP solution was added into each well after 1-hour incubation. After streptavidin-HRP incubation, the plate was washed three times with wash buffer, filled with 100 µL of chemiluminescence substrate for each well as shown in Figure 4.1B. The details of this procedure can be found in previous report by our group (132, 134). All tested and optimal conditions are summarized in Table A.4.1.

4.2.5. Cell culture and macrophage preparation

Human monocytic THP-1 cells (ATCC, TIB-202) were grown in Roswell Park Memorial Institute (RPMI) 1640 biotin-free medium (MyBioSource, MBS653376) with 10% fetal bovine serum (FBS) (Gemini Bio-products), and 1% penicillin-streptomycin (Gibco). Cells were seeded in T75 flasks at a density of 1×10^6 cells/mL, and

differentiated into macrophages as described by Spiller et. al. (135), with 320 nM PMA (Sigma) and incubated overnight. The activated and now adherent THP-1 derived macrophages were washed three times with fresh media to remove PMA. THP-1-derived macrophages were then detached using Accutase (Sigma, A6964) for 5-10 minutes at 37^{o}C followed by gentle scraping before being collected and counted using a Nexcelom Cell Counter. Subsequently, macrophages were seeded into T25 flasks for polarization into M1 or M2 macrophages (105). Macrophages were polarized toward M1 by adding 100 ng/mL LPS (Sigma, L2630), and 100 ng/mL interferon gamma (IFN-γ) (R&D Systems, 285-IF), and incubated for 48 h. Macrophages were polarized toward M2 by adding 20 ng/mL IL-13 (R&D Systems, 213-ILB), and 40 ng/mL IL-4 (R&D Systems, 204-IL), and incubated for 48 hours. Cells were washed three times in cell culture medium and incubated for 24 hours to allow the macrophages to secrete cytokines into the supernatant. Supernatants were collected and centrifuged at 200× g for 5 minutes to remove dead cells and debris, then frozen at -80^{o}C for subsequent ELISA analysis.

4.2.6 Fluorescence/chemiluminescence imaging: Image J

Image J Software (http://imagej.nih.gov/ij/) was used for evaluation of fluorescence intensity from FITC-dAb images and all chemiluminescence images from ELISA. A custom Image J plugin was written to aid in identifying and outlining microbasin areas within each well. Briefly, the plugin guides the user through image rotation and determination of the size and locations of microbasins to generate a plate-wide map. The plugin then measured the average chemiluminescence intensity for each microbasin, exporting an Excel sheet with annotated wells and microbasin intensities.

4.2.7. Evaluation of analytical characteristic of ELISA assay

Standard curves were constructed and fitted with a four-parameter logistic function in Graph Pad Prism for calculating sample values. The limit of detection was calculated as LOB + 1.65 ($SD_{\text{low concentration sample}}$), where LOB is the limit of blank and

SD is the standard deviation. LOB was computed from LOB = $mean_{blank}$ + 1.645(SD_{blank}). Signal to noise ratios (S/N) were calculated as mean signal from the highest antigen standards (2,000 pg/mL) divided by mean of the blank, assuming that noise does not correlate with signal intensity. Coefficient of variation (CV) was calculated as percent of SD from antigen standard signal divided by mean of the signal. A t-test was performed by GraphPad InStat software (GraphPad Software Inc., San Diego, CA, USA) for statistical analysis (unpaired t test) between M1 and M2 (Section 4.3.3).

4.3. Results and discussion

In this work, we compare three ELISA assays, as shown in Figure 4.1A-C. For standard ELISA (Figure 4.1A), dAb incubation is separate and follows antigen binding to surface immobilized cAb, resulting in more steps and longer overall assay time. The total assay time is 4 hours with nine washing steps. For the two-incubation ATPS ELISA that we reported previously Figure 4.1B, dAbs are pre-spotted reducing the number of steps in the assay. Our newly described one-incubation ELISA includes HRP in the sample PEG solution and has an optimized PEG and DEX formulation, as described below, that reduces the incubation time by 4-fold (1 hour) and reduces wash steps by half Figure 4.1C.

4.3.1. Optimization of one-incubation ATPS ELISA

In consideration of recent work by our group, showing that ATPS composition can influence mass transport within the rehydrating DEX phase (132), we examined ATPS composition to balance the competing factors of 1. high polymer content for high dAb retention in the DEX phase, and 2. low polymer content for low viscosity and improved mass transport.

4.3.1.1 Investigation of ATPS conditions

Concentrations of PEG and DEX are key parameters for ATPS ELISAs because they affect retention of detection antibodies in DEX phase, and in the case of assays that include HRP in the PEG phase, the amount of non-specific background

signal generated. As shown in Figures 4.2A and 4.2B, we tested seven different formulations of PEG-DEX concentrations to study their effect on detection-antibody retention. ATPS solutions of different PEG-DEX concentrations (%w/w) were; (a) 5%PEG-5%DEX, (b) 9%PEG-9%DEX, (c) 5%PEG-9%DEX, (d) 9%PEG-5%DEX, (e) 3%PEG-5%DEX, (f) 5%PEG-3%DEX and (g) 3%PEG-3%DEX, each ATPS condition was also performed with one-incubation ELISA and the calculated LODs were 1.82, 231.11, 24.38, 30.23, 12, 96.36 and 267.28 pg/mL, respectively (Figure 4.1C. All fluorescence images of ATPS solution of FITC-dAb-DEX were given in Figure A.4.1). A majority of the goat anti-human IgG FITC-antibodies are retained within DEX phases over the course of 1 hour for high and medium concentration of DEX (9% and 5%w/w, respectively) but not at the lower concentration of DEX. Moreover, size and shape of DEX droplets remain consistent over this period.

We next determined the calibration curves for a singleplex IL-6 ATPS ELISA using the same 7 different PEG-DEX formulations (Figure 4.2C). Low PEG and DEX concentration (3%) have low antibody retention in DEX (Figure 4.2) leading to low signal and low sensitivity as expected. The high PEG and DEX concentrations (9%) produced high background. Surprisingly, high PEG and DEX concentrations (9%) that yield high antibody retention in DEX droplets also had lower signal than the moderate concentrations (5%). This may be due to the high viscosity, which limits the ability of the analyte to interact with cAbs at the surface and dAbs in solution. The medium PEG and DEX concentration (5%) balanced the two competing needs of a high signal and low noise, providing the best standard curve.

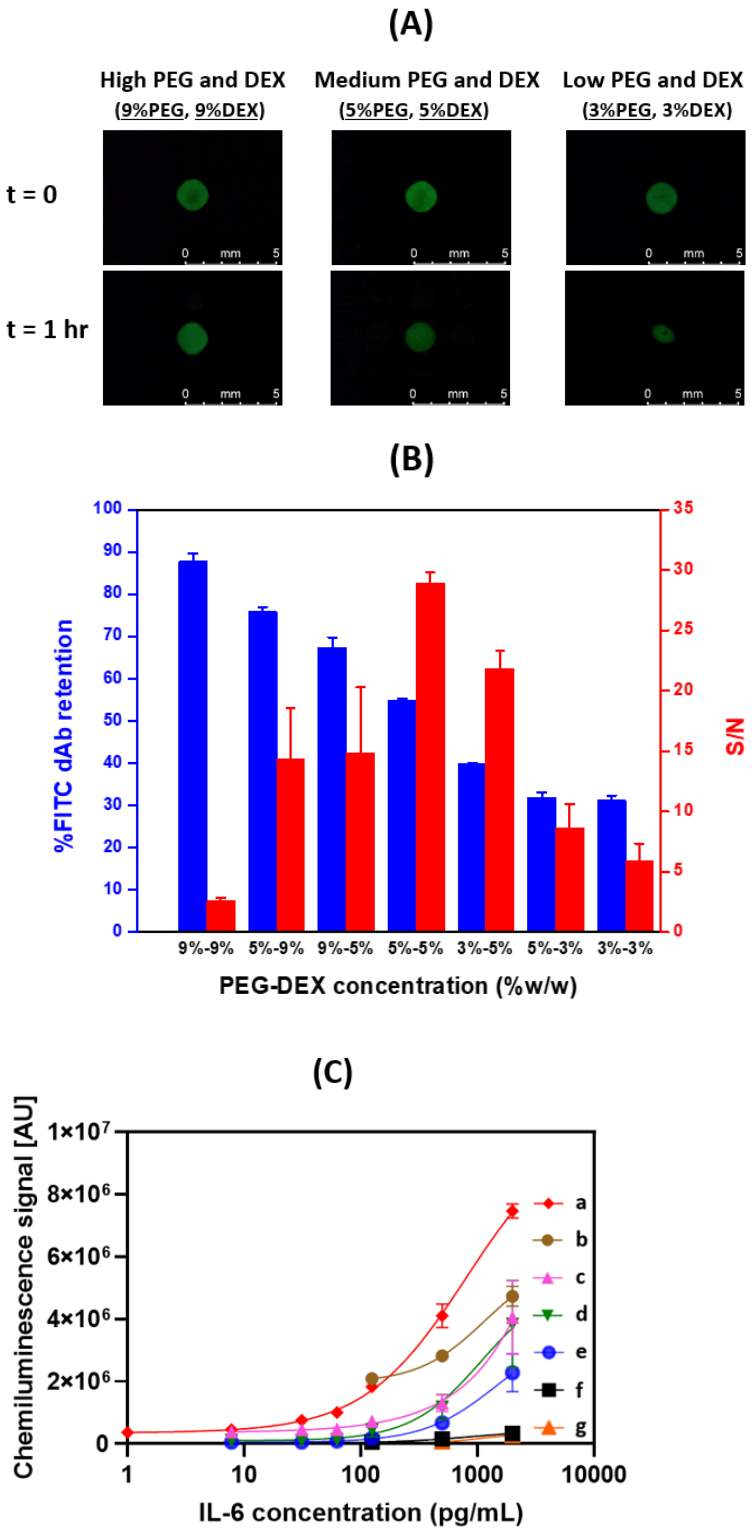

Figure 4.2. Effect of PEG-DEX concentration on FITC-dAb retention in DEX and ELISA reaction; (A) Bar graph for percent of FITC-dAb retaining in DEX droplets and S/N. PEG-DEX concentration; (a) 5%PEG-5%DEX, (b) 9%PEG-9%DEX, (c) 5%PEG-9%DEX, (d) 9%PEG-5%DEX, (e) 3%PEG-5%DEX, (f) 5%PEG-3%DEX and (g) 3%PEG-3%DEX The percent was measured by fraction of FITC-antibodies intensity in 0 minutes to 1 hour multiplying with 100 from three replicate measurements, bars are standard deviations (SDs). (B) Fluorescence images of FITC-dAb retaining in DEX droplets (C) Effect of PEG-DEX concentration on ELISA reaction.

4.3.1.2 Incubation time

The typical sandwich ELISA assay involves three separate incubation steps for three different protein-ligand interactions: (i) binding of analyte to cAb, (ii) binding of dAb to cAb-bound analyte, and (iii) binding of HRP to the analyte-bound dAb through a biotin-streptavidin interaction. Each incubation step is also followed by wash steps. In our previously published multiplex ATPS ELISA assay, we integrated the first two binding incubations into one step which took 4 hours, followed by wash, incubation with HRP for another 20 minutes, another wash, and then reading chemiluminescent signal. In a more recent singleplex ATPS ELISA that also integrates the first two binding incubations, we demonstrated a formulation with enhanced internal convection that provided signals with just a 15 minute incubation time rather than 4 hours, although with slightly inferior sensitivity. For our new one-incubation ELISA, we investigated incubation times of 15 minutes, 1 hour and 4 hours as shown in Table 4.2.

Table 4.2. Effect of incubation time on ATPS ELISA (15 minutes, 1 hour and 4 hours). The performance was carried out with information, LOD, CV (%) and S/N±SD (n=3) obtained by using each incubation time is listed.

Incubation time	LOD (pg/mL)	CV (%)	S/N±SD	ELISA images	
				Signal	Noise
15 minutes	>500	3.69%	3.74±0.03		
1 hour	<1	1.34%	28.91±0.89		
4 hours	442	5.88%	1.61±0.09	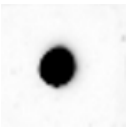	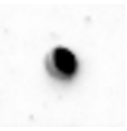

We found that in our new procedure that integrates all three-binding interaction into one incubation with 1 hour provided an optimal time for incubation, it provided sufficiently high signal with low background signal that leads to high S/N and low LOD (see details in Figure A.4.2 and Figure A.4.3). The shorter time (15 minutes) was not sufficient time for strong signals to be obtained. On the other hand, a 4-hour incubation also did not enhance sensitivity because of a higher background signal.

4.3.1.3. Blocking buffer

Common blocking buffer solutions are composed of proteins, surfactants, or other additive compounds that minimize aggregation, precipitation, and nonspecific interaction of regents and analyte to surfaces. Blocking buffer can also stabilize antibody molecules on dried surfaces through a variety of mechanisms, including hydrogen bonding replacement and vitrification (136). Identification of an appropriate blocking scheme is critical for achieving high signal-to-noise ratios. Table 3 lists five types of blocking buffer for selection.

We also determined the calibration curves for an ATPS ELISA using 5 different blocking buffers: 3× StabilCoatTM, 1× StabilCoatTM, 5% BSA, 5% goat serum, and 0.1% ChonblockTM with 0.05% goat serum (137, 138).

BSA is a commonly used blocking agents typically used at a 1 to 5% concentration. As displayed in Table 4.3, dehydrated 5%BSA-5%DEX generates an inconsistent, porous surface during dehydration that led to low repeatability and low sensitivity. Use of goat serum and Chonblock™ led to weak signals. StabilCoat™ produced dehydrated DEX spots with the smoothest surface (Table 4.3) and provided high repeatability in IL-6 ELISAs. The use of 3× StabilCoat provided better sensitivity than 1× StabilCoat. The concentrated buffer of 3× StabilCoat generated lower background signal.

Table 4.3. Images of dried spots employing different types of blocking buffer with 5% DEX containing IgG FITC-antibodies. A scale bar was 1000 μm. Performing of ATPS ELISA was carried out with information, LOD, CV (%) and S/N±SD (n=3) obtained by using each blocking buffer is listed.

Parameters	**3× StabilCoat**	**1× StabilCoat**	**5%BSA**	**5%Goat serum**	**0.1%Chonblock/ 0.05%goat serum**
Bright field images	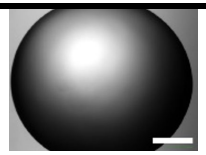	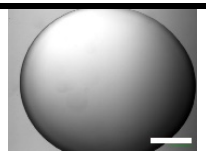	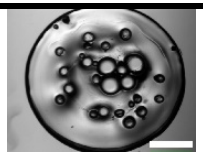	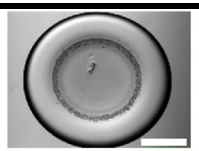	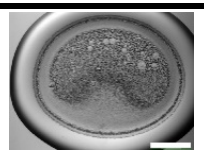
Fluorescence images	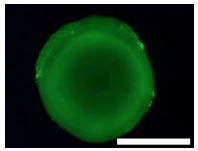	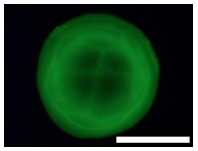	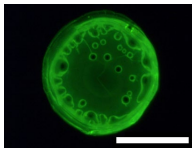	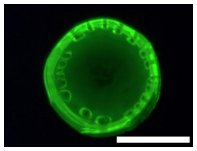	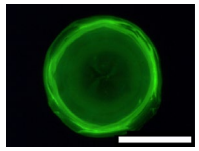
LOD (pg/mL)	<1	26.17	95.13	69	1,660
CV (%)	1.88	3.01	54.68	36.98	68.65
S/N±SD	27.79±0.45	9.62±0.65	2.64±0.46	3.78±0.40	2.70±0.06

4.3.1.4. Capture antibody, detection antibody and HRP concentrations

Selection of suitable concentrations of capture antibody, detection antibody and HRP for one-incubation ATPS ELISA was performed.

Capture antibody concentration: To determine suitable cAb concentration to spot, 1 µL droplets containing 2 to 25 µg/mL of cAb (0.002-0.025 µg of cAb) were arrayed and the S/N of ATPS ELISA performance determined (Fig. 4.3A). Signal increased as more cAb was immobilized, then leveled off. Because our plate preparation involves a step where excess cAb is washed away prior to dAb spotting, higher cAb spotting does not lead to a hook effect where the S/N decreases, in contrast to our previous method (19). From these results, we selected cAb concentrations of 10 ng/mL for IL-6, IL-10, TNF-α, IL-1β and CCL18.

Detection antibody: Figure 4.3B presents a dAb concentration study to determine optimal dAb concentrations for improving S/N. Specifically, a concentration range of dAb from 1 to 75 ng/mL (0.001-0.075 ng of dAb) was tested. Curves reached a peak prior to reduction of S/N at higher concentrations. The decrease in S/N at higher dAb concentration generally resulted from high background signal. Based on these results we selected dAb concentrations of 10 ng/mL for IL-6, 25 ng/mL for IL-10, TNF-α, IL-1β and CCL18.

HRP concentration: HRP concentration plays important role to enhance S/N and it was tested as shown in Figure 4.3C. The key takes away is that too little leads to weak signal while too much leads to high background. The optimal amount of HRP in an assay also depends on the total amount of biotinylated dAb that is present in an assay microwell because the streptavidin-conjugated HRP is incubated together with the dAb before any excess is washed away, unlike typical protocols. Based on these considerations, the optimum HRP concentration was found to be 5× the manufacturer recommended concentration.

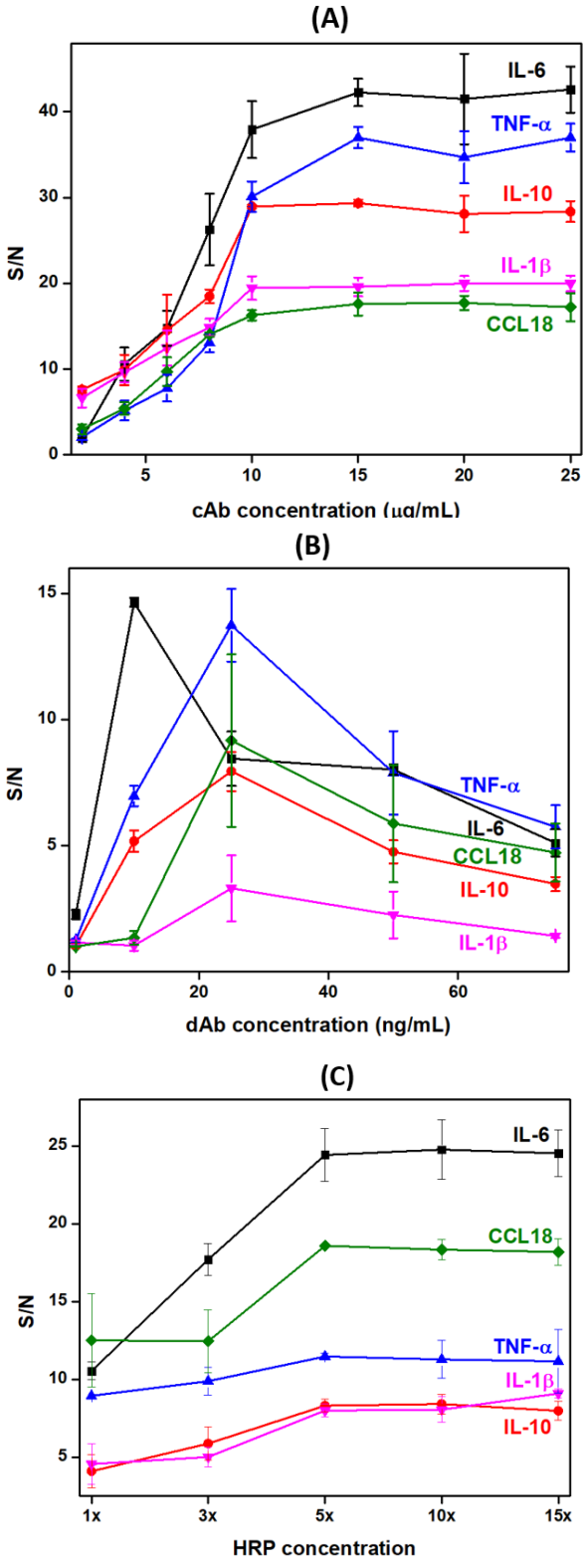

Figure 4.3. Determination of optimal cAb, dAb and HRP concentrations shows mean chemiluminescent signal, and the error bars are standard deviations; (A) cAb concentration (0-25 μg/mL), (B) dAb concentration (0-75 ng/mL) and (C) HRP concentration (1×-15×).

4.3.2. Comparison of ELISA performance for multiplex detection

As an application for the newly developed one-incubation ATPS ELISA, we compare the ELISA performance of three procedures (see Figure 4.1A-C and Table 4.4) with the detection of a five-cytokine panel (IL-6, IL-10, TNF-α, IL-1β and CCL18). These cytokines, produced by various cell types including macrophages, are important modulators in immune responses and diseases such as cancer, and autoimmune diseases (138). Identifying the cytokine profile released in cell culture supernatants aids in classifying cells into disease-relevant subsets, for example, M1 pro-inflammatory versus M2 pro-regenerative macrophage populations. Therefore, the five-cytokine panel we developed tests typical markers for M1 (IL-6, TNF-α, IL-1β) and M2 (IL-10, CCL18) phenotypes. Calibration curves, LOD, and S/N for standard ELISA (No ATPS), two-incubation and one-incubation ATPS ELISA are shown in Figure 4.4 for each biomarker (Table 4.4).

LOD and S/N comparison between the three methods is shown in Figure 4.1 (A-C) for each cytokine that was investigated. An improved LOD was observed for ATPS ELISA (i.e. one- and two-incubation) compared to the standard ELISA, possibly due to convective mixing and reagent co-localization. Table A.4.2 summarizes previous reports of multiplex ELISA detection of cytokines. It is shown that our method provides short assay time (1 hour) and high sensitivity (LOD = 1.82-7.63 pg/mL) when compared to other methods.

Table 4.4 Performance comparison of three ELISA methods (i.e. standard ELISA, two-incubation ATPS ELISA and one-incubation ATPS ELISA). Comparison of LOD, CV (%) and S/N±SD (n=36) in each method for detection of five cytokines.

Methods	IL-6	IL-10	TNF-α	IL-1β	CCL18
	LOD (pg/mL)				
Standard ELISA	9.4	31.20	15.60	3.91	7.81
Two-incubation ATPS ELISA	28.6	83.50	23.01	60.71	33.18
One-incubation ATPS ELISA	1.8	4.89	2.41	7.63	3.65
	S/N				
Standard ELISA	30.1	15.0	10.10	30.10	33.20
Two-incubation ATPS ELISA	29.7	3.2	14.25	18.60	25.97
One-incubation ATPS ELISA	30.3	10.1	27.20	43.06	43.52
	%CV				
Two-incubation ATPS ELISA	5.53%	4.73%	7.53%	9.81%	8.91%
One-incubation ATPS ELISA	6.64%	4.81%	6.36%	8.43%	8.84%

4.3.3 Measurement of human macrophage cytokine production

We optimized the 5-plex detection assay to test the application of our one-incubation ELISA, see Table 4.5 of summarized conditions for optimization studies and Figure 4.4 for 5-plex standard curves. We measured the cytokine production from ThP-1-derived human macrophages to compare the cytokine secretion of M1 and M2 polarized human macrophages. Figure 4.5 presents the cytokine production by human macrophages (M1 and M2). For statistical analysis, a t-test analysis (unpaired t test) between M1 and M2 was performed; differences between groups were considered statistically significant when $P < 0.01$. Consistent with previous reports (111, 120, 138), we detected higher IL-6 and IL-1β in M1 macrophages, while IL-10 was elevated in M2

macrophages ($P < 0.01$). Both phenotypes expressed TNF-α and CCL18 at similar levels ($P>0.05$). Applying a one-incubation ELISA approach to test cytokine profiles of macrophage supernatants generated results in one hour; faster than commercially available options (5-fold total assay time reduction compared to standard method). Therefore, reducing washing steps significantly to achieve a one-hour incubation time has the potential to accelerate high-throughput observations using cell culture supernatants.

Table 4.5. Summary of the investigated range and selected condition for one-incubation ATPS ELISA

Variable	Investigated range	Selected condition
1. PEG-DEX concentration	9%-9%, 5%-9%, 9%-5%, 5%-5%, 3%-5%, 5%-3% and 3%-3% (%w/w)	5%-5% (%w/w)
2. Incubation time	15 minutes, 1 hour and 4 hours	1 hour
3. Types of blocking buffer	3×StabilCoat, 1×StabilCoat, 5%BSA, 0.5%Goat serum and 0.1%Chonblock/0.05%goat serum	3×StabilCoat
4. cAb concentration	2, 4, 6, 8, 10, 15, 20 and 25 µg/mL	10 µg/mL
5. dAb concentration	1, 10, 25, 50 and 75 ng/mL	10 ng/mL for IL-6, 25 ng/mL for IL-10, TNF-α, IL-1β, and CCL18
6. HRP concentration	1×, 3×, 5×, 10× and 15×	5×

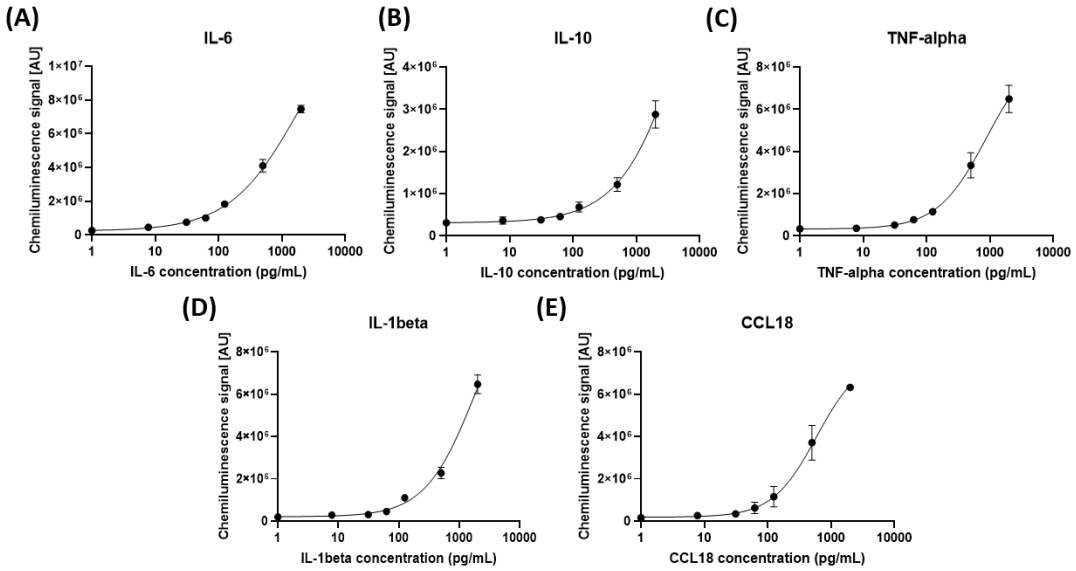

Figure 4.4 Calibration data and results for analysis of cytokines in human monocytic ThP-1 cells. Calibration curves for IL-6, IL-10, TNF-α, IL-1β, and CCL18. Curves shown are mean chemiluminescence signals from three replicates, and error bars are standard deviations (SDs).

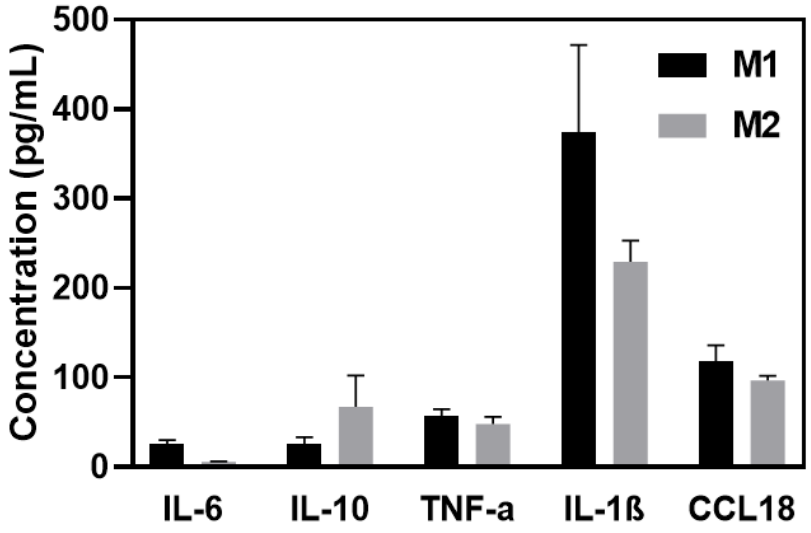

Figure 4.5. Measurement of cytokine production by M1- and M2-polarized macrophage, n = 3 replicate measurements, error bars are SDs. “ns” indicates not significant ($p>0.05$), whereas “**” indicates significant difference ($p<0.01$) between M1 and M2 (unpaired t test).

4.4. Conclusion

We developed a one-incubation with one-hour multiplex immunoassay. We examined competing factors that influence the selection of an ideal ATPS composition for rehydrated, multiplex ELISA: namely antibody retention in the DEX phase, incubation time, selection of blocking buffer, antibody concentration, and HRP concentration. We characterized the signal to noise ratio and the limit of detection for our optimized ATPS ELISA and found improvements over our previous work. Lastly, we demonstrated quantification of cytokines in macrophage supernatants that are consistent with published literature. From a practical perspective, this assay provides a convenient and high sensitivity option for multiplex detection of cytokines. From the perspective of how to formulate ATPSs for ELISA use, this work describes a conceptual shift from simply maximizing antibody partitioning to optimizing the overall process that also includes mass transport and background signal levels.

CHAPTER 5 Biofabrication of phenotypic pulmonary fibrosis assays

5.1. Introduction

Idiopathic pulmonary fibrosis (IPF) is a devastating lung disease, in which normal lung parenchyma is progressively replaced with fibrotic scar tissue. Although the pathology of the disease is varied and still controversial, it generally involves dysregulation of the normal wound healing process. In a prevailing disease theory (139-142), an initial insult to the alveolar epithelial layer leads to recruitment of macrophages and other immune cells in a pro-inflammatory response Figure 5.1. The epithelial injury leads to clotting and fibrin formation, accompanied by fibroblast invasion to plug the wound. The fibroblasts then proliferate and activate (Figure 5.1). Activated fibroblasts, termed myofibroblasts due to the expression of alpha-smooth muscle actin, contract the tissue and deposit extracellular matrix (ECM) to close the wound. In a healthy response, the myofibroblasts would subsequently apoptose to be cleared by macrophages, facilitating re-epithelialization and a return to the original healthy state. In pulmonary fibrosis, however, the myofibroblasts become senescent (143) and continue to generate stiff tissue. Lung stiffening is accompanied by irreversible alveolar collapse, ultimately preventing breathing in patients (144).

Treatment options for pulmonary fibrosis are sparse, highlighting the need for effective models of the disease (145). The standard animal model of pulmonary fibrosis uses bleomycin to generate scar tissue in rodents. This model yields lungs similar in histological appearance to fibrosis, but subtle differences from the human disease have led to misuse of the model (146). In parallel with animal studies, there has been considerable progress in development of complex *in vitro* models of pulmonary fibrosis (147). A subset of these models provide readouts of cell and tissue level phenotypes associated with pulmonary fibrosis. Phenotypic assays are advantageous over mechanistic assays, because they can account for complex, multifactorial cell

behaviors producing sometimes unexpected and emergent behavior. Phenotypic assays have proven generally useful in the discovery of first-in-class new therapeutics (148). In this review, we will examine and contrast a variety of biofabrication techniques to assess pulmonary fibrosis phenotypes in the *in vitro* setting. The analysis aims to summarize progress and highlight challenges and opportunities in this field.

5.2. Techniques for *in vitro* phenotypic analysis of pulmonary fibrosis

This review is organized by describing *in vitro* cell-based assays that aim to recreate various aspects of pulmonary fibrosis pathogenesis roughly in their order of progression *in vivo*: epithelial damage, fibroblast invasion, clotting, fibroblast activation, myofibroblast contraction, and myofibroblast persistence. These techniques are summarized in Figure 5.1, where they are sorted roughly by the phenotypes they cover and when those phenotypes occur in a simplified model of IPF pathogenesis. Table 5.1 at the end of this chapter further summarizes the techniques.

5.2.1 Phenotypic assays incorporating epithelial damage

In the context of pulmonary fibrosis, epithelial damage could arise from a variety of sources, including aging, smoking, infection, inhaled toxins or nanoparticles, and a variety of other potential insults (149). A common observation among IPF patients is telomere shortening. The telomere shortening hypothesis of disease pathogenesis is consistent with the strong correlation between prevalence and patient age. Assays of epithelial damage in the context of IPF should therefore include some consideration of aging, repetitive damage, or similar types of stress. Downstream biochemical signaling has been reviewed elsewhere (150-152), and should also be considered. A plethora of techniques for culturing and assaying epithelial cells exist, but this review will cover those assays that pertain most specifically to epithelial-fibroblast interactions in pulmonary fibrosis.

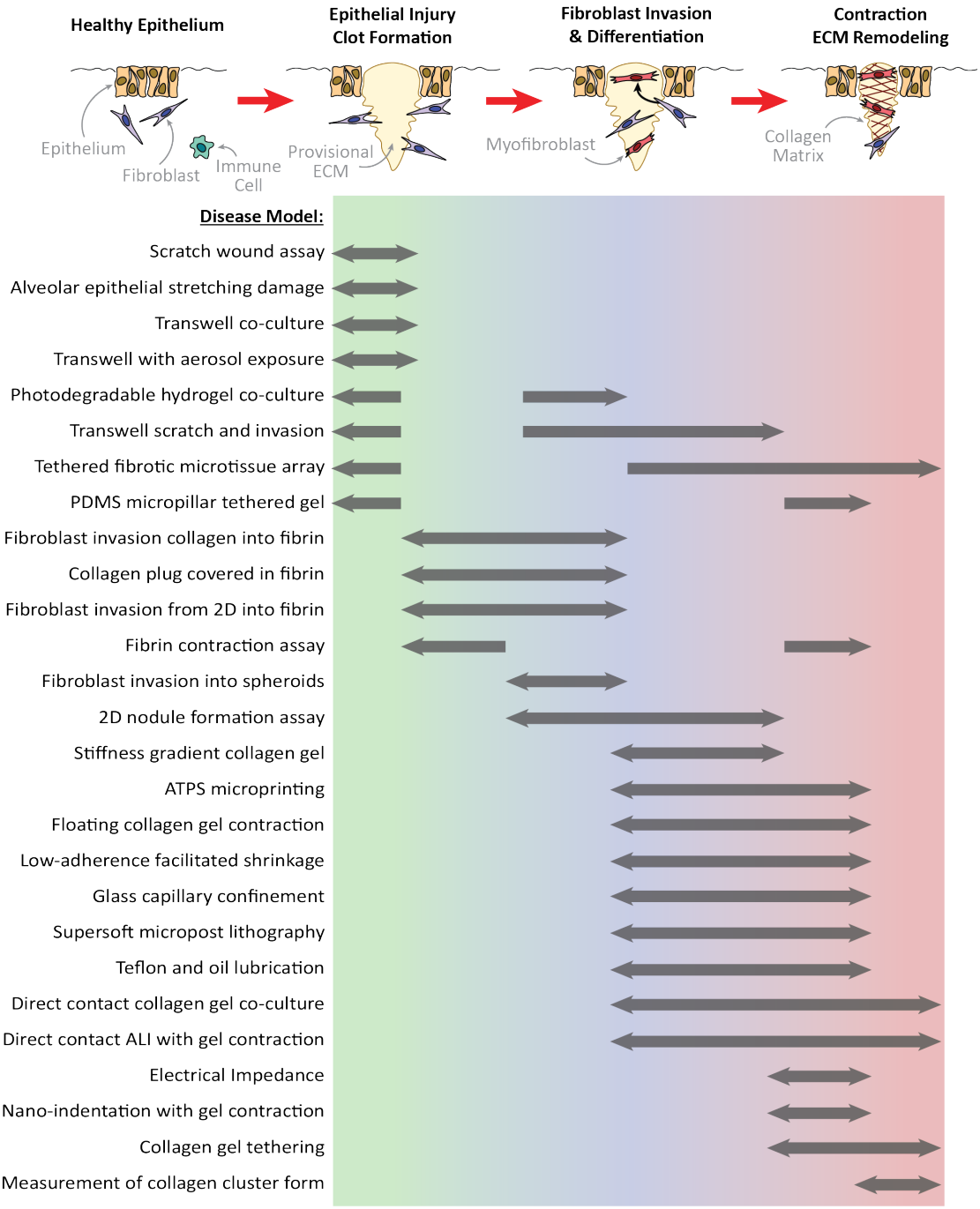

Figure 5.1. In vitro assays of pulmonary fibrosis. In a simplified model of pulmonary fibrosis, an epithelial injury precedes formation of the clot-like provisional extracellular matrix (ECM). Subsequently, fibroblasts invade the wound site and differentiate into myofibroblasts. The myofibroblasts accelerate wound closure by contracting and depositing extracellular matrix components, predominantly collagen. The assays covered in this review are listed and roughly sorted by the phenotypes present in each assay, labelled by the gray arrows. Additional information for each technique is in Table 5.1. Note that some assays span multiple phenotypes that may split across the graph.

Several techniques have been developed to physically induce epithelial damage, the presumed first step towards development of pulmonary fibrosis. Some of these techniques use custom-built devices to impose cyclical strain on epithelial cells, similar to that seen in healthy breathing. In one iteration, alveolar epithelial cells were seeded onto a flexible silicone membrane, anchored with a washer (153). This membrane was cyclically stretched by pressing on the underside of the membrane with a motorized cam mechanism. The authors demonstrated that epithelial cells were damaged by strains of ~25%. Furthermore, additional culture time prior to cyclic strain had a protective effect on the epithelial cells. Another version of the technique comprised a stretching microdevice with flexible polydimethylsiloxane (PDMS) membrane and syringe pump hydraulic actuation (154). This study found that air-liquid interface culture exposed cells to high damage from cyclic stretching at ~35% strain. They also examined fluid mechanical stress from liquid plug movement, finding that the damage could be reduced by addition of pulmonary surfactant. These studies examined physiological strain, but they could be adapted to replicate the fibrotic lung, which is less compliant than healthy lungs. Although hyperventilation has not been causally linked to pulmonary fibrosis, mechanical ventilation has been shown to correlate with bleak outcomes for patients with pulmonary fibrosis whose hypoxemia prompts the use of mechanical ventilation (155, 156). These cyclic stretch models provide methods to assess the epithelial contribution to disease exacerbation.

In static culture settings, membrane culture techniques, such as Transwell culture, have gained tremendous popularity. These devices comprise a porous membrane, fixed to an insert that can be submerged into a culture well, enabling physically separated co-culture between the membrane cell population and the well plate cell population (157). Transwells have also been used extensively to generate and test air-liquid interface (ALI) culture. ALI culture prompts many airway epithelial cells to differentiate into more physiologic epithelium (158). The membrane ALI format

has been adapted to allow aerosol exposure to nanoparticles in well-plate format (159) as well as microfluidic devices (160). In addition to cell viability and biochemical assays, membrane cultures are amenable to measurements of epithelial barrier integrity. Barrier function can be measured by either permeability assays using fluorescently-labeled macromolecules, such as dextran (161), or using trans-epithelial electrical resistance (162). Transwell and membrane techniques present versatile tools for biofabrication of assays incorporating ALI epithelial components.

For analysis of epithelial injury and wound healing, the scratch wound assay is well established (163). Briefly, a confluent monolayer of epithelial cells is denuded using a pipet tip or other blunt object to tear off the epithelial cells. The remaining edges are tracked visually as the epithelial cells proliferate and migrate to repair the wound area. A recent paper combined the scratch wound assay with Transwell co-culture (4), wherein A549 epithelial cells were grown on the top of the membrane, while primary human lung fibroblasts (healthy vs IPF) were grown on the underside of the membrane, as depicted in Figure 5.2A. The authors reported differing behavior in healthy and IPF patient-derived pulmonary fibroblasts. After scratching the epithelial layer, the A549 migrated over 4 days to close the wound. In co-culture with healthy fibroblasts, the fibroblasts migrated into the wound site to plug the gap and inhibited re-epithelialization. However, pulmonary fibrosis-derived fibroblasts failed to invade the wound site, allowing the epithelium to close the wound. This study prompts interesting questions about the long-term behavior of pulmonary fibroblasts in healthy and diseased states, as the healthy fibroblasts appeared more active in the short period examined than the diseased fibroblasts, contrary to what may be expected. Despite the progress made with biofabricated assays of epithelial damage, there remains fertile ground for research regarding long-term culture, chronic epithelial damage, and downstream signaling relevant to IPF. A particularly challenging aspect of lung research has been the inability to culture alveolar epithelial cells. However, recent work

has indicated that co-culture with pulmonary fibroblasts may help solve the problem (35). New biofabrication methods could provide additional benefits by working directly with clinicians to establish cell cultures directly from the source.

5.2.2 Phenotypic assays incorporating fibroblast invasion

Following epithelial damage, a coagulation cascade results in the formation of the provisional ECM. Fibrinogen from blood plasma is cross-linked into fibrin, which is supported hydrostatically by glycosaminoglycans such as hyaluronic acid (164). Fibroblasts from surrounding tissue then invade this provisional ECM in order to initiate the remodeling process. As illustrated in Figure 5.1, formation of the provisional ECM and invasion of fibroblasts is an early component of pathogenesis, where it develops as the consequence of an aberrant wound healing response (140). A number of techniques have been developed to recapitulate behavior of fibroblasts in the provisional ECM, both for evaluation of the physiology of fibroblast invasion and for screening of potential therapeutics.

One such approach utilized a fibroblast-containing collagen matrix, formed on top of a dehydrated/rehydrated fibrin gel in media. Fibroblasts were then able to invade the fibrin matrix. This was used to evaluate the influence of fibronectin during fibroblast invasion into a fibrin matrix, and it was found that fibronectin provides a conduit for fibroblast transmigration from collagenous stroma into the fibrin clot provisional matrix. Fibroblast migration began as early as 24 hours into the assay, but was significantly slowed by the removal of fibronectin (165). This approach was used to further establish the necessity of CD44 and Syndecan-4 Proteoglycan in fibroblast invasiveness (166, 167).

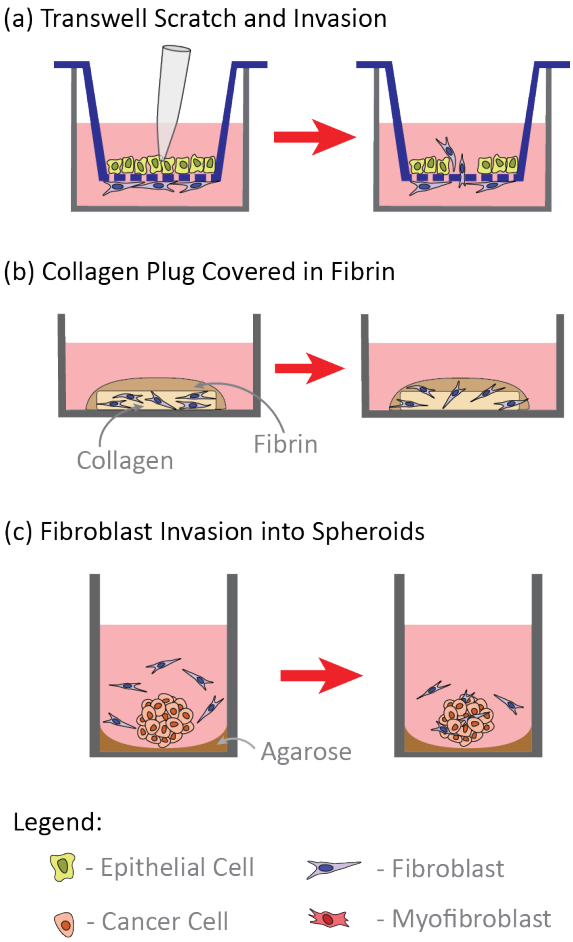

Figure 5.2. Phenotypic assays for invasion. (a) In the Transwell scratch and invasion assay, fibroblasts are seeded on the underside of the Transwell, while epithelial cells are seeded on the top side. The epithelial layer is gently scratched with a pipet tip to remove a section of epithelial cells. After several days of culture, epithelial cells and fibroblasts may migrate into the opened area (4). (b) The collagen plug covered in fibrin assay monitors fibroblast migration from an encapsulated collagen gel out into the surrounding fibrin gel (5). (c) Spheroids were seeded in agarose-coated 384-well microplates. Fibroblasts added after spheroid formation could be observed invading the spheroids (6).

Miron-Mendoza et al. used a similar assay to evaluate the impact of fibrin cross-linking on fibroblast migration. Cell-laden collagen discs were coated with fibrin for an easily imaged cell invasion assay (Figure 5.2B). This was used to show that supplemental fibronectin was necessary for the invasive fibroblast phenotype, and fibroblast-fibronectin network formation was dependent on α5β1 integrin. Fibronectin tracks (fluorescently labelled) were formed at the leading edge of migrating cells and fibroblasts preferentially migrated through pre-existing fibronectin tracks laid down by other cells (5).

Other phenotypic assays for fibroblast invasiveness have focused on migration from 2D adherent culture into fibrin matrices. One such approach used microdroplets of fibroblast suspension patterned on a 6-well plate and covered with a fibrin matrix (168). Through this approach, migration from the 2D culture into the fibrin gel was used to evaluate invasiveness of fibroblasts isolated from patients with acute lung injuries. This was used to evaluate the role of CD44 in mediating fibroblast invasion and subsequent tissue fibrosis. By blocking the function of CD44 with monoclonal antibodies, fibroblast invasion into a fibrin matrix was inhibited (169).

An alternative, matrix-free approach focused on fibroblast invasion into cancer spheroids. This was used for evaluation of therapeutic candidates to combat fibrotic processes in cancer, but could just as easily be applied as a phenotypic assay for invasiveness in other forms of fibrosis. The approach was optimized for 384-well microplates for high throughput evaluation of drug libraries. Tumor spheroids were formed in agarose-coated wells, as depicted in Figure 5.2C. A suspension of fluorescently labeled fibroblasts was then added and invasiveness was evaluated via confocal spinning disc microscopy to locate the fluorescent lung fibroblasts that had invaded the spheroids. A 480-compound library of bioactive substances was evaluated for anti-invasiveness, where prostaglandins and ROCK inhibitors were identified as potential therapeutics (6).

Lewis et al. used a co-culture technique involving a photodegradable PEG-based hydrogel in order to evaluate the impact of crosstalk between fibroblasts and cancer cells on invasiveness of the fibroblasts. An Operetta high content imaging machine was used for high-throughput migration tracking in order to show the increased invasiveness and matrix metalloproteinase (MMP) expression in fibroblasts under the influence of cross-talk with cancer cells compared to fibroblasts alone (170).

Despite the involvement of the fibroblast invasion into the provisional ECM during fibrosis, there remains a question of whether it is necessary for the pathogenesis of fibrotic disease. In the case of pulmonary fibrosis, fibrin deposition does not itself appear to be required for pathogenesis because fibrinogen-null mice are still able to develop lung fibrosis after bleomycin-induced lung injury (171, 172). Assays based on fibroblast invasion into the provisional ECM should therefore establish physiological importance before being used to evaluate compound libraries for potential therapeutic candidates.

5.2.3 Phenotypic assays incorporating fibroblast contraction

A histological hallmark of IPF is the presence of fibroblastic foci, dense clusters of cells and ECM in the lung. The characteristic cell type in these clusters is the myofibroblast. These cells are a differentiated and activated form of fibroblasts, which synthesize collagen and contract the ECM. The myofibroblast is considered the primary effector cell in driving the progression of IPF (173). There are extensive reviews covering the various roles and behaviors of myofibroblasts (173-177). A plethora of biofabrication techniques have been developed to measure contraction, an identifying characteristic of the myofibroblast phenotype. The bulk of these techniques are based on collagen contraction, but there are exceptions. Tuan et al used a fibrin gel scaffold in their model as an analogue to the provisional ECM in wound repair. Gel contraction and collagen production were evaluated in order to show matrix remodeling

under transforming growth factor (TGF-β1) stimulation (178). The use of other hydrogel alternatives to collagen is already covered in detail by other reviews (147, 179, 180).

5.2.3.1 Collagen gel contraction assay

Collagen gel contraction is the gold standard of phenotypic readouts for evaluation of fibrosis, with widespread use. The first reported use of a collagen gel contraction assay established the standard contraction assay format in 1979 (181). When fibroblast-laden collagen gels are cultured in media with serum, they exhibit a high baseline level of contraction, shrinking gels to as small as 1/7th the original area within 24 hours (181, 182). The collagen gel may adhere to the walls of the dish, so most protocols physically detach the gel from the wall using a sterile pipet tip after polymerization. The need for this step limits the throughput of collagen gel contraction assays. These assays are often called floating collagen gels (183). The contraction has been divided into three phases: slow lag phase, rapid contraction phase, and sustained slow contraction phase (184). During the lag phase, fibroblasts recover from trypsinization and elongate along collagen fibers. As previously reviewed (174), tensile force measurements of collagen gels indicated that the lag phase correlates with fibroblast adhesion and cell movement within the collagen gel. Therefore, the lag phase has also been called the traction phase (174). The length of the lag phase can be shortened by using more cells, more serum, or cells at higher passage number (184). Following the lag phase, the collagen gel is rapidly contracted and remodeled, at rates sped up by high cell number or serum concentration and slowed down by higher initial collagen concentration or cytoskeletal inhibitors. Lastly, the system enters a state of slow, prolonged contraction.

Contraction by fibroblasts is regulated to a large extent by TGF-β1 (185), which can be added exogenously to induce contraction (186) or produced or activated by fibroblasts themselves (187), among other sources (187-189). The combination of

TGF-β1 and tensile stress induces fibroblasts to differentiate to myofibroblasts, identified by their expression of alpha-smooth muscle actin (α-SMA), stress fibers, and high contractility (185). It should be noted that tensile stress is also a necessary and critical component for myofibroblast differentiation (190). The capacity for tensile stress within collagen gels can be increased by tethering gels to the dish (181) or altering gelation parameters to form stiffer gels. Gels formed at more acidic conditions down to pH 5.5 have demonstrated higher tensile strength than gels formed at more neutral or alkaline conditions up to pH 8.0 (191). Collagen stiffness can also be increased by using higher concentrations of collagen (192).

Following the initial development of the collagen gel contraction assay, many adaptations to the format have been added. The conventional collagen contraction assay is low throughput and high cost, due to the large consumption of collagen and cells. More modern techniques enable higher throughput with drastically lower collagen gel volumes. In addition to the cost benefit, low volume collagen gels also reduce the diffusion distance necessary for media and relevant exogenous biomolecules (9).

One approach to improve assay consistency is to confine the collagen gel within a glass capillary tube, yielding a single, linear measurement, as in Figure 5.3A (3). Suspended human bladder-derived smooth muscle cells in an uncured collagen solution were aspirated into glass capillary tubes and polymerized. The collagen gels were then detached from the capillary by gently applying air pressure to one end. The capillaries were placed in an incubator inside a petri dish alongside smaller dishes of water to provide supplemental humidity. Over 48 hours of culture, cell viability was consistent between the capillary culture method and the traditional whole well culture method. Due to the diffusive barrier introduced by the glass capillary, the stimulants and inhibitors were added to the gel prior to polymerization. Standard deviations ran close to 1% between replicates. The authors also suggest that the capillary technique

is amenable to future addition of electrical current. Although the capillary technique is limited to short-term culture applications due to diffusive limitations, it provides a consistent, easy-to-read assay that uses low volumes of collagen.

Although fibroblasts can contract collagen gels shortly after seeding, the gel can often attach to the walls and bottom surface of the well, introducing inconsistencies when measuring and analyzing the contraction. In addition to the pipet tip manual detachment method, several groups have developed techniques to consistently seed gels that cover only a fraction of the well area, often employing non-adherent surfaces to further reduce friction (193).

Sage and coworkers published a series of papers using the collagen gel contraction assay, with an array of techniques to reduce gel adhesion. They initially used agarose-coated microwells to reduce the adhesion of the collagen gels to wells (182). In a subsequent study, however, their group designed a water-in-oil system to contain the collagen gel to a small Teflon-coated area in the center of the well, as shown in Figure 5.3B (8). In this technique, a Teflon glass cloth was pinned to the bottom of a 12-well tissue culture well with a Teflon-coated washer. The pieces were then submerged in mineral oil. Collagen with suspended adult human dermal fibroblasts was then pipetted into the center of the Teflon washer ring and incubated to polymerize the gel. Interestingly, the authors found that as the collagen gel contracted, it expelled media, leaving a gel in water in oil 3-phase system. The oil and Teflon modified collagen gel contraction assay performed better than the conventional assay on multiple fronts. The gels maintained a more consistent circularity compared to the conventional assay, wherein gels had a tendency to adhere to the well and form elongated shapes, stretched tightly between the anchor points. In addition to altering the gel shape, the anchor points in the conventional method also prevented full contraction, introducing noise to the measurements.

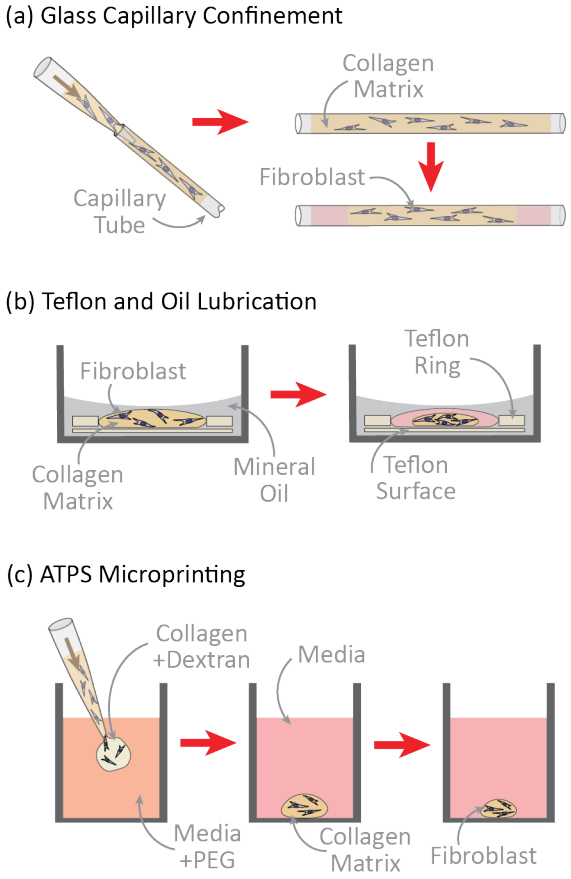

Figure 5.3. Collagen gel contraction assays. (a) Soluble, cell-laden collagen is pipeted into glass capillary tubes. After gelation, the collagen contracts linearly, enabling easy measurement of contraction (3). (b) Teflon-coated surfaces contain the collagen gel, allowing smooth contraction without friction-induced deformations. The mineral oil layer helps confine the gel to the Teflon-coated contraction region (8). (c) Aqueous two-phase systems (ATPS) enable formation of collagen microgels without excessive evaporation by confining soluble collagen to a dextran-rich phase until gelation. The ATPS components are washed out and floating collagen gel contraction assay can commence (9).

Furthermore, conventional assays exhibited cupping, a result of cells sedimenting to the bottom of the collagen gel as it cured, producing vertically asymmetric contraction. In the large gels, cupping can interfere with microscopy, as cells in the center of the gel are pulled to a higher plane than the cells at the bottom of the well. The pre-warmed oil facilitated more rapid polymerization, trapping cells in a more uniformly distributed state. In studies using platelet-derived growth factor (PDGF-BB) to stimulate contraction and measuring the reduction of area, Sage and coworkers achieved standard deviations of roughly 5% between replicates. While the oil and

Teflon technique provides a more uniform and consistent contraction assay, it does lose some of the mechanical stress that has previously been shown to be a driving factor for fibroblast differentiation and activation (190). The authors did not comment on this point. Additionally, the technique is rather low throughput and still uses large volume gels. Nonetheless, their study presents a compelling case for addressing assay consistency. The widespread availability of non-adherent microplates for spheroid culture provide an accessible alternative to the Teflon-coated method.

More recently, ATPSs have been used to generate collagen microgels for contraction assays (9) (Figure 5.3C). Scaling down to 1 µL gels facilitates diffusion of stimulatory or inhibitory proteins and molecules into the center of the gel. However, 1 µL gels evaporate during the 30 minutes collagen polymerization process, often killing the embedded cells. The authors used ATPS to provide an aqueous buffer against evaporation, while confining the collagen and cells into the 1 µL gel during polymerization. ATPS are phase separating solutions similar to oil-water two-phase systems, but both phases contain primarily water. The distinction between phases in this particular ATPS is the presence of immiscible polymers: PEG and DEX. Conveniently, many cells and proteins partition preferentially to one phase, allowing ATPS to be used to spatially confine cells and collagen. After the collagen gel formed, the PEG and DEX were washed out and replaced with culture medium, leaving a 5 µL cell-laden collagen gel. This technique is compatible with conventional liquid handling tools and imaging, making it appropriate for high-throughput studies. A follow-up study used the technique to produce 1 µL collagen gels and showed excellent robustness of the technique to assess cytotoxicity in collagen gels (194). However, the consistency and reproducibility of the microgel technique to assess contraction have not yet been established.

Several microfluidic approaches have facilitated formation of sub-millimeter collagen gels, as reviewed recently (195, 196). These techniques use photolithography

to generate channels 10s to 100s of microns in width for precise and controlled fluid mixing. Flow-focusing devices introduce a collagen-containing aqueous phase into a stream of oil to produce microdroplets of controlled size (197). Several groups have utilized these device geometries to generate and cure cell-laden collagen microgels 10s to 100s of microns in diameter (198-200). However, these studies have not yet examined the use of microfluidic collagen microgels in contraction assays.

5.2.3.2 Mechanics of collagen gel contraction

In parallel with the development of techniques for assay consistency and throughput, several groups have designed methods to measure more detailed mechanical information from collagen gel contraction assays. Liu et al. demonstrated the importance of substrate stiffness in pulmonary fibrosis by generating a stiffness-gradient collagen gel using photopolymerization of polyacrylamide (201). They showed that fibroblasts are more active and responsive to TGF-β1 on stiff substrates and less active on soft substrates. The lack of fibroblast activation was also found by inhibiting focal adhesion kinase formation with prostaglandin E2, a metabolic product produced by epithelial cells that has also been shown to suppress fibroblast activation in co-culture (202). This technique was demonstrated as both a stiffness gradient gel and a 96-well discrete stiffness array, highlighting its versatility in probing the contractile phenotype of fibroblasts.

A separate study used agarose to modulate collagen gel stiffness (203). More agarose yields stiffer gels, which can activate fibroblasts (201). However, the agarose also sterically obstructs collagen presentation to the cells, inhibiting the ability of the cells to cross-link and locally stiffen the matrix (203). This study indicated that collagen concentration can increase contractility by increasing ligand availability. The competing factors of agarose-to-collagen ratio and the collagen concentration allow fine tuning of both collagen stiffness and ligand availability.

Although the strength of fibroblast contraction can be inferred in relative terms by monitoring the shrinkage of the collagen gel, more granular mechanical information requires more advanced techniques. A variety of mechanical sensors and accompanying theoretical frameworks have been built into or applied externally to the collagen gels (204, 205). Harley et al. made a collagen-glycosaminoglycan scaffold by freeze-drying (206). The process generated somewhat uniform structures with repeating lattice units, allowing for single-cell microscopic measurements to be incorporated into a whole-gel solid mechanics model. The authors generated both homogeneous, isotropic structures and heterogeneous structures for comparison. They used an Euler model of buckling stress to determine how much force a cell must exert on the lattice to buckle a strut, given the strut's thickness and the overall elastic modulus of the material. Depending on the thickness of a given strut, the dermal fibroblasts exerted contractile stress of 11 to 52 nN per cell. The authors examined many individual cells buckling struts of various thicknesses and found an upper bound of 450 nN, which the cell was unable to contract. The mode of contractile failure was proposed to be at the focal adhesion. While this model provides granular information about the mechanical stresses exerted by cells, the collagen glycosaminoglycan structure represents a far stiffer matrix (~5 MPa linear elastic modulus) compared to the healthy or fibrosis lung (1-20 kPa) (201). The analysis provided in this study could be adapted in future studies examining biofabricated materials with stiffness more relevant to pulmonary fibrosis, as well as biochemical stimuli relevant to IPF.

Another treatment of collagen gel contraction mechanics derived a solid mechanics model around a cylindrical collagen disc model (207). The model assumes an incompressible solid with a non-linear strain-dependent elastic modulus. It uses linear elastic mechanics to relate the area reduction and the elastic modulus (measured with a nano-indentation probe) to the bulk cell contraction force. These calculations yielded a contractile force of 1.41 nN (baseline) to 4.15 nN (activated) per

human aortic adventitial fibroblast cell. The differences in substrate stiffness and cell type confound any comparisons between this method and the collagen-glycosaminoglycan scaffold calculations. One drawback to this model is the incompressible solid assumption. Several studies cited in this review indicate the collagen gels lose water as they compress and decrease volume (3, 8), invalidating the incompressible assumption. Nonetheless, this model provides a general method to approximate contractile forces from area reduction measurements for cylindrical collagen gels.

5.2.3.3. Strain gauge techniques

Several techniques have been developed to measure contractile forces using macroscale (208) and microscale strain gauges (204). In most of these systems, cell-laden collagen gels are formed to span between two anchors. One or both of these anchors acts as a strain gauge. Early methods used large electronic strain gauges, converting the strain (or displacement) into a change in resistance using piezoelectric materials (208). If the geometry and elastic modulus of the anchoring material is known, the force exerted by the cells can be calculated. Modern methods apply the same principle, but use microscale anchors and detect strain by time-lapse imaging. Because the force exerted by cells is relatively small, strains on the materials commonly used for cell culture (plastics, PDMS, etc.) can be difficult to detect. A common workaround forms the scaffold into tall micropillars, where the long torque arm and cantilever action amplifies the distance that the micropillar moves in response to the nN-scale cell contractile forces (204).

Another technique to measure the contractile force of fibroblasts used supersoft PDMS to generate microposts inside donut-shaped wells, as shown in Figure 5.4A (2). Although hydrogels and other supersoft materials can be produced, these materials often suffer from tearing during demolding in traditional replica molding

techniques. The supersoft PDMS technique addressed the problem by using 'hard candy' recipes to generate sacrificial replica molds (2). This technique enabled fabrication of PDMS microwells with 200 μm diameter microposts and an elastic modulus on the order of 0.1 kPa. Fibroblast-laden collagen gels were centrifuged into the microwells, where they formed a ring around the post. When the fibroblasts contracted, they squeezed the post. Solid mechanics analysis enabled the calculation of contractile force on the post by measuring the reduced post area. The authors reported the force exerted as a bulk radial stress and did not calculate a per-cell force. The authors also demonstrated the ability to detect an initial contraction, apply an inhibitor, then see the cells and the post relax back toward its original shape, demonstrating the elastic compression.

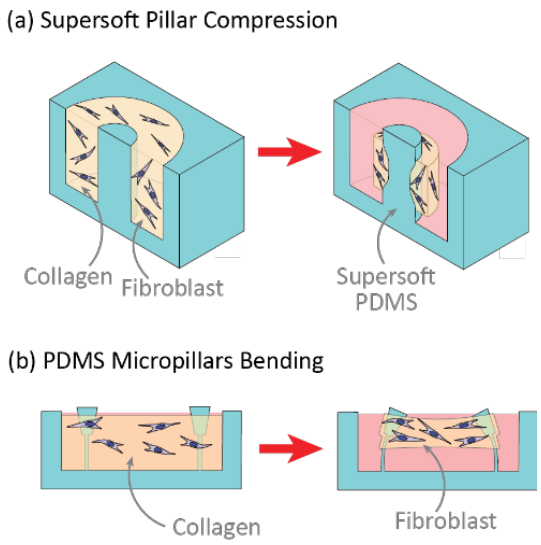

Figure 5.4. Microfabricated devices for fibroblast contraction. (a) Cell-laden collagen gels are formed inside of microfabricated, supersoft, donut-shaped wells. The cells are able to contract and deform the low elastic modulus pillars (2). (b) Cell-laden collagen gels are seeded around micropillars. When the cells contract, the micropillars bend as predicted by cantilever solid mechanics (7).

Chen et al. modified the tethered collagen gel format to work at the microscale, as shown in Figure 5.4B (7). They tested epithelial cells by treating the cells with multi-walled carbon nanotubes (MWCNTs) in the culture flask prior to seeding in the

microdevice. Cells were then suspended and seeded into the microdevices along with type I collagen by centrifugation. The microtissues formed and detached from the outer walls within 12-24 hours, with cultures lasting for 1 week without detaching from the micropillars, due to their goblet shape. The authors found that low concentrations of MWCNTs increased contraction force, while high concentrations inhibited contraction force. The low dose conditions corresponded to a state of inflammation and activation, indicated by contraction, presence of reactive oxygen species (ROS), and miR-21 expression. The high dose caused considerable cell death, offsetting the activation, as measured by the contraction force. This study demonstrates the need for multifactorial analysis of phenotypic screens, as counteracting influences may confound the interpretation of results. In this case, measurement of both cell activation (contraction force and ROS production) and cell viability elucidated the behavior along a dose-response curve that indicated peak bulk pathologic behavior at a medium concentration.

The same group used a similar approach to evaluate anti-fibrotic therapeutics using their in-vitro assay (209). Fibroblasts were suspended by micropillars in a super thin (35 - 55 um) collagen layer arranged in a leaflet shape in order to mimic the geometry of alveoli. Contractile forces in the collagen were measured by deflection of the micropillars that suspended the collagen and differentiation of fibroblasts into myofibroblasts was confirmed by staining for α-SMA. This assay was then used to evaluate the therapeutics Nintedanib and Pirfenidone through measurement of both changes in tissue compliance and differentiation of fibroblasts into myofibroblasts. This paper also used an alternative implementation of the micropillar supported collagen membrane to evaluate traction bronchiectasis. By modulating the rigidity of the micropillars, it was shown that increased stiffness in lung tissue due to fibrosis would compound lung damage as seen in traction bronchiectasis.

Direct Contact ALI with Contraction

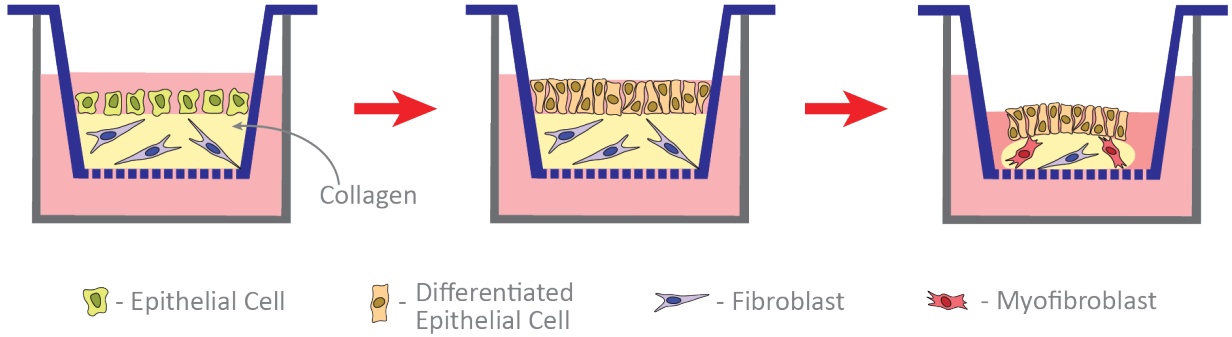

Figure 5.5. Epithelial cells are seeded on top of a fibroblast-laden collagen gel in a Transwell insert. After confluence is reached, culture media is removed from the top well, generating an air-liquid interface culture. The epithelial layer differentiates in response to the air-liquid interface. After stimulation, the collagen gel contracts, separating from the walls of the well (1).

5.2.3.4 Co-culture collagen gel contraction assays

The interplay between epithelial cells and fibroblasts may be a key component of pulmonary fibrosis pathology (141). In an early study, A549 or bronchial epithelial cells were seeded directly on top of fibroblast-laden collagen gels (210). Compared to the fibroblast monoculture, the co-culture gels showed less total contraction over 15 days. The authors fit an exponential decay curve to the area reduction, finding that the co-culture gel had the same time constant as the monoculture, despite the differences in total contraction. Furthermore, the authors used two-photon microscopy to show that co-culture decreased the degree of collagen crosslinking, as inferred by two-photon fluorescence intensity.

In another co-culture study, Ishikawa et al. prepared a similar collagen contraction gel with human bronchial epithelial cells seeded directly on top of the gel. However, this study also introduced air-liquid interface culture, as depicted in Figure 5.5 (1). These gels were not manually detached and remained in place for 21 days before stimulation. The gels detached by cell contraction when cells were stimulated with TGF-β1. Histology slices of the microtissue demonstrated that TGF-β1 also induced a decrease in epithelial layer thickness. Immunostaining in these histological slices also revealed changes in MMP and tissue inhibitor of metalloproteinase (TIMP) expression due to the crosstalk between co-cultured cells. These techniques demonstrated the synergistic effects often seen in co-culture approaches.

The biochemical mechanisms of epithelial-fibroblast co-culture have been reviewed (150). Growing evidence indicates that epithelial cells secrete a variety of biochemical signals to regulate fibroblast behavior. Biofabrication of phenotypic IPF assays would benefit from consideration of this cross-communication.

5.2.3.5 Alternative techniques to measure fibroblast contraction

A recently developed technique enables measurement of cell contraction based on the cell coverage of the culture surface. The xCELLigence platform uses electrodes patterned on the surface of a culture plate to measure the electrical impedance past the cells (211). As the cells contract, they tighten and narrow, exposing electrode surfaces. The exposed surfaces pass current more easily, as the resistance from the cells is removed. One of the key benefits of this technique is its rapid response time. However, that may be more useful in studies of rapid contraction, as seen in muscle and cardiac tissues rather than the progressive contraction typically observed in fibrosis.

5.2.3.6 Discussion of contraction assays

As the key effector phenotype of IPF, considerable progress has been made to develop biofabrication techniques assessing contraction. However, one key phenotype that is missing from these cell-based contraction assays is the divergence between physiological contraction, which resolves, and pathophysiological contraction, which persists and progresses. The standard collagen gel contraction assay moves only in the direction of contraction, with little consideration or potential for reversal. The ability of epithelial cells to delay activation and contraction of fibroblasts (1) presents a promising building block for future biofabrication of assays that reflect IPF resolution.

5.2.4 Phenotypic assays incorporating collagen production and deposition

In addition to collagen contraction, the production and deposition of new collagen by fibroblasts is a key event in disease progression. A study of kidney mesangial cells in 2D culture indicated that they respond to TGF-β1 by forming clusters, or nodules, that somewhat resemble the nodules seen in human pulmonary fibrosis (212). Immunostaining of these nodules indicated localized deposition of collagen. The nodule assay was later adapted in several different publications, one of which used the assay to screen Chinese herbal medicine extracts for inhibition of

kidney fibroblast nodule formation (213). Another similar study found that macromolecular crowding with dextran sulfate causes much higher collagen deposition by fibroblasts (214). Neutral macromolecular crowding with Ficoll produces less elevated, but more sustained collagen deposition with greater cross-linking. Collagen deposition was assessed and screened using immunochemical staining and optical microscopy of the cluster formation. This 2D method lacks the complex microenvironment of some of the other techniques, but it does provide disease-relevant information by assessing the collagen deposited by the fibroblasts.

5.3. Future directions and conclusions

Considerable progress has been made in the past two decades to biofabricate complex 3D lung culture environments that recreate aspects of pulmonary fibrosis. These extend from epithelial damage, to fibroblast invasion, contraction, and deposition. Furthermore, some of these techniques have been adapted and applied to medium-throughput phenotypic screens for potential therapeutics.

However, there remains unexplored territory, particularly in the areas of provisional extracellular matrix and long-term disease progression. These two areas present particularly challenging aspects for cell-based assays. Clotting is a complex process involving many different factors from blood. Incorporation of endothelial compartments or fibrin assays has somewhat addressed the issue. Recent literature implicates aging and fibroblast senescence as key differences between fibrotic and healthy tissue in both animal models (215) and in human patients (216). The role of senescence in fibrosis has been reviewed recently (143). Maintaining long-term culture has proven difficult, although multicellular systems has shown some success, including the direct contact epithelial-fibroblast culture that lasted 21 days (1). Furthermore, we have deliberately neglected the ever-present immune system in this review. The exact role of the immune system in IPF remains controversial and the challenges

surrounding biofabrication of immune components are immense, but new work in this area could have tremendous benefits.

Development of future phenotypic assays should carefully consider the unique features of the lung environment: mechanical compliance, tissue geometry, and the composition of cells and matrix proteins. Furthermore, selection of appropriate readouts will be critical to answering the right questions about disease progression. If the assays are to be adapted to high-throughput screens, then extensive optimization of the reproducibility and performance of the assay should be performed. Biofabrication of culture models that enable phenotypic screening of pulmonary fibrosis presents a compelling approach to finding new therapies in pulmonary fibrosis and potentially other related aberrant wound healing diseases.

Chapter adapted from Yamanishi C, Robinson S, Takayama S. Biofabrication of phenotypic pulmonary fibrosis assays. Biofabrication. 2019;11(3):032005, with permission from IOPscience.

Table 5.1. Biofabricated phenotypic assays for pulmonary fibrosis.

Technique	Cell types used	Exogenous materials	Scale	Additional equipment	Phenotypes	Ref
Scratch wound assay	NA	None	Any	None	Re-epithelialization	(163)
Alveolar epithelial stretching damage	Rat alveolar epithelial type II cells	Silicone membrane	1-well custom device	Cam motor, gasket setup	Cell death	(153)
Alveolar epithelial stretching damage	Mouse alveolar epithelial cells	PDMS membrane	1-well custom device	Syringe pump, microfabrication	Cell death and detachment from surface	(154)
Transwell co-culture	SAEC and endothelial	Transwell	6-well	None	Protein expression...?	(157)
Transwell with aerosol exposure	A549	Transwell with 1 μm pore	6-well	Nebulizer, gas containment chamber	Viability, cytokine expression	(159)
Photodegradable microbeads in hydrogel co-culture	A549, human normal lung fibroblasts CCL-210.	Home-made microspheres, hydrogels	24-well plate	Operetta high content imaging system (Perkin Elmer)	Migration	(170)
Transwell scratch and invasion	A549 and fibroblast (NHLF vs IPF)	Transwell with 8 μm pore	6-well	None	Migration, wound closure, re-epithelialization	(4)
Tethered fibrotic microtissue array	Primary NHLF, human primary SAECs	PDMS, collagen, matrigel, fibronectin	8x8 microtissue array	Micropillar PDMS device	Contraction, tearing epithelial layer, activation	(209)

Table 5.1 (continued).

Technique	Cell types used	Exogenous materials	Scale	Additional equipment	Phenotypes	Ref
PDMS micropillar tethered collagen gel	BEAS-2B normal lung epithelial cells	PDMS micropillars, collagen	10x13 array in 35 mm dish	Microfabrication	Contraction	(7)
Fibroblast invasion from collagen into fibrin	Human adult dermal fibroblasts	Dried fibrin gels, collagen, fibronectin	24-well	None	Invasion	(166)
Fibroblast invasion from 2D into fibrin gel	Isolated human lung mesenchymal cells	Fibrinogen, thrombin	6 well plate	inverted phase contrast microscope	Invasion	(169)
Fibrin contraction Assay	Human Dermal Fibroblasts	Fibrinogen, thrombin,	48 well plate	inverted microscope to measure height	Proliferation and collagen synthesis	(178)
Fibroblast invasion into spheroids	T47D (breast cancer), MCF7 + H1299 (lung cancer), HPF (pulmonary fibroblasts)	480 compound library	384 well	agarose for non-adherent surface for spheroid formation	invasiveness	(6)
2D nodule formation assay	Many different cells examined	None	96-well	None	Nodule formation	(212)
Stiffness gradient collagen gel	Human lung fibroblasts (CCL-151)	Collagen, acrylamide, bisacrylamide, Irgacure 2959	96-well	UV light source	Activation, collagen production	(201)
Aqueous two-phase system microprinting	HEK 293, NIH 3T3, MC 3T3	Polyethylene glycol, dextran, collagen	96-well	Robotic pipettor	Contraction	(9, 194)

Table 5.1 (continued)

Technique	Cell types used	Exogenous materials	Scale	Additional equipment	Phenotypes	Ref
Floating collagen gel contraction	Human foreskin fibroblasts monoculture	Collagen	100 – 500 µL	None	Contraction	(181)
Low-adherence plates facilitated collagen gel shrinkage	NB1RGB normal human dermal fibroblasts	Collagen	12-well	Flexcell compression	Contraction	(193)
Glass capillary confinement	Primary human bladder-derived smooth muscle cells	Glass capillary	48-well	None	Contraction	(3)
Supersoft micropost lithography	HS-5 stromal fibroblast cell line	Microfabricated device	Not reported	Microfabrication	Micropost area reduction	(2)
Teflon and oil lubrication	Normal adult human dermal fibroblasts	Teflon-coated glass, teflon-coated washer, mineral oil	12-well	None	Contraction	(8)
Direct contact collagen gel co-culture	A549, 16HBE14o-, CCD-18 lung fibroblast	Collagen	24-well	2-photon microscope for collagen sub-analysis	Macroscopic & microscopic contraction	(210)
Direct contact ALI with collagen gel contraction	IMR-90 human fetal lung fibroblasts, normal human bronchial epithelial cells (HBECs)	Collagen	12-well	None	Gel contraction	(1)
Electrical impedance	Human primary bronchial smooth muscle cells (BSMCs), primary lung fibroblasts (HLFs)	Gold electrode arrays	96-well	xCELLigence RTCA MP instrument	Contraction	(211)

Table 5.1 (continued)

Technique	Cell types used	Exogenous materials	Scale	Additional equipment	Phenotypes	Ref
Nano-indentation with collagen gel contraction to measure contractile forces	Human aortic adventitial fibroblasts	Collagen type I	35 mm dish	Depth-sensing nanoindentation tester	Contractile force	(207)
Collagen gel tethering	Normal and diseased human and calf skin fibroblasts	Strain gauge	1-well device	Custom strain gauge	Direct force measurement via strain gauge	(208)
Microfluidic droplet generation	3T3 fibroblast cells	porcine gelatin, rat tail collagen type I	1 nL gels, continuous production	Blue LED for photocrosslinking, microfabrication	Not reported	(198)
Optical measurement of collagen cluster formation	Normal primary human lung fibroblasts (WI-38)	Macromolecules (optional)	24-well	None	Deposition	(214)
Collagen microsphere generation	MDA 231 cells	Collagen	200 μm microgels, continuous	Microfabrication lab	None	(199)
Agarose-embedded collagen gels	U373-MG human glioma cells	Collagen, agarose	Not clear	None	Contraction	(203)

CHAPTER 6 Kinetic Analysis of Label-Free Collagen Gel Contraction Using Machine Learning-Aided Image Analysis

6.1 Introduction

Pulmonary fibrosis is a deadly lung disease, characterized by an aberrant wound healing response (140). Although progress has been made in understanding disease mechanisms, effective therapies have not yet been shown (217). Part of the difficulty in studying pulmonary fibrosis arises from the complex interplay between different cell types, mechanics, genetics, and the microenvironment (140, 142, 152, 218). Phenotypic assays, which can measure more holistic responses than gene or protein expression assays, are an important, complementary set of tools to understand cell and tissue processes (134).

One of the classic phenotypic assays for pulmonary fibrosis is the collagen gel contraction assay (181). In this assay, fibroblasts are embedded into a collagen gel, which is detached from the surface of its container – usually a microplate well. Activated fibroblasts remodel the collagen gel, macroscopically shrinking the gel in a process similar wound closure. Despite the assay's utility and reliability in cell lines, the behavior of primary lung fibroblasts can be more subtle and difficult to detect (219-221). These differences arise, as primary cells have variable initial states and sensitivities to stimulation. Primary cells present additional challenges, as they have limited growth capacity. Furthermore, the throughput has previously been low, as the collagen gel contraction assay traditionally requires the user to manually detach the gel from the edges of the well with a pipet tip (181). Measurement of the contracting area has also been manual, with pictures taken daily and images traced by hand. To address these issues, we explore methods to increase the throughput of the assay and incorporate continuous imaging. Our lab has previously developed a high throughput collagen microgel bioprinting technique and demonstrated its effectiveness with cell lines (9). In this assay, evaporation

of the microgel during curing is prevented by mixing the collagen and cells with an aqueous solution of DEX, which forms an ATPS with an aqueous solution of PEG. Collagen mostly remains within the DEX phase as it cures (222), while the PEG phase provides an aqueous buffer, containing the collagen and limiting evaporation. In this study, we extend the ATPS collagen bioprinting technique and examine contraction kinetics of normal vs diseased primary human lung fibroblasts, particularly in the context of anti-fibrotic drugs.

6.2 Materials and Methods

6.2.1 Cell Culture

Normal human lung fibroblasts (NHLF, lot 655309) and idiopathic pulmonary fibrosis human lung fibroblasts (IPF, lot 627840) were purchased from Lonza (Walkersville, MD). These primary cells were cultured in complete Fibroblast Growth Medium (FGM-2, Lonza) and used from passages 2-5. For collagen gel contraction assays, cells were passaged into FGM-2, without serum or FGF (FGM-SF), then seeded into collagen gels the following day at ~75% confluence.

6.2.2 Collagen Microgel Contraction Assay

Collagen microgel contraction assays were seeded as previously described (9). 96-well round bottom microplates were filled with 100 µL per well of 6% (w/w) PEG, MW 35,000 dissolved in serum-free DMEM (Gibco) with 10% distilled water (Gibco) to adjust for osmotic pressure. This plate was warmed to 37C in a 5% CO_2 incubator. A collagen-detxran mixture was prepared on ice, consisting of 6% (w/w) DEX T500, 2 mg/mL Type I bovine skin collagen (Advanced Biomatrix), and 5 mM NaOH to neutralize the collagen. This mixture was mixed by pipetting up and down on ice, with care taken to avoid introducing bubbles. The mixture was kept on ice while cells were prepared for seeding. Cells were washed with PBS, then trypsinized with 0.25% Trypsin (Gibco). After the cells lifted, the cells were quickly diluted in FGM-SF and centrifuged at 200xg, 5 min, room temperature. After aspirating the supernatant, cells were resuspended in 1 mL FGM-SF

and counted. Appropriate volumes of resuspended cells were centrifuged again and resuspended in DMEM. The cells were then mixed 1:1 with the collagen mixture to generate a 1 mg/mL collagen, 3% DEX solution. The collagen-DEX-cell suspension was transferred to a 96-well plate for seeding, where the DEX-cell suspension would be seeded into the wells containing PEG, as in Figure 6.1.

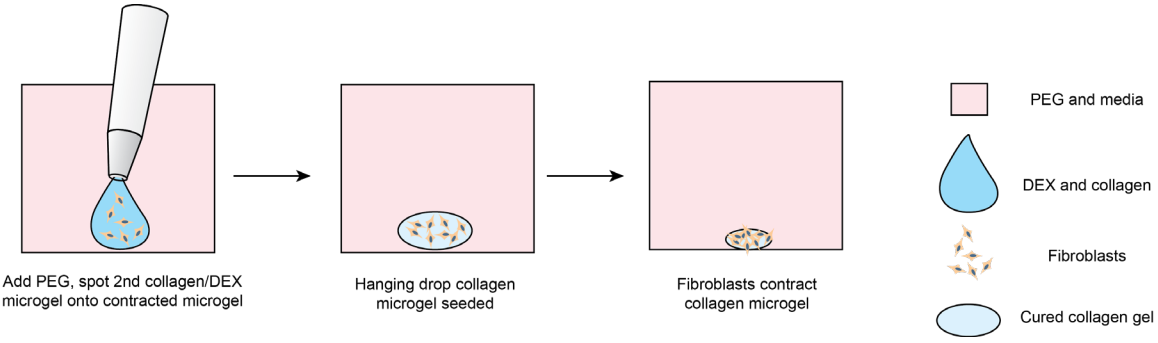

Figure 6.1. Schematic of ATPS collagen micro-gel contraction assay

6.2.3 Liquid Handling

A Cybi-FeliX liquid handler was used to transfer 5 µL of the collagen-DEX-cell suspension into the microplate containing PEG solutions. The microgels were incubated at 37C in a 5% CO2 incubator for 30 minutes to cure the gels. After curing the gels, all wells in the microplate were washed simultaneously using the liquid handler. Gel washes were performed by withdrawing down to 25 µL to avoid pipetting the gel, then adding and removing 50 µL PBS (4x) to remove PEG, then 4x more with FGM-SF, and finally refilled to 100 µL with a 2x concentrated solution of the desired stimulant in FGM-SF. To avoid withdrawing the microgels, aspiration and dispense speeds were set to 5 µL/s.

Collagen microgels were incubated and imaged using an Incucyte in-incubator microscope system. 4x brightfield images were acquired at 1-hour intervals for 2 days, then at 6-hour intervals for the next 6 days.

6.2.4 Drug Response Studies

Cell-laden collagen microgels were stimulated with or without 10 ng/mL TGF-β1 (R&D Systems) and anti-fibrotic drugs: Nintedanib (Selleck Chem), Pirfenidone (Selleck Chem), and the focal adhesion kinase inhibitor PF 431396 (Tocris) at specified concentrations. These collagen microgels were imaged over 8 days to monitor contraction. To determine the half maximal inhibitory concentration (IC50), the AUC of the area over time graph was calculated for each individual gel as a parameter of overall contractility. These values were normalized, such that a gel with no contraction would have a normalized AUC of 100%. The IC50 was determined to be the concentration of an inhibitor at which the normalized AUC was halfway between the corresponding inhibitor-free control and 100%. IC50 determinations were considered for stimulated NHLF and unstimulated IPF, as the IPF are highly contractile independent of TGF-β1 stimulation.

6.2.5 Wash Efficiency Measurements

To assess the removal of ATPS reagents, fluorescent molecules were used. PEG solutions were spiked with 1 ng/mL fluorescein. The average fluorescent intensity per field of view was measured using the Incucyte prior to and after washing the collagen gels with the automated liquid handler to determine how much fluorescein, and by proxy, how much PEG was removed. To asses removal of DEX from the collagen gels, 1 μg/mL FITC-DEX MW 500,000 was spiked into the collagen-DEX-cell mixture and seeded into the PEG plate in separate wells. Again, the average fluorescent intensity per field of view was measured using the Incucyte before and after washing.

6.2.6 Cell Viability

Cell viability was measured using a Calcein AM, ethidium homodimer LIVE/DEAD stain (ThermoFisher). 1 μM of Calcein AM and 1 μM of ethidium homodimer in PBS were added to the collagen microgels and incubated for 1 hour. Fluorescent images were then acquired and quantified using the built-in Incucyte software.

6.2.7 Image Processing

Collagen microgel areas were quantified using three methods: manual, Incucyte, and trainable WEKA segmentation. For manual quantification, gel perimeters were traced using ImageJ and areas were measured. For Incucyte quantification, images were segmented using the built-in Incucyte 2019A segmentation software from the Spheroid Module. In the trainable WEKA segmentation plugin from FIJI (ImageJ), 1-10 representative microgel images were annotated and used to train the classifier. We wrote a new plugin to iterate through a folder of images exported from the Incucyte 2019A software, apply the WEKA classifier, run quality checks, measure areas, and generate a .csv file containing areas, well positions, and times.

6.3 Results and Discussion

6.3.1 Optimization of Automated Seeding and Culture

Initially, the introduction of air bubbles into the collagen gels was problematic. Visual examination of the PEG plate and the collagen-DEX-cell solution indicated that neither were the source of bubbles. We then suspected that the relatively high viscosity of the collagen-DEX-cell solution was causing the solution to have delayed flow into the pipet tips, pulling a small pocket of air after the tip was lifted out of the seeding solution. That air pocket was then trapped when the pipet was introduced into the PEG solution, producing a bubble along with the microgel. This was confirmed by withdrawing additional fluid into the pipet and serially seeding multiple gel plates. Each plate contained 1-2 bubbles per gel. To address the problem, we programmed the liquid handler to pre-dispense 0.5 µL above the surface of the PEG, then submerge the tip into the PEG solution and dispense the remaining 4.5 µL. No satellite gels were introduced using this method.

Initial tests indicated that parts of the collagen microgels were being aspirated during the washing step. To address this issue, the liquid handler was programmed to aspirate and dispense at the outer edge of the well. Subsequent imaging indicated that all of the microgels survived washing intact with washes performed at the outer edge of the

well and 5 μL/s pipetting speed. Despite the low pipetting speed measurements of fluorescein in the PEG solution indicated a 98% reduction in background-subtracted fluorescence by washing. In contrast, DEX proved more difficult to remove. Microgels seeded with FITC-DEX had only a 14% reduction in background-subtracted fluorescence immediately following washing. However, there was a 72% reduction in background-corrected fluorescence 24 hours after the washing step. This is likely due to the low diffusivity of high molecular weight DEX in collagen. Note that the cells retained 94% viability after seeding and washing (n=3, SD=1%).

6.3.2 Validation and Optimization of Machine Learning Image Processing

To quantify collagen microgel area, we initially examined the built-in Incucyte segmentation software. However, the software performed poorly with microplate imperfections and gels at early time points, when they are relatively translucent. We next examined WEKA Trainable Segmentation, a machine learning plugin included in the open source image processing program, FIJI (ImageJ). Figure 6.2 shows the process for training the WEKA Segmentation classifier. After loading an image sequence into FIJI and selecting Trainable WEKA Segmentation, the background area is manually identified with the cursor and marked as Class 1. Gel areas are similarly marked as Class 2. After training a classifier, additional annotations can be added to revise the classifier until it performs adequately. Once a satisfactory classifier has been found, it is saved for future use.

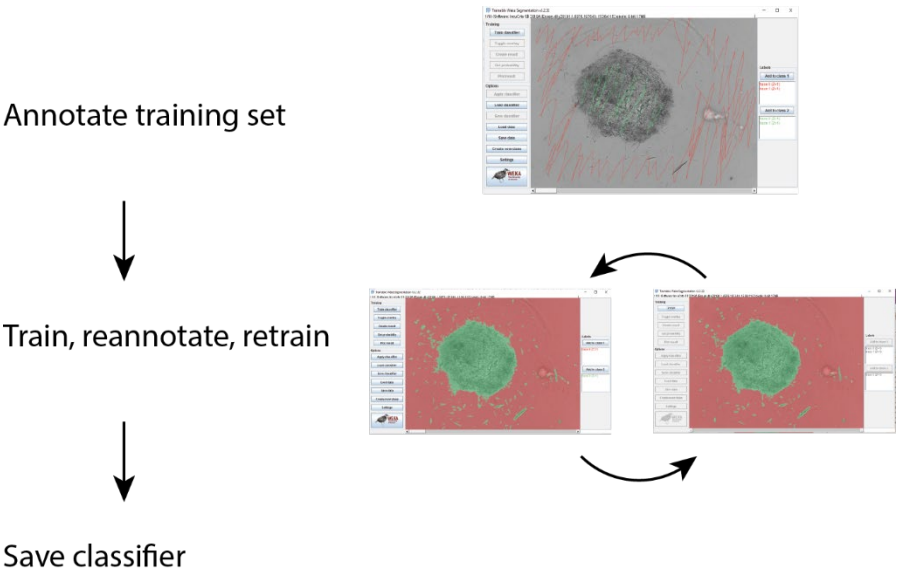

Figure 6.2. Training the classifier for WEKA Segmentation.

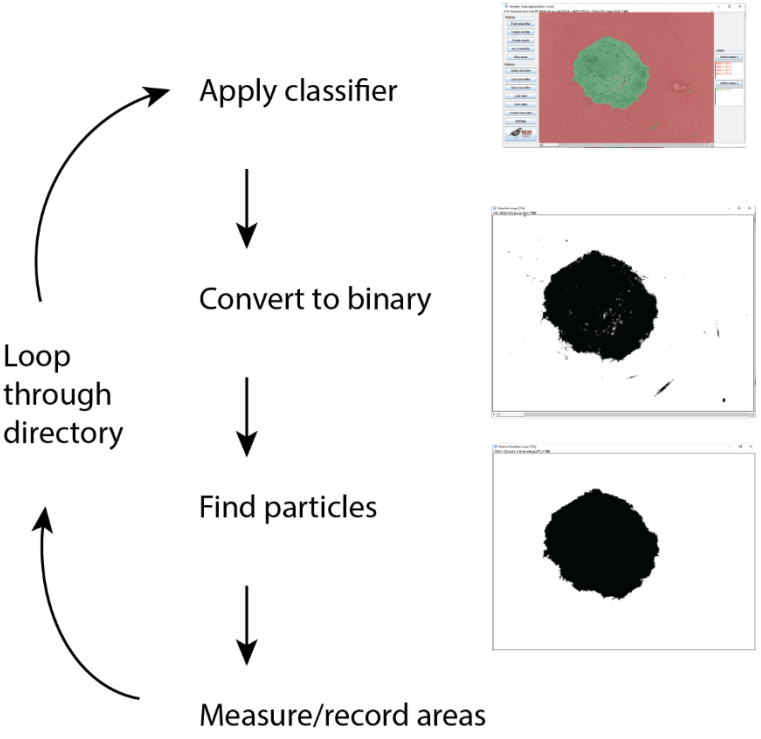

Figure 6.3. Applying trained WEKA Segmentation to measure gel areas.

To analyze large sets of images exported from the Incucyte in-incubator microscope, a FIJI plugin was written. This plugin uses the built-in Trainable WEKA

Segmentation plugin to apply the saved classifier to each image in a directory, as in Figure 6.3. Following classification, the image was converted to binary and the largest particle was found using the built-in particles function. Areas and metadata were then recorded.

During initial testing on an Intel® Core™ i7-7700 CPU at 3.60 GHz, classification of a single image took 15 s. Further exploration revealed that smaller training sets enabled faster classification. The iterative training process in Figure 6.2 allowed for fine-tuning small training sets to achieve accurate segmentation without sacrificing speed.

To validate the automated image analysis algorithm, 300 images of microgels from early and late time points were manually annotated for comparison of area measurements. A strong correlation with manual area measurements was achieved (Figure 6.4) at 3 s per image.

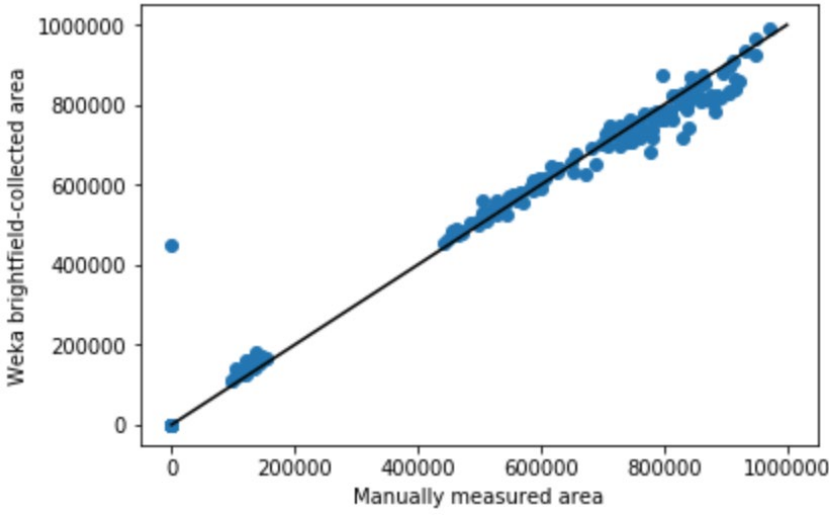

Figure 6.4. Correlation plot of WEKA Segmentation and manual area annotation.

6.3.3 Collagen Microgel Contraction Kinetics

We examined the performance of the ATPS collagen microgel contraction assay with NHLF and IPF responses to TGF-β1 stimulation at high dose (10 ng/mL) using our automated seeding, washing, and image processing system. The NHLF had slower

baseline and activated contraction compared to IPF. TGF-β1 induced a moderate increase in the rate of contraction for both cell types, as shown in Figure 6.5.

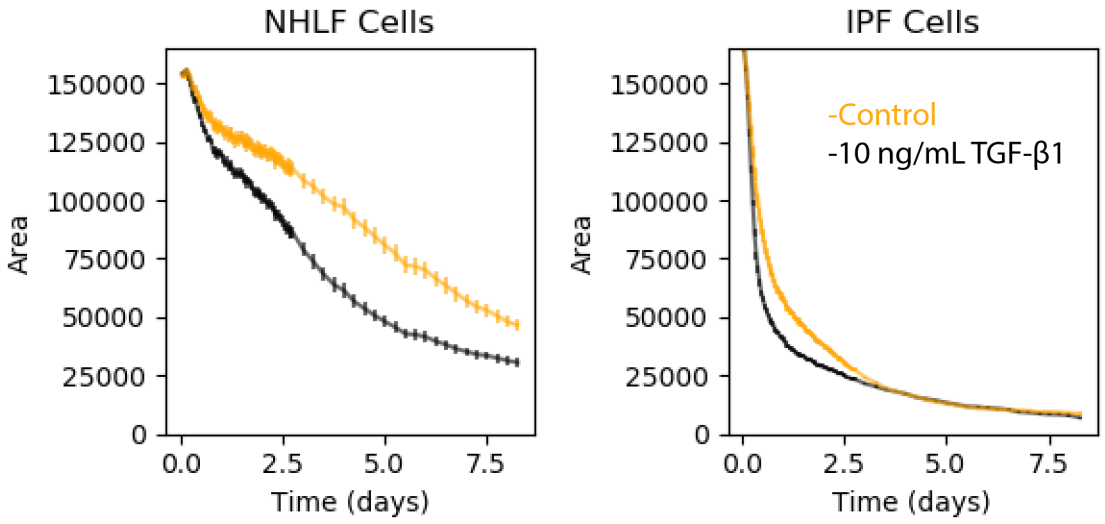

Figure 6.5. Contraction of NHLF and IPF in response to stimulation with 10 ng/mL TGF-β1. Error bars are standard error of the mean, n=15 per condition.

To assess the potential of this assay as a platform for high-throughput drug discovery, we calculated the Z statistic. The Z statistic compares the variance of an assay to the difference between the means of positive and negative controls. A perfect assay Z statistic is 1.0, an excellent assay is 0.5-1.0, a good assay is 0.0-0.5, and anything below 0 may not be appropriate for high-throughput screening. We calculated a Z statistic for each individual time point, as well as for the area under the curve for each individual gel, using 10 ng/mL TGF-β1 with NHLF as the negative control (no inhibition) and no TGF-β1 with NHLF as the positive control. With these controls, the Z factor increases over time, peaking at -0.7 near day 4 (Figure 6.6). To aggregate the time course data, we also calculated the area under the curve of the area vs time graph for each collagen microgel. The area under the curve mimics the best performing individual time point, but does not

cross into the range of a useful high-throughput screening tool with this set of controls. Therefore, this assay is inappropriate for use as a primary high-throughput screening tool.

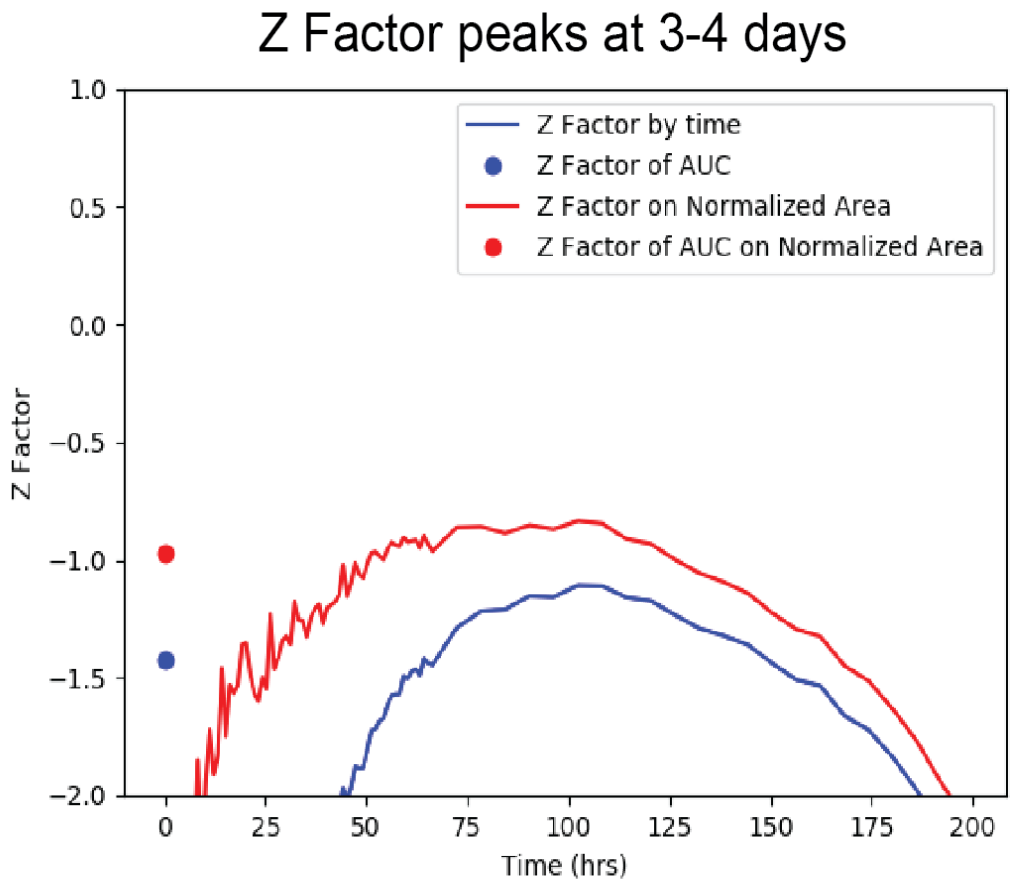

Figure 6.6. Z Factors for set time points. The Z Factor was calculated for aggregate data (n=30 replicates) for each individual time point, as well as for the AUC of each gel contraction curve.

A close examination of the individual gels demonstrates why this assay would be inappropriate for high-throughput screening of drug candidates. Although the mean area is markedly different between +/- TGF-β1 controls, individual microgels at the outer ends of the population distribution overlap, generating false positives and/or false negatives in a screen of unknown drugs, despite the stark differences between populations that are seen when using the industry-standard reporting method of mean +/- standard error of the

mean. The standard error of the mean can be an appropriate metric when addressing population-wide differences, but it does not convey the variance of the population.

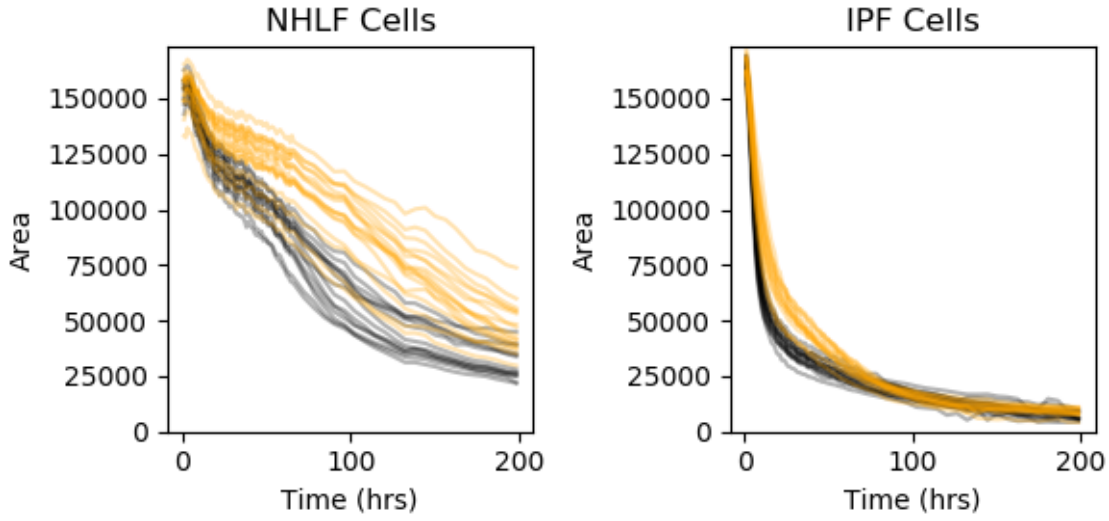

Figure 6.7. Contraction of individual collagen microgels.

6.3.4 Examination of Anti-Fibrotic Drugs

We next assessed the ability of known anti-fibrotic drugs to inhibit contraction of collagen microgels. Using a concentration range of 32 nM to 500 μM, we assessed the dynamic contraction of collagen microgels with NHLF and IPF cells, both with and without 10 ng/mL TGF-β1. Consistent with literature reports (221), Pirfenidone has little effect below 500 μM, but mildly inhibits contraction at 500 μM in all conditions, as in Figure A.6.1. None of the concentrations of Pirfenidone tested produced a half maximal inhibition of contraction (Figure 6.8).

In contrast, Nintedanib exhibits a dose-dependent inhibition of contraction in all conditions (Figure A.6.2). Areas of collagen microgels were normalized to their initial area. Interestingly, the inhibition of microgel contraction was largely independent of TGF-β1 for both NHLF and IPF. After a rapid initial contraction, the area reduction dramatically slowed after ~1 day in culture for both cell types. Recent reports indicate that Nintedanib acts

through multiple mechanisms, including inhibition of early TGF-β1 signaling, inhibition of extracellular matrix production, and induction of autophagy (223). Nintedanib demonstrated greater potency on the stimulated NHLF (IC50 = 10 μM), compared to unstimulated IPF (IC50 = 90 μM). This is consistent with Nintedanib's known mechanism of action as a pan-kinase inhibitor (223). Furthermore, Nintedanib is known to only slow the progression of IPF, rather than restoring function. IPF cells, many of which are already activated into myofibroblasts, are not contracting in response to the same signaling pathway as NHLF, which is also consistent with a lower efficacy of Nintedanib for these cells.

Lastly, the focal adhesion kinase (FAK) inhibitor, PF 431396, inhibited contraction at concentrations above 4 μM for all cell types, as shown in Figure A.6.3. Although FAK inhibition is not a widely used drug target, due to many off-target effects, this experiment does corroborate previous reports indicating that NHLF contraction of collagen gels requires FAK stimulation. Unlike Nintedanib, the FAK inhibitor displayed a similar efficacy for inhibiting contraction of IPF cells (IC50 = 10 μM) compared to NHLF (IC50 = 9 μM). These results are consistent with the need for mechanical stimulation via FAK signaling to achieve myofibroblast activation (201, 202).

These are, to our knowledge, the first reports of dose response for inhibition of TGF-β1 stimulated collagen gel contraction of primary human fibroblasts by Pirfenidone, Nintedanib, and PF 431396.

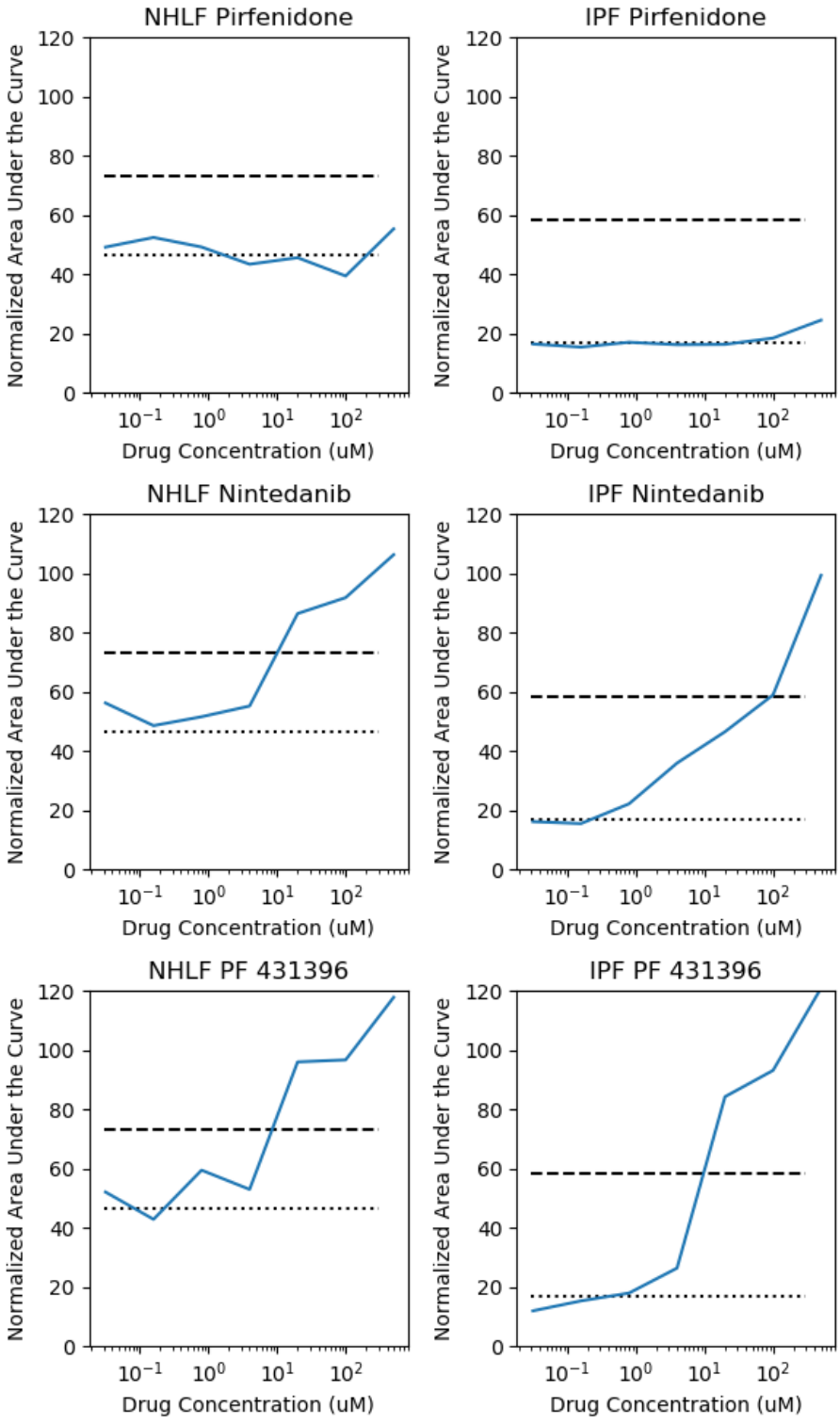

Figure 6.8. Dose response curves for fibrosis inhibitors on TGF-β1 (10 ng/mL) activated NHLF (left side) and untreated IPF collagen microgels. The normalized area under the curve is plotted against the drug concentration in μM for each drug in solid blue lines. The corresponding control is plotted in the black dotted line. The halfway point between the control and 100% (no contraction) is plotted in the dashed lines.

6.4 Conclusions and Future Directions

We have extended the ATPS microgel contraction assay with live-cell imaging to uncover differential phenotypic behavior. We developed and validated liquid handling protocols to avoid introduction of bubbles and to remove PEG from the microgels. DEX, however, remains in the microgels. We assessed and optimized an automated image segmentation algorithm using WEKA machine learning to measure the area of each collagen gel with high temporal resolution. Characterization of the assay revealed that it is inappropriate for high-throughput screening, due to its low Z Factor. However, the assay still provides added convenience and throughput, making it appropriate for secondary screening assays and dose response studies. Lastly, we report dose response characteristics for two FDA approved drugs: Nintedanib, Pirfenidone, as well as the FAK inhibitor, PF 431396 with TGF-activated normal and non-activated IPF primary human fibroblasts. These results confirm previous reports of lower potency for Pirfenidone relative to Nintedanib. This assay could provide useful medium-throughput, phenotypic information to aid secondary and tertiary drug screens, as well as relatively high-throughput information about primary cell behavior in basic research on fibroblast contraction.

CHAPTER 7: Conclusions and Future Outlooks

In this thesis work, I examined applications of ATPS for two microassays: ELISA and the collagen microgel contraction assay. To uncover internal micro-convection, I designed and built a stigmatic microscope to track 3D micro-scale flow. This microscope required optical modeling to determine parameters such as lens strength and ideal placement of components. Following construction of the microscope, I wrote software to calibrate and retrieve Z-positions based on the shapes of microbead images.

Future work using the stigmatic microscope could follow three primary routes. First, improvements to the microscope and software could include the addition of motorized focus and stage movement that are standard in many microscopes. The frame rate of the stigmatic microscope, as currently constructed, is also a limitation. Fine tuning the match between the bead tracer fluorophore and the filter cube set could increase signal, enabling higher temporal resolution. Furthermore, deep learning may improve the fidelity of the calibration, as well as processing speed. Secondly, there are further questions to be answered regarding the drivers of internal micro-scale convection. Comparison of flow tracking data to computational modeling could test the influence of Korteweg Forces that are assumed to drive flow. Thirdly, there are many alternate applications where micro-scale flow is useful. Z-directional flows in microfluidic devices have proven difficult to measure and currently require complicated microfabrication strategies. Stigmatic microscopy could address some of these problems, as it only requires one viewing angle.

I aided in the development of a pre-dried multiplex ATPS ELISA, showing that micro-scale confinement of reagents is robust to dehydration and rehydration. This enables automation of the microarray generation, unlocking the ATPS ELISA as a useful multiplex immunoassay. Combining the pre-dried ATPS ELISA with my findings from the

stigmatic microscope, I led a group to determine optimal parameters for the ATPS ELISA, improving the limit of detection, while also decreasing assay time and steps.

Future work with the ATPS ELISA could examine other phase-forming combinations, besides PEG and DEX. These include PEG-salt systems, polyvinyl alcohol, and Ficoll. Additionally, the ATPS microarray assay could be combined with bead-based detection applications to separate known cross-reacting pairs, while drastically increasing the number of targets that can be detected. Pre-dried ATPS may also prove useful in cell migration assays, as an alternative to scratch-wound assays.

In a separate branch of studies, I determined the performance characteristics of an ATPS collagen micro-gel contraction assay. In that process, I automated most of the production and maintenance of the micro-gels, as well as the image analysis. This facilitated the use of high temporal resolution. Furthermore, this collagen microgel contraction assay enabled drug dose response studies, wherein I confirmed that Nintedanib has higher potency than Pirfenidone.

Future work using the collagen microgel contraction assay could explore additional properties of the collagen microgels. In particular, mechanical tension and collagen fiber alignment are known to influence fibroblast behavior. Further characterization of the mechanical properties could reveal insights into drug mechanisms or key differences between normal and IPF fibroblasts. Additionally, internal convection of ATPS collagen microgels could generate collagen fiber alignment, with potential applications in cancer migration. The automated collagen microgel assay is also amenable to long-term studies of sequential collagen gel contraction. Fibrosis is known to be an aging-related disease. In this proposed assay, cells have the opportunity to activate and differentiate into myofibroblasts, then act upon a fresh layer of collagen gel. Unlike mice, which are prohibitively expensive at long time points, this assay would enable testing of large

libraries of compounds that may influence aging-related fibrotic behavior. Finally, the collagen gel contraction assay currently contains only fibroblasts. Co-culture with epithelial cells presents an interesting suite of questions regarding tissue-level behavior.

APPENDIX A

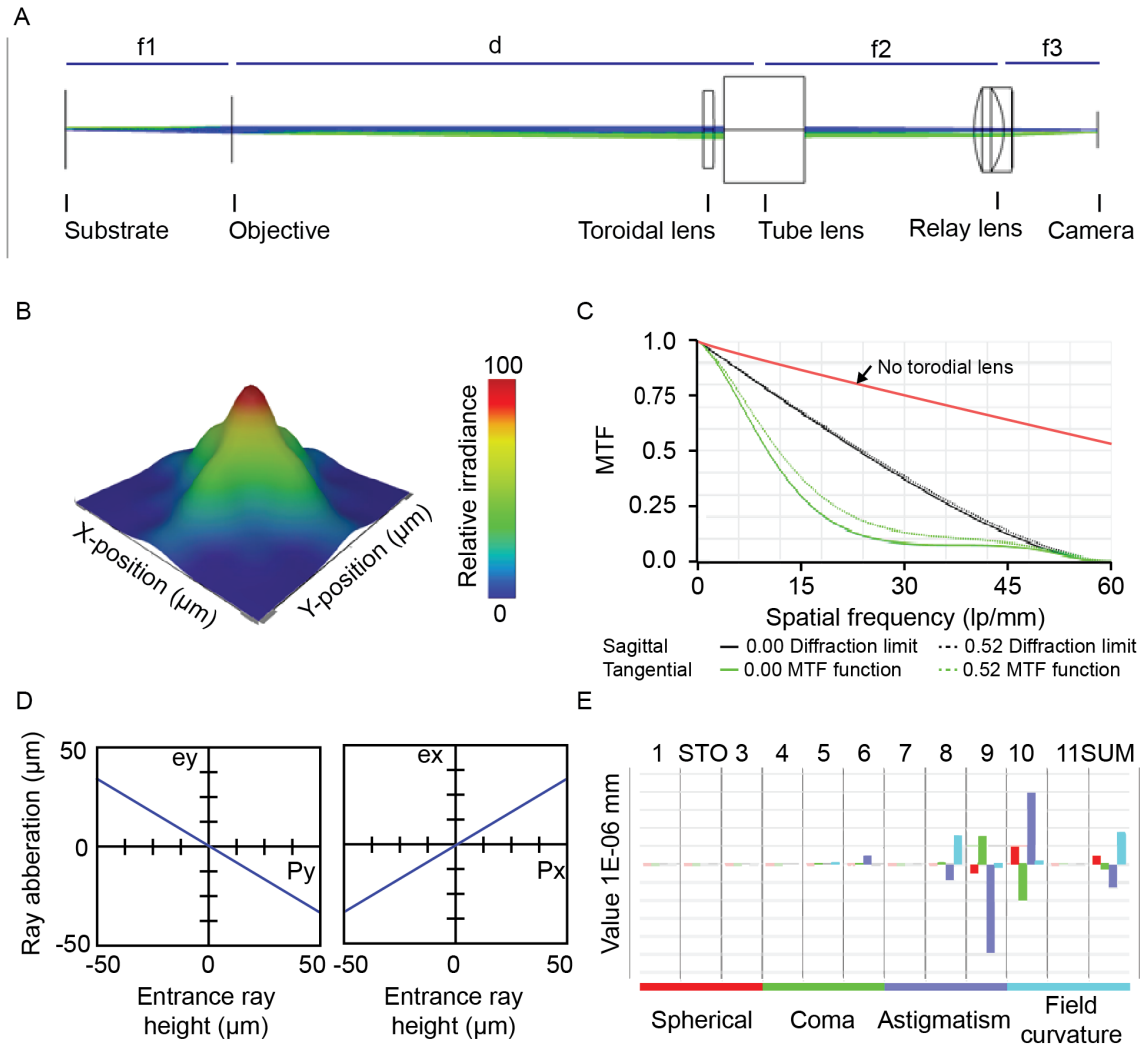

Figure A.1.4. Model of stigmatic microscope. (A) Schematic. (B) Point-spread function (PSF). (C) Modulation transfer function with and without the toroidal lens. (D) Aberration ray fan plot showing astigmatism. (E) Aberration contribution from each surface in the microscope and a sum of the aberrations at the end.

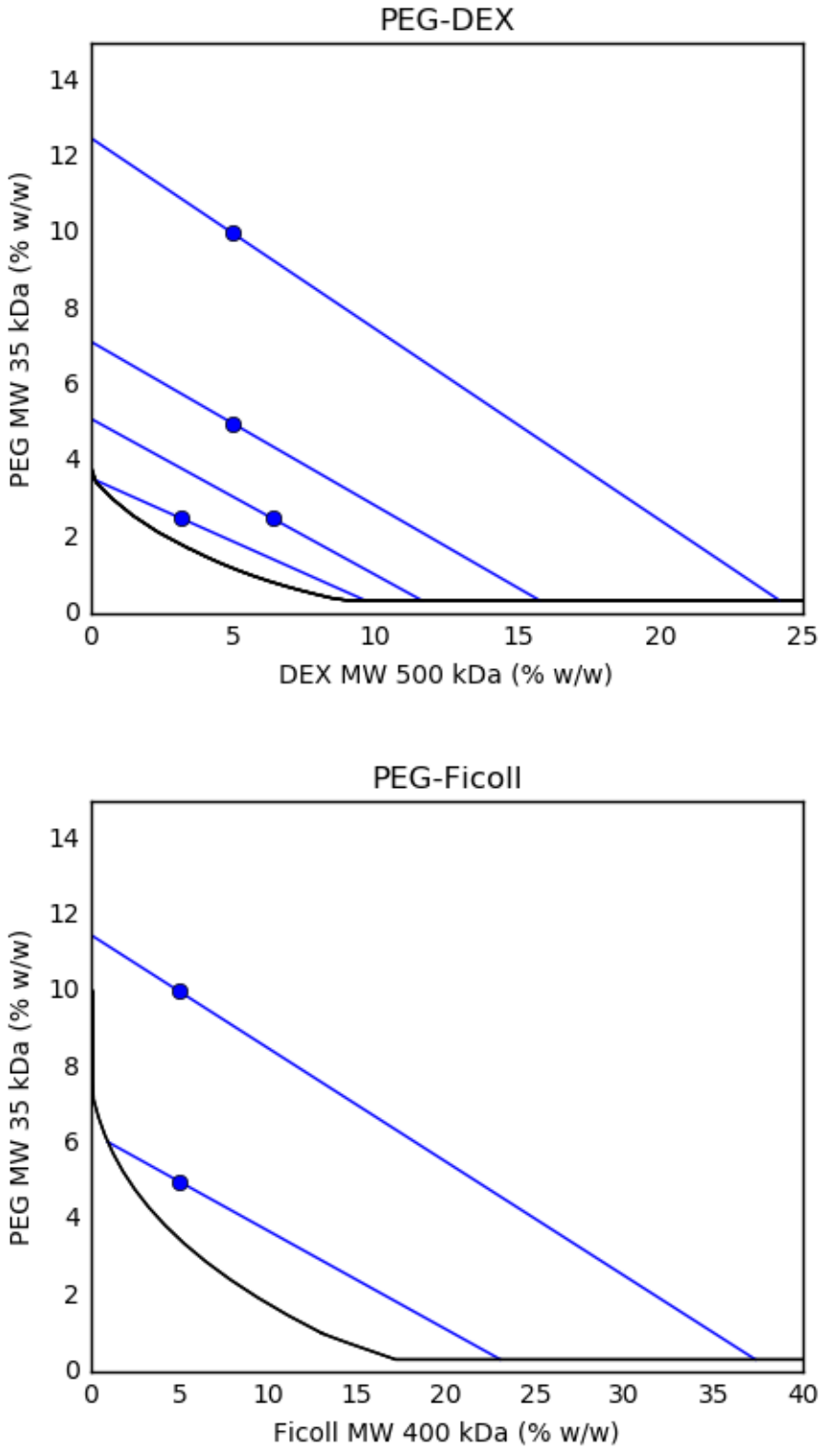

Figure A.1.2. Phase diagrams for PEG-DEX and PEG-Ficoll systems. Circles indicate solutions used to fit tie-lines to the binodal curves based on measured volume ratios.

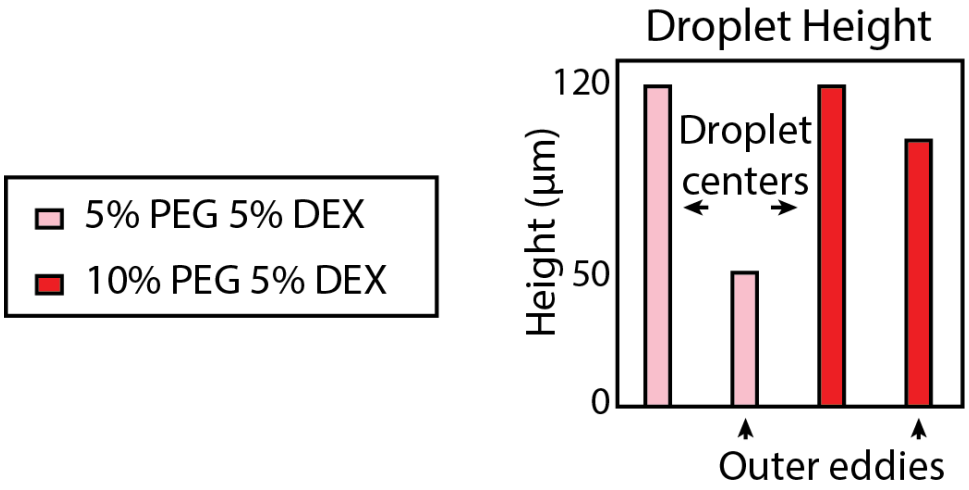

Figure A.1.3. Vertical magnitude of flow traces within the 15-minute rehydration of 1 μL DEX droplets with 100 μL of PEG solutions.

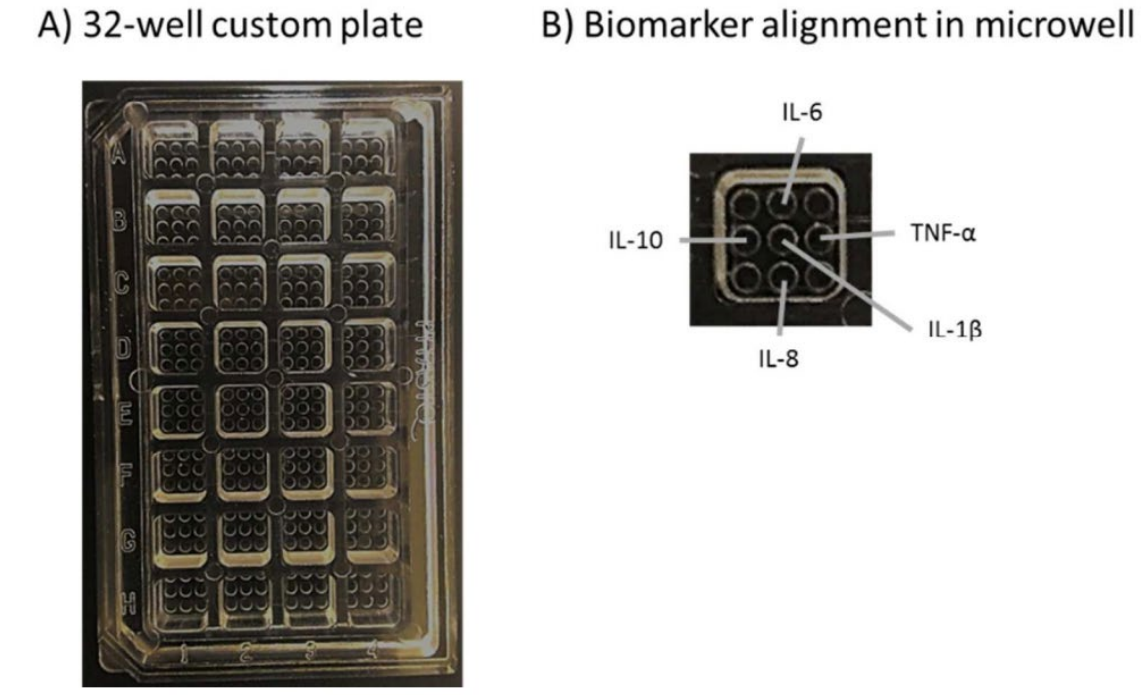

Figure 3.1. (A) Custom-made 32-well polystyrene plate. Each well contains a 3x3 array of microbasins for droplet placement. (B) Alignment of the five biomarkers in each well was consistent across the plate and between different runs for the multiplex ATPS ELISA.

Table A.3.1. Summary of dAb and high protein standard concentrations used in cAbtitration experiments. dAb was pre-spotted as the final layer before dehydration in theATPS multiplex ELISA. High protein standards were prepared in sample diluent andincubated for 4 hours in duplicate for each cAb concentration.

Sample	IL-1β	IL-6	IL-8	IL-10	TNF-α
dAb (ng/mL)	200	50	20	75	400
Protein (pg/mL)	250	600	2000	2000	1000

Table A.3.2. Summary of calculated average concentrations and standard deviations (SD)for five biomarkers in ThP-1 cell culture supernatant with (+LPS) and without (-LPS)stimulation. Analysis performed on pre-spotted ATPS multiplex ELISA with 4 hourincubation of quadruplicates for each sample. Concentrations interpolated in Prism(GraphPad). P-values determined with two-tailed t-test.

Sample	IL-1β	IL-6	IL-8	IL-10	TNF-α
+ LPS	16.75 pg/mL	4.560 pg/mL	969.1 pg/mL	39.83 pg/mL	91.30 pg/mL
	SD=±1.69	SD=±2.95	SD=±156.0	SD=±9.160	SD=±10.68
- LPS	7.210 pg/mL	N/A	100.2 pg/mL	14.42 pg/mL	12.51 pg/mL
	SD=±1.190	N/A	SD=±22.38	SD=±7.410	SD=±15.21
p-value	<0.0001	N/A	<0.0001	0.0050	0.0005

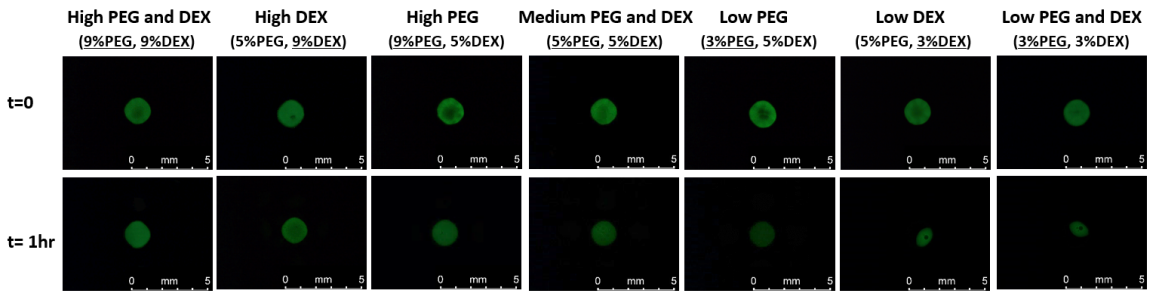

Figure A.4.1 FITC dAb retention studies in different concentrations of PEG and DEX over the course of 1 hour at room temperature.

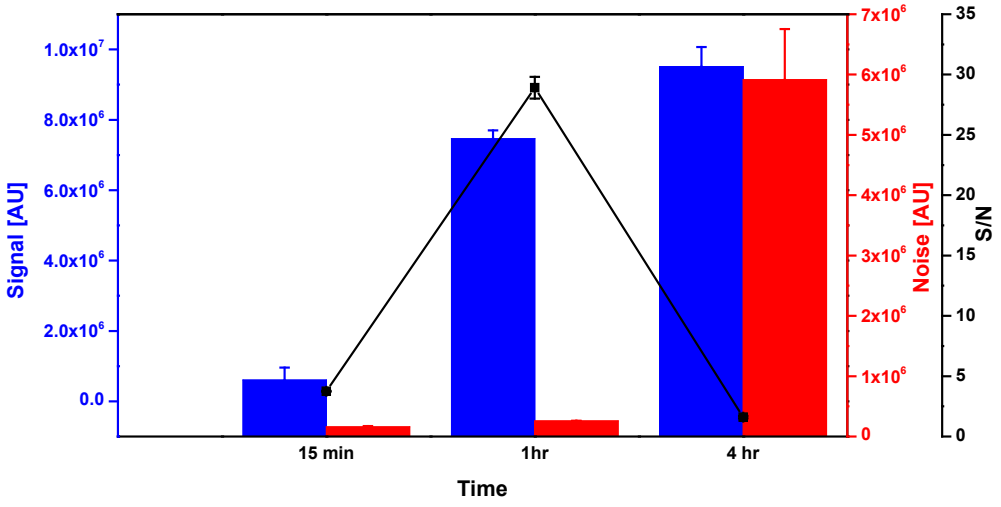

Figure A.4.2. Signal and noise for different incubation time (15 min, 1 hr and 4 hr)

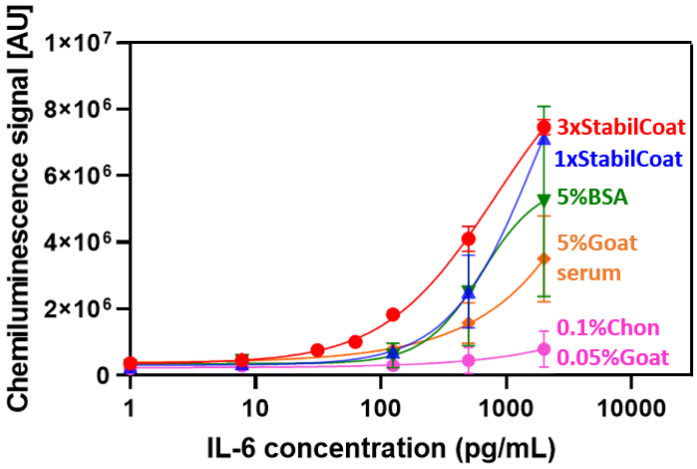

Figure A.4.3. ELISA with different types of blocking buffer

Table A.4.1 Summary of the investigated range and otimum condition for one-incubation ATPS ELISA

Variable	Investigated range	Optimum condition
1. PEG-DEX concentration (%w/w)	3%-5%	5%PEG-5%DEX
2. Incubation time	15 min, 1 hr and 4 hr	1 hr
3. Types of blocking buffer	3xStabilCoat, 1xStabilCoat, 5%BSA, 0.5%Goat serum and 0.1%Chonblock/0.05%goat serum	3xStabilCoat
4. cAb concentration[a] (µg/mL)	2-25	10
5. dAb concentration[b] (ng/mL)	50-400	10 ng/mL for IL-6 25 ng/mL for IL-10, TNF-α, IL-1β and CCL18
6. HRP concentration[c]	1x-15x	5x

[a]cAb: Capture antibody
[b]dAb: Detection antibody
[c]HRP:Horseradish Peroxidase-

Table A.4.2. Literature performance for cytokine detection

Assay	Assay time	Wash steps	Working range (pg/mL)	Plex	LOD (pg/mL)	S/N	Ref.
General ELISA	4 hours 40 min	9	3.91-2,000	1	IL-6 = 9.38 IL-10 = 31.2 TNF-α = 15.6 IL-1β = 3.91 IL-8 = 7.81	IL-6 = 30.1 IL-10 = 15 TNF-α = 10.1 IL-1β = 30.1 IL-8 = 33.2	Commercial R&D ELISA kit
Two-incubation ELISA	4 hours 20 min	12	1-1,200	5	IL-6 = <1.65 IL-10 = 3.40 TNF-α = 1.67 IL-1β = 2.05 IL-8 = 2.72	IL-6 = 30.2 IL-10 = 16.4 TNF-α = 7.6 IL-1β = 64.8 IL-8 = 19.3	(19)
Two-incubation ELISA	15 min	9	31.25-2,000	1	IL-6 > 31.25	-	(134)
Two-incubation ELISA	1 hr	6	1-2,000	5	IL-6 = 28.60 IL-10 = 83.50 TNF-α = 23.01 IL-1β = 60.71 CCL18 = 33.18	IL-6 = 29.7 IL-10 = 3.2 TNF-α = 14.25 IL-1β = 18.6 CCL18 = 25.97	This chapter

Table A.4.2 (continued).

One-incubation ELISA	1 hr	6	1-2,000	5	IL-6 = 1.82 IL-10 = 4.89 TNF-α = 2.41 IL-1β = 7.63 CCL18 = 3.65	IL-6 = 30.3 IL-10 = 10.1 TNF-α = 27.2 IL-1β = 43.06 CCL18 = 43.52	This chapter

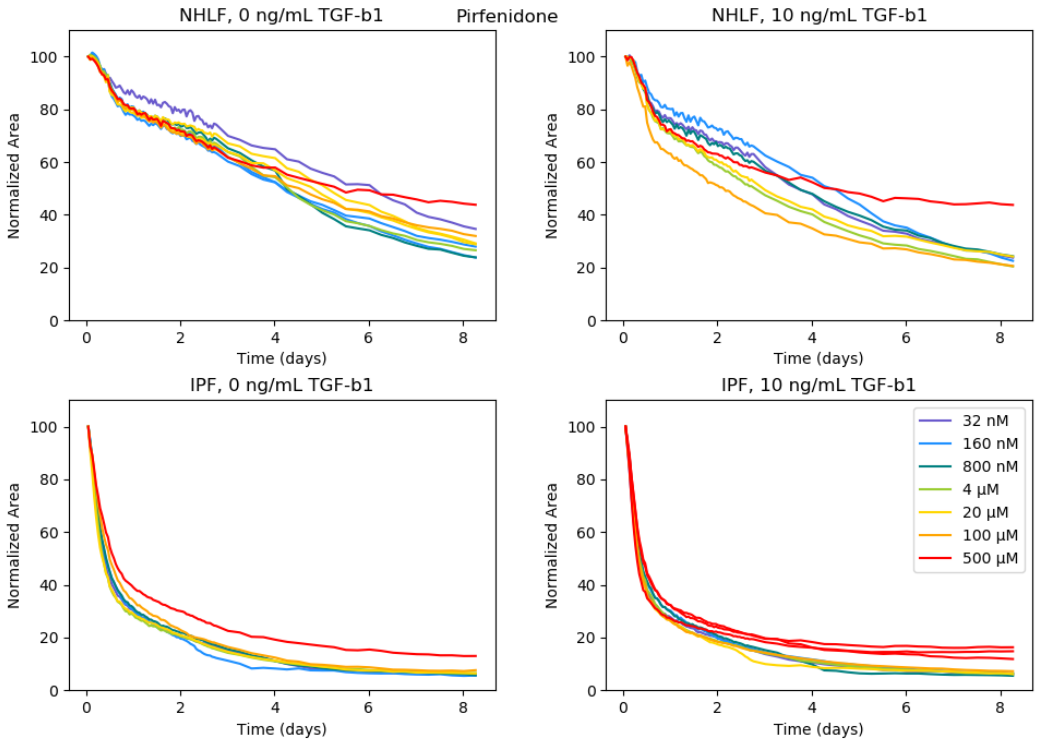

Figure A.6.1. Contraction of primary human fibroblasts with addition of Pirfenidone. Areas are normalized to the initial area of each microgel. N=1-2 per condition.

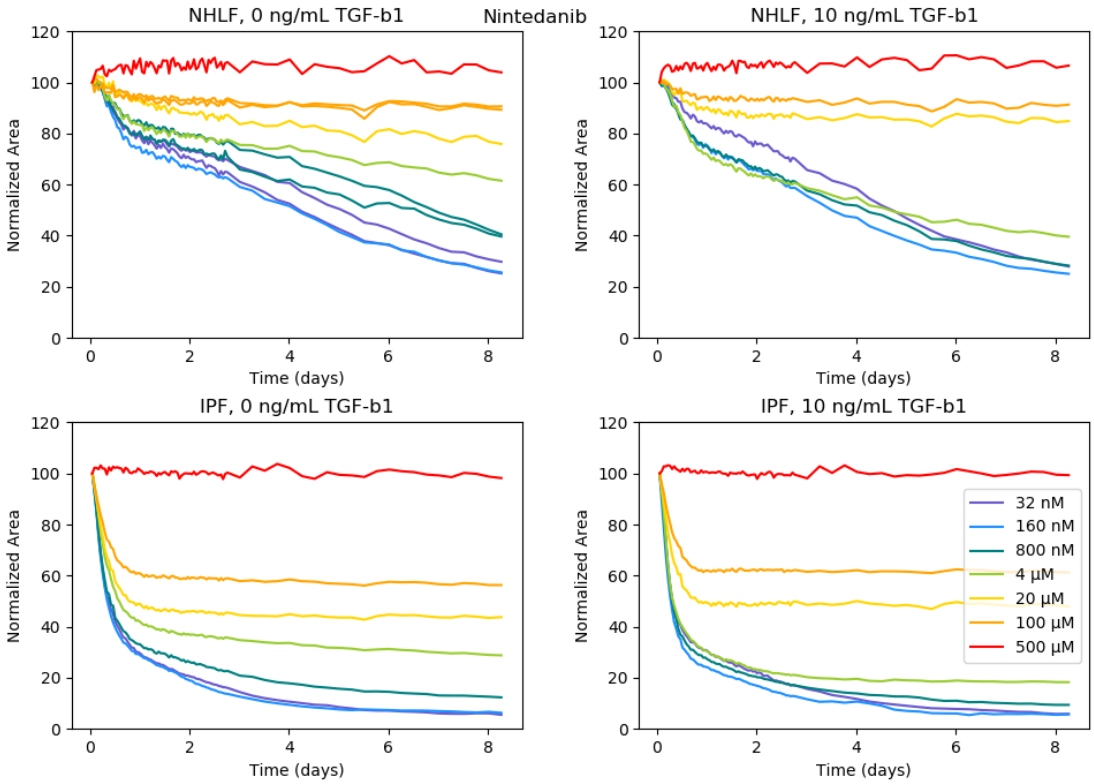

Figure A.6.2. Contraction of collagen microgels by primary human lung fibroblasts with addition of Nintedanib. Areas of collagen microgels were normalized to their initial area. N=1-2 per condition.

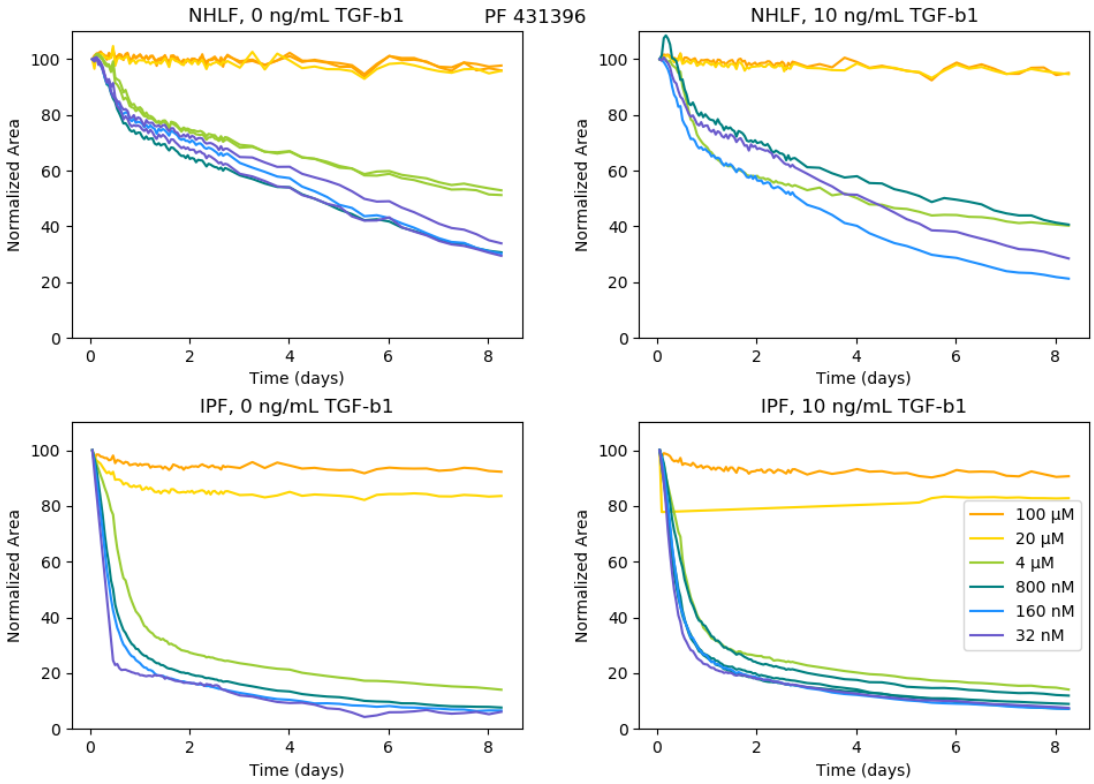

Figure A.6.3. Contraction of collagen microgels with primary human lung fibroblasts and the FAK inhibitor, PF 431396. Areas are normalized to the initial area of each microgel. N=1-2 per condition.

REFERENCES

1. Ishikawa S, Ishimori K, Ito S. A 3D epithelial-mesenchymal co-culture model of human bronchial tissue recapitulates multiple features of airway tissue remodeling by TGF-beta1 treatment. Respir Res. 2017;18(1):195.

2. Moraes C, Labuz JM, Shao Y, Fu J, Takayama S. Supersoft lithography: candy-based fabrication of soft silicone microstructures. Lab on a chip. 2015;15(18):3760-5.

3. Ilagan R, Guthrie K, Quinlan S, Rapoport HS, Jones S, Church A, et al. Linear measurement of cell contraction in a capillary collagen gel system. Biotechniques. 2010;48(2):153-5.

4. Prasad S, Hogaboam CM, Jarai G. Deficient repair response of IPF fibroblasts in a co-culture model of epithelial injury and repair. Fibrogenesis Tissue Repair. 2014;7:7.

5. Miron-Mendoza M, Graham E, Manohar S, Petroll WM. Fibroblast-fibronectin patterning and network formation in 3D fibrin matrices. Matrix Biol. 2017;64:69-80.

6. Wenzel C, Otto S, Prechtl S, Parczyk K, Steigemann P. A novel 3D high-content assay identifies compounds that prevent fibroblast invasion into tissue surrogates. Exp Cell Res. 2015;339(1):35-43.

7. Chen Z, Wang Q, Asmani M, Li Y, Liu C, Li C, et al. Lung Microtissue Array to Screen the Fibrogenic Potential of Carbon Nanotubes. Scientific reports. 2016;6:31304.

8. Vernon RB, Gooden MD. An improved method for the collagen gel contraction assay. In Vitro Cell Dev Biol Anim. 2002;38(2):97-101.

9. Moraes C, Simon AB, Putnam AJ, Takayama S. Aqueous two-phase printing of cell-containing contractile collagen microgels. Biomaterials. 2013;34(37):9623-31.

10. Albertsson PA. Partition of cell particles and macromolecules in polymer two-phase systems. Adv Protein Chem. 1970;24:309-41.

11. Kaul A. The Phase Diagram. In: Hatti-Kaul R, editor. Aqueous Two-Phase Systems: Methods and Protocols: Methods and Protocols. Totowa, NJ: Humana Press; 2000. p. 11-21.

12. Rito-Palomares M. Practical application of aqueous two-phase partition to process development for the recovery of biological products. Journal of chromatography B, Analytical technologies in the biomedical and life sciences. 2004;807(1):3-11.

13. Iqbal M, Tao Y, Xie S, Zhu Y, Chen D, Wang X, et al. Aqueous two-phase system (ATPS): an overview and advances in its applications. Biol Proced Online. 2016;18:18.

14. Tavana H, Jovic A, Mosadegh B, Lee QY, Liu X, Luker KE, et al. Nanolitre liquid patterning in aqueous environments for spatially defined reagent delivery to mammalian cells. Nature materials. 2009;8(9):736-41.

15. Yaguchi T, Lee S, Choi WS, Kim D, Kim T, Mitchell RJ, et al. Micropatterning bacterial suspensions using aqueous two phase systems. The Analyst. 2010;135(11):2848-52.

16. Byun CK, Hwang H, Choi WS, Yaguchi T, Park J, Kim D, et al. Productive chemical interaction between a bacterial microcolony couple is enhanced by periodic relocation. Journal of the American Chemical Society. 2013;135(6):2242-7.

17. Frampton JP, Tsuei M, White JB, Abraham AT, Takayama S. Aqueous Two-Phase System-Mediated Antibody Micropatterning Enables Multiplexed Immunostaining of Cell Monolayers and Tissues. Biotechnology journal. 2014.

18. Frampton JP, White JB, Simon AB, Tsuei M, Paczesny S, Takayama S. Aqueous two-phase system patterning of detection antibody solutions for cross-reaction-free multiplex ELISA. Scientific reports. 2014;4:4878.

19. Eiden L, Yamanishi C, Takayama S, Dishinger JF. Aqueous Two-Phase System Rehydration of Antibody-Polymer Microarrays Enables Convenient Compartmentalized Multiplex Immunoassays. Anal Chem. 2016;88(23):11328-34.

20. Bathany C, Park J, Cho YK, Takayama S. Dehydrated aqueous two-phase system micro-domains retain their shape upon rehydration to allow patterned reagent delivery to cells. J Mater Chem B. 2013;1(44):6020-6.

21. Lee J, Bathany C, Ahn Y, Takayama S, Jung W. Volumetric monitoring of aqueous two phase system droplets using time-lapse optical coherence tomography. Laser Phys Lett. 2016;13(2).

22. Bansal L, Chakraborty S, Basu S. Confinement-induced alterations in the evaporation dynamics of sessile droplets. Soft Matter. 2017;13(5):969-77.

23. Ban T, Fukuyama T, Makino S, Nawa E, Nagatsu Y. Self-Propelled Vesicles Induced by the Mixing of Two Polymeric Aqueous Solutions through a Vesicle Membrane Far from Equilibrium. Langmuir. 2016;32(11):2574-81.

24. Lai HC, Chew TF, Razak NA. Evaluation of Particle Image Velocimetry Measurement Using Multi-wavelength Illumination. Iop Conf Ser-Mat Sci. 2018;370.

25. Hagsater M. Development of micro-PIV techniques for applications in microfluidic systems: Technical University of Denmark; 2008.

26. Fujimoto JG, Pitris C, Boppart SA, Brezinski ME. Optical coherence tomography: an emerging technology for biomedical imaging and optical biopsy. Neoplasia. 2000;2(1-2):9-25.

27. Moschakis T, Murray BS, Dickinson E. Particle tracking using confocal microscopy to probe the microrheology in a phase-separating emulsion containing nonadsorbing polysaccharide. Langmuir. 2006;22(10):4710-9.

28. Huang B, Wang W, Bates M, Zhuang X. Three-dimensional super-resolution imaging by stochastic optical reconstruction microscopy. Science. 2008;319(5864):810-3.

29. Tavana H, Kaylan K, Bersano-Begey T, Luker KE, Luker GD, Takayama S. Polymeric Aqueous Biphasic System Rehydration Facilitates High Throughput Cell Exclusion Patterning For Cell Migration Studies. Adv Funct Mater. 2011;21(15):2920-6.

30. Seward GH. Optical Design of Microscopes. Bellingham, WA: SPIE; 2010.

31. Geary J. Introduction to lens design: with practical ZEMAX examples. Richmond, VA: Willmann-Bell; 2002.

32. Bradski G, Kaehler A. Learning OpenCV. 1st ed. Cambridge, MA: O'Reilly Media Inc.; 2008.

33. Fornaciari M, Prati A. Very Fast Ellipse Detection for Embedded Vision Applications. 2012 Sixth International Conference on Distributed Smart Cameras (Icdsc). 2012.

34. Kojima T, Takayama S. Microscale Determination of Aqueous Two Phase System Binodals by Droplet Dehydration in Oil. Analytical Chemistry. 2013;85(10):5213-8.

35. Laidlaw I, Steinmetz M. Introduction to Differential Sedimentation. Analytical Ultracentrifugation: Techniques and Methods. 2005:270-90.

36. Binks BP, Horozov TS. Colloidal Particles at Liquid Interfaces: Cambridge University Press; 2006.

37. Mashayekhi F, Le AM, Nafisi PM, Wu BM, Kamei DT. Enhancing the lateral-flow immunoassay for detection of proteins using an aqueous two-phase micellar system. Analytical and bioanalytical chemistry. 2012;404(6-7):2057-66.

38. Lemoine J, Fortin T, Salvador A, Jaffuel A, Charrier JP, Choquet-Kastylevsky G. The current status of clinical proteomics and the use of MRM and MRM(3) for biomarker validation. Expert review of molecular diagnostics. 2012;12(4):333-42.

39. Boja ES, Jortani SA, Ritchie J, Hoofnagle AN, Tezak Z, Mansfield E, et al. The journey to regulation of protein-based multiplex quantitative assays. Clinical chemistry. 2011;57(4):560-7.

40. Diamandis EP. The failure of protein cancer biomarkers to reach the clinic: why, and what can be done to address the problem? BMC medicine. 2012;10:87.

41. Rifai N, Gillette MA, Carr SA. Protein biomarker discovery and validation: the long and uncertain path to clinical utility. Nature biotechnology. 2006;24(8):971-83.

42. Anderson NL. The clinical plasma proteome: a survey of clinical assays for proteins in plasma and serum. Clinical chemistry. 2010;56(2):177-85.

43. Hornbeck P. Enzyme-linked immunosorbent assays. Current protocols in immunology / edited by John E Coligan [et al]. 2001;Chapter 2:Unit 2 1.

44. Li H, Bergeron S, Juncker D. Microarray-to-microarray transfer of reagents by snapping of two chips for cross-reactivity-free multiplex immunoassays. Anal Chem. 2012;84(11):4776-83.

45. Markov DA, Swinney K, Bornhop DJ. Label-free molecular interaction determinations with nanoscale interferometry. Journal of the American Chemical Society. 2004;126(50):16659-64.

46. Gordon R, Sinton D, Kavanagh KL, Brolo AG. A new generation of sensors based on extraordinary optical transmission. Accounts of chemical research. 2008;41(8):1049-57.

47. Washburn AL, Luchansky MS, Bowman AL, Bailey RC. Quantitative, label-free detection of five protein biomarkers using multiplexed arrays of silicon photonic microring resonators. Anal Chem. 2010;82(1):69-72.

48. Ji J, O'Connell JG, Carter DJ, Larson DN. High-throughput nanohole array based system to monitor multiple binding events in real time. Anal Chem. 2008;80(7):2491-8.

49. Zheng G, Patolsky F, Cui Y, Wang WU, Lieber CM. Multiplexed electrical detection of cancer markers with nanowire sensor arrays. Nature biotechnology. 2005;23(10):1294-301.

50. Wang ZH, Jin G. A label-free multisensing immunosensor based on imaging ellipsometry. Anal Chem. 2003;75(22):6119-23.

51. Wang ZH, Meng YH, Ying PQ, Qi C, Jin G. A label-free protein microfluidic array for parallel immunoassays. Electrophoresis. 2006;27(20):4078-85.

52. Xue C-Y, Khan SA, Yang K-L. Exploring Optical Properties of Liquid Crystals for Developing Label-Free and High-Throughput Microfluidic Immunoassays. Advanced Materials. 2009;21(2):198-202.

53. Michael KE, Vernekar VN, Keselowsky BG, Meredith JC, Latour RA, Garcia AJ. Adsorption-induced conformational changes in fibronectin due to interactions with well-defined surface chemistries. Langmuir. 2003;19(19):8033-40.

54. Armstrong JK, Wenby RB, Meiselman HJ, Fisher TC. The hydrodynamic radii of macromolecules and their effect on red blood cell aggregation. Biophysical journal. 2004;87(6):4259-70.

55. Diercks AH, Ozinsky A, Hansen CL, Spotts JM, Rodriguez DJ, Aderem A. A microfluidic device for multiplexed protein detection in nano-liter volumes. Analytical biochemistry. 2009;386(1):30-5.

56. Park J, Sunkara V, Kim TH, Hwang H, Cho YK. Lab-on-a-disc for fully integrated multiplex immunoassays. Anal Chem. 2012;84(5):2133-40.

57. Tenje M, Xia H, Evander M, Hammarstrom B, Tojo A, Belak S, et al. Acoustic trapping as a generic non-contact incubation site for multiplex bead-based assays. Analytica chimica acta. 2015;853:682-8.

58. Ng AH, Uddayasankar U, Wheeler AR. Immunoassays in microfluidic systems. Analytical and bioanalytical chemistry. 2010;397(3):991-1007.

59. Qiao Y, Tang H, Munske GR, Dutta P, Ivory CF, Dong WJ. Enhanced fluorescence anisotropy assay for human cardiac troponin I and T detection. Journal of fluorescence. 2011;21(6):2101-10.

60. Pakkila H, Malmi E, Lahtinen S, Soukka T. Rapid homogeneous immunoassay for cardiac troponin I using switchable lanthanide luminescence. Biosensors & bioelectronics. 2014;62:201-7.

61. Schallmeiner E, Oksanen E, Ericsson O, Spangberg L, Eriksson S, Stenman UH, et al. Sensitive protein detection via triple-binder proximity ligation assays. Nature methods. 2007;4(2):135-7.

62. Assarsson E LM, Holmquist G, Bjo¨rkesten J, Bucht Thorsen S, et al. . Homogenous 96-Plex PEA Immunoassay Exhibiting High Sensitivity, Specificity, and Excellent Scalability. PLoS ONE. 2014;9(4):e95192.

63. Shaw LM, Vanderstichele H, Knapik-Czajka M, Figurski M, Coart E, Blennow K, et al. Qualification of the analytical and clinical performance of CSF biomarker analyses in ADNI. Acta neuropathologica. 2011;121(5):597-609.

64. Schwenzer KS, Anhalt JP. Automated fluorescence polarization immunoassay for monitoring streptomycin. Antimicrobial agents and chemotherapy. 1983;23(5):683-7.

65. Filburn BH, Shull VH, Tempera YM, Dick JD. Evaluation of an automated fluorescence polarization immunoassay for vancomycin. Antimicrobial agents and chemotherapy. 1983;24(2):216-20.

66. Smith DS, Eremin SA. Fluorescence polarization immunoassays and related methods for simple, high-throughput screening of small molecules. Analytical and bioanalytical chemistry. 2008;391(5):1499-507.

67. Tian J, Zhou L, Zhao Y, Wang Y, Peng Y, Zhao S. Multiplexed detection of tumor markers with multicolor quantum dots based on fluorescence polarization immunoassay. Talanta. 2012;92:72-7.

68. Lam AJ, St-Pierre F, Gong Y, Marshall JD, Cranfill PJ, Baird MA, et al. Improving FRET dynamic range with bright green and red fluorescent proteins. Nature methods. 2012;9(10):1005-12.

69. Hussain SA. An Introduction to Fluorescence Resonance Energy Transfer (FRET)2009. Available from: arXiv:0908.1815.

70. Zeng Q, Zhang Y, Liu X, Tu L, Kong X, Zhang H. Multiple homogeneous immunoassays based on a quantum dots-gold nanorods FRET nanoplatform. Chemical communications. 2012;48(12):1781-3.

71. Liu M, Zhao H, Quan X, Chen S, Fan X. Distance-independent quenching of quantum dots by nanoscale-graphene in self-assembled sandwich immunoassay. Chemical communications. 2010;46(42):7909-11.

72. Ullman EF, Kirakossian H, Switchenko AC, Ishkanian J, Ericson M, Wartchow CA, et al. Luminescent oxygen channeling assay (LOCI): sensitive, broadly applicable homogeneous immunoassay method. Clinical chemistry. 1996;42(9):1518-26.

73. Leister KP, Huang R, Goodwin BL, Chen A, Austin CP, Xia M. Two High Throughput Screen Assays for Measurement of TNF-alpha in THP-1 Cells. Current chemical genomics. 2011;5:21-9.

74. Simon AB, Frampton JP, Huang NT, Kurabayashi K, Paczesny S, Takayama S. Aqueous two-phase systems enable multiplexing of homogeneous immunoassays. Technology. 2014;2(2):176.

75. Fredriksson S, Gullberg M, Jarvius J, Olsson C, Pietras K, Gustafsdottir SM, et al. Protein detection using proximity-dependent DNA ligation assays. Nature biotechnology. 2002;20(5):473-7.

76. Fredriksson S, Dixon W, Ji H, Koong AC, Mindrinos M, Davis RW. Multiplexed protein detection by proximity ligation for cancer biomarker validation. Nature methods. 2007;4(4):327-9.

77. Darmanis S, Nong RY, Hammond M, Gu J, Alderborn A, Vanelid J, et al. Sensitive plasma protein analysis by microparticle-based proximity ligation assays. Molecular & cellular proteomics : MCP. 2010;9(2):327-35.

78. Ellington AA, Kullo IJ, Bailey KR, Klee GG. Antibody-based protein multiplex platforms: technical and operational challenges. Clinical chemistry. 2010;56(2):186-93.

79. Poetz O, Ostendorp R, Brocks B, Schwenk JM, Stoll D, Joos TO, et al. Protein microarrays for antibody profiling: specificity and affinity determination on a chip. Proteomics. 2005;5(9):2402-11.

80. Lipman NS, Jackson LR, Trudel LJ, Weis-Garcia F. Monoclonal versus polyclonal antibodies: distinguishing characteristics, applications, and information resources. ILAR journal / National Research Council, Institute of Laboratory Animal Resources. 2005;46(3):258-68.

81. Schwenk JM, Lindberg J, Sundberg M, Uhlen M, Nilsson P. Determination of binding specificities in highly multiplexed bead-based assays for antibody proteomics. Molecular & cellular proteomics : MCP. 2007;6(1):125-32.

82. Kim JW, You J. Protein target quantification decision tree. International journal of proteomics. 2013;2013:701247.

83. Tighe P, Negm O, Todd I, Fairclough L. Utility, reliability and reproducibility of immunoassay multiplex kits. Methods. 2013;61(1):23-9.

84. Li D, Chiu H, Gupta V, Chan DW. Validation of a multiplex immunoassay for serum angiogenic factors as biomarkers for aggressive prostate cancer. Clin Chim Acta. 2012;413(19-20):1506-11.

85. Wood WG. "Matrix effects" in immunoassays. Scandinavian journal of clinical and laboratory investigation Supplementum. 1991;205:105-12.

86. Mire-Sluis AR, Barrett YC, Devanarayan V, Koren E, Liu H, Maia M, et al. Recommendations for the design and optimization of immunoassays used in the detection of host antibodies against biotechnology products. J Immunol Methods. 2004;289(1-2):1-16.

87. Shah VP, Midha, K. K., Dighe, S., McGilveray, I. J., Skelly, J. P., Yacobi, A., Layloff, T., Viswanathan, C. T., Cook, C. E., McDowall, R. D., Pittman, K. A. and

Spector, S. Analytical methods validation: Bioavailability, bioequivalence, and pharmacokinetic studies. J Pharm Sci. 1992;81:309-12.

88. Schnaidt M, Weinstock C, Jurisic M, Schmid-Horch B, Ender A, Wernet D. HLA antibody specification using single-antigen beads--a technical solution for the prozone effect. Transplantation. 2011;92(5):510-5.

89. Ermens AAM, Bayens AJM, Crooymans A, Broekman-van Hout AAM, van Duijnhoven HLP. Dilution protocols for detection of hook effects/prozone phenomenon. Clinical chemistry. 2000;46(10):1719-20.

90. Weinstock C, Schnaidt M. The complement-mediated prozone effect in the Luminex single-antigen bead assay and its impact on HLA antibody determination in patient sera. International journal of immunogenetics. 2013;40(3):171-7.

91. Juncker D, Bergeron S, Laforte V, Li H. Cross-reactivity in antibody microarrays and multiplexed sandwich assays: shedding light on the dark side of multiplexing. Current opinion in chemical biology. 2014;18:29-37.

92. Perlee L, Christiansen J, Dondero R, Grimwade B, Lejnine S, Mullenix M, et al. Development and standardization of multiplexed antibody microarrays for use in quantitative proteomics. Proteome science. 2004;2(1):9.

93. Bjerner J, Bormer OP, Nustad K. The war on heterophilic antibody interference. Clinical chemistry. 2005;51(1):9-11.

94. Bolstad N, Warren DJ, Nustad K. Heterophilic antibody interference in immunometric assays. Best practice & research Clinical endocrinology & metabolism. 2013;27(5):647-61.

95. Bjerner J, Nustad K, Norum LF, Olsen KH, Bormer OP. Immunometric assay interference: incidence and prevention. Clinical chemistry. 2002;48(4):613-21.

96. Saviranta P, Okon R, Brinker A, Warashina M, Eppinger J, Geierstanger BH. Evaluating sandwich immunoassays in microarray format in terms of the ambient analyte regime. Clinical chemistry. 2004;50(10):1907-20.

97. Tam SW, Wiese R, Lee S, Gilmore J, Kumble KD. Simultaneous analysis of eight human Th1/Th2 cytokines using microarrays. J Immunol Methods. 2002;261(1-2):157-65.

98. de Jager W, Prakken BJ, Bijlsma JWJ, Kuis W, Rijkers GT. Improved multiplex immunoassay performance in human plasma and synovial fluid following removal of interfering heterophilic antibodies. J Immunol Methods. 2005;300(1-2):124-35.

99. Fulwyler MJ, McHugh TM. Flow microsphere immunoassay for the quantitative and simultaneous detection of multiple soluble analytes. Methods Cell Biol. 1990;33:613-29.

100. Kellar KL, Kalwar RR, Dubois KA, Crouse D, Chafin WD, Kane BE. Multiplexed fluorescent bead-based immunoassays for quantitation of human cytokines in serum and culture supernatants. Cytometry. 2001;45(1):27-36.

101. Wei W, Shin YS, Ma C, Wang J, Elitas M, Fan R, et al. Microchip platforms for multiplex single-cell functional proteomics with applications to immunology and cancer research. Genome Med. 2013;5(8):75.

102. Tighe PJ, Ryder RR, Todd I, Fairclough LC. ELISA in the multiplex era: potentials and pitfalls. Proteomics Clin Appl. 2015;9(3-4):406-22.

103. Huebner A, Sharma S, Srisa-Art M, Hollfelder F, Edel JB, Demello AJ. Microdroplets: a sea of applications? Lab on a chip. 2008;8(8):1244-54.

104. Du W, Li L, Nichols KP, Ismagilov RF. SlipChip. Lab on a chip. 2009;9(16):2286-92.

105. Pla-Roca M, Leulmi RF, Tourekhanova S, Bergeron S, Laforte V, Moreau E, et al. Antibody colocalization microarray: a scalable technology for multiplex protein analysis in complex samples. Molecular & cellular proteomics : MCP. 2012;11(4):M111 011460.

106. Andersson P, Jesson G, Kylberg G, Ekstrand G, Thorsen G. Parallel nanoliter microfluidic analysis system. Anal Chem. 2007;79(11):4022-30.

107. Aldo P, Marusov G, Svancara D, David J, Mor G. Simple Plex() : A Novel Multi-Analyte, Automated Microfluidic Immunoassay Platform for the Detection of Human and Mouse Cytokines and Chemokines. Am J Reprod Immunol. 2016;75(6):678-93.

108. Albertsson PA. Partition methods for fractionation of cell particles and macromolecules. Methods Biochem Anal. 1962;10:229-62.

109. Grilo AL, Aires-Barros MR, Azevedo AM. Partitioning in Aqueous Two-Phase Systems: Fundamentals, Applications and Trends. Sep Purif Rev. 2016;45(1):68-80.

110. Lund ME, To J, O'Brien BA, Donnelly S. The choice of phorbol 12-myristate 13-acetate differentiation protocol influences the response of THP-1 macrophages to a pro-inflammatory stimulus. J Immunol Methods. 2016;430:64-70.

111. Chanput W, Mes J, Vreeburg RAM, Sayelkoul HFJ, Wichers HJ. Transcription profiles of LPS-stimulated THP-1 monocytes and macrophages: a tool to study inflammation modulating effects of food-derived compounds. Food Funct. 2010;1(3):254-61.

112. Armbruster DA, Pry T. Limit of blank, limit of detection and limit of quantitation. Clin Biochem Rev. 2008;29 Suppl 1:S49-52.

113. Jeong SH. Analytical methods and formulation factors to enhance protein stability in solution. Arch Pharm Res. 2012;35(11):1871-86.

114. Gekko K, Morikawa T. Thermodynamics of Polyol-Induced Thermal Stabilization of Chymotrypsinogen. J Biochem-Tokyo. 1981;90(1):51-60.

115. Gonzalez M, Murature DA, Fidelio GD. Thermal-Stability of Human-Immunoglobulins with Sorbitol - a Critical-Evaluation. Vox Sang. 1995;68(1):1-4.

116. Akdis M, Burgler S, Crameri R, Eiwegger T, Fujita H, Gomez E, et al. Interleukins, from 1 to 37, and interferon-gamma: receptors, functions, and roles in diseases. The Journal of allergy and clinical immunology. 2011;127(3):701-21 e1-70.

117. Tartour E, Fridman WH. Cytokines and cancer. Int Rev Immunol. 1998;16(5-6):683-704.

118. Duque GA, Descoteaux A. Macrophage cytokines: involvement in immunity and infectious diseases. Front Immunol. 2014;5:1-12.

119. Baliwag J, Barnes DH, Johnston A. Cytokines in psoriasis. Cytokine. 2015;73(2):342-50.

120. Daigneault M, Preston JA, Marriott HM, Whyte MKB, Dockrell DH. The Identification of Markers of Macrophage Differentiation in PMA-Stimulated THP-1 Cells and Monocyte-Derived Macrophages. Plos One. 2010;5(1).

121. Vashist SK, Schneider EM, Lam E, Hrapovic S, Luong JHT. One-step antibody immobilization-based rapid and highly-sensitive sandwich ELISA procedure for potential in vitro diagnostics. Scientific reports. 2014;4.

122. Bari SMI, Reis LG, Nestorova GG. Calorimetric sandwich-type immunosensor for quantification of TNF-alpha. Biosensors & bioelectronics. 2019;126:82-7.

123. Lim PY, Cardosa MJ. Development of a sandwich ELISA to detect virus-like-particles in enterovirus A71 vaccines. J Virol Methods. 2019;270:113-9.

124. Ooi KG, Galatowicz G, Calder VL, Lightman SL. Cytokines and chemokines in uveitis: is there a correlation with clinical phenotype? Clin Med Res. 2006;4(4):294-309.

125. Matson RS. Multiplex ELISA Using Oligonucleotide Tethered Antibodies. Methods Mol Biol. 2015;1318:181-95.

126. Tokarz R, Mishra N, Tagliafierro T, Sameroff S, Caciula A, Chauhan L, et al. A multiplex serologic platform for diagnosis of tick-borne diseases. Scientific reports. 2018;8(1):3158.

127. Yamanishi CD, Chiu JH, Takayama S. Systems for multiplexing homogeneous immunoassays. Bioanalysis. 2015;7(12):1545-56.

128. Eddings MA, Miles AR, Eckman JW, Kim J, Rich RL, Gale BK, et al. Improved continuous-flow print head for micro-array deposition. Analytical biochemistry. 2008;382(1):55-9.

129. Weng Z, Zhao Q. Utilizing ELISA to monitor protein-protein interaction. Methods Mol Biol. 2015;1278:341-52.

130. Syedbasha M, Linnik J, Santer D, O'Shea D, Barakat K, Joyce M, et al. An ELISA Based Binding and Competition Method to Rapidly Determine Ligand-receptor Interactions. J Vis Exp. 2016(109).

131. Lin M, Krawitz D, Callahan MD, Deperalta G, Wecksler AT. Characterization of ELISA Antibody-Antigen Interaction using Footprinting-Mass Spectrometry and Negative Staining Transmission Electron Microscopy. J Am Soc Mass Spectrom. 2018;29(5):961-71.

132. Yamanishi C, Oliver CR, Kojima T, Takayama S. Stigmatic Microscopy Enables Low-Cost, 3D, Microscale Particle Imaging Velocimetry in Rehydrating Aqueous Two-Phase Systems. Front Chem. 2019;7:311.

133. Xia T, Xu X, Zhao N, Luo Z, Tang Y. Comparison of the diagnostic power of cytokine patterns and procalcitonin for predicting infection among paediatric haematology/oncology patients. Clin Microbiol Infect. 2016;22(12):996-1001.

134. Yamanishi C, Robinson S, Takayama S. Biofabrication of phenotypic pulmonary fibrosis assays. Biofabrication. 2019;11(3):032005.

135. Spiller KL, Wrona EA, Romero-Torres S, Pallotta I, Graney PL, Witherel CE, et al. Differential gene expression in human, murine, and cell line-derived macrophages upon polarization. Exp Cell Res. 2016;347(1):1-13.

136. Crowe JH, Carpenter JF, Crowe LM. The role of vitrification in anhydrobiosis. Annual review of physiology. 1998;60:73-103.

137. Peterfi Z, Kocsis B. Comparison of blocking agents for an ELISA for LPS. J Immunoassay. 2000;21(4):341-54.

138. Genin M, Clement F, Fattaccioli A, Raes M, Michiels C. M1 and M2 macrophages derived from THP-1 cells differentially modulate the response of cancer cells to etoposide. BMC Cancer. 2015;15:577.

139. King TE, Jr., Pardo A, Selman M. Idiopathic pulmonary fibrosis. Lancet. 2011;378(9807):1949-61.

140. Ahluwalia N, Shea BS, Tager AM. New therapeutic targets in idiopathic pulmonary fibrosis. Aiming to rein in runaway wound-healing responses. American journal of respiratory and critical care medicine. 2014;190(8):867-78.

141. Selman M, Pardo A. Revealing the pathogenic and aging-related mechanisms of the enigmatic idiopathic pulmonary fibrosis. an integral model. American journal of respiratory and critical care medicine. 2014;189(10):1161-72.

142. Betensley A, Sharif R, Karamichos D. A Systematic Review of the Role of Dysfunctional Wound Healing in the Pathogenesis and Treatment of Idiopathic Pulmonary Fibrosis. J Clin Med. 2016;6(1).

143. Waters DW, Blokland KEC, Pathinayake PS, Burgess JK, Mutsaers SE, Prele CM, et al. Fibroblast senescence in the pathology of idiopathic pulmonary fibrosis. Am J Physiol Lung Cell Mol Physiol. 2018;315(2):L162-L72.

144. Selman M, King TE, Pardo A, American Thoracic S, European Respiratory S, American College of Chest P. Idiopathic pulmonary fibrosis: prevailing and evolving hypotheses about its pathogenesis and implications for therapy. Ann Intern Med. 2001;134(2):136-51.

145. Collard HR, Bradford WZ, Cottin V, Flaherty KR, King TE, Jr., Koch GG, et al. A new era in idiopathic pulmonary fibrosis: considerations for future clinical trials. Eur Respir J. 2015;46(1):243-9.

146. Moeller A, Ask K, Warburton D, Gauldie J, Kolb M. The bleomycin animal model: a useful tool to investigate treatment options for idiopathic pulmonary fibrosis? The international journal of biochemistry & cell biology. 2008;40(3):362-82.

147. Sundarakrishnan A, Chen Y, Black LD, Aldridge BB, Kaplan DL. Engineered cell and tissue models of pulmonary fibrosis. Adv Drug Deliv Rev. 2018;129:78-94.

148. Eder J, Sedrani R, Wiesmann C. The discovery of first-in-class drugs: origins and evolution. Nat Rev Drug Discov. 2014;13(8):577-87.

149. Wolters PJ, Blackwell TS, Eickelberg O, Loyd JE, Kaminski N, Jenkins G, et al. Time for a change: is idiopathic pulmonary fibrosis still idiopathic and only fibrotic? Lancet Respir Med. 2018;6(2):154-60.

150. Sakai N, Tager AM. Fibrosis of two: Epithelial cell-fibroblast interactions in pulmonary fibrosis. Biochimica et biophysica acta. 2013;1832(7):911-21.

151. Horowitz JC, Thannickal VJ. Epithelial-mesenchymal interactions in pulmonary fibrosis. Semin Respir Crit Care Med. 2006;27(6):600-12.

152. Borensztajn K, Crestani B, Kolb M. Idiopathic pulmonary fibrosis: from epithelial injury to biomarkers--insights from the bench side. Respiration. 2013;86(6):441-52.

153. Tschumperlin DJ, Margulies SS. Equibiaxial deformation-induced injury of alveolar epithelial cells in vitro. The American journal of physiology. 1998;275(6 Pt 1):L1173-83.

154. Douville NJ, Zamankhan P, Tung YC, Li R, Vaughan BL, Tai CF, et al. Combination of fluid and solid mechanical stresses contribute to cell death and detachment in a microfluidic alveolar model. Lab on a chip. 2011;11(4):609-19.

155. Fernandez-Perez ER, Yilmaz M, Jenad H, Daniels CE, Ryu JH, Hubmayr RD, et al. Ventilator settings and outcome of respiratory failure in chronic interstitial lung disease. Chest. 2008;133(5):1113-9.

156. Fumeaux T, Rothmeier C, Jolliet P. Outcome of mechanical ventilation for acute respiratory failure in patients with pulmonary fibrosis. Intensive care medicine. 2001;27(12):1868-74.

157. Snyder-Talkington BN, Schwegler-Berry D, Castranova V, Qian Y, Guo NL. Multi-walled carbon nanotubes induce human microvascular endothelial cellular effects in an alveolar-capillary co-culture with small airway epithelial cells. Part Fibre Toxicol. 2013;10:35.

158. Lin H, Li H, Cho HJ, Bian S, Roh HJ, Lee MK, et al. Air-liquid interface (ALI) culture of human bronchial epithelial cell monolayers as an in vitro model for airway drug transport studies. Journal of pharmaceutical sciences. 2007;96(2):341-50.

159. Lenz AG, Karg E, Lentner B, Dittrich V, Brandenberger C, Rothen-Rutishauser B, et al. A dose-controlled system for air-liquid interface cell exposure and application to zinc oxide nanoparticles. Part Fibre Toxicol. 2009;6:32.

160. Huh D, Matthews BD, Mammoto A, Montoya-Zavala M, Hsin HY, Ingber DE. Reconstituting organ-level lung functions on a chip. Science. 2010;328(5986):1662-8.

161. Elbert KJ, Schafer UF, Schafers HJ, Kim KJ, Lee VH, Lehr CM. Monolayers of human alveolar epithelial cells in primary culture for pulmonary absorption and transport studies. Pharmaceutical research. 1999;16(5):601-8.

162. Srinivasan B, Kolli AR, Esch MB, Abaci HE, Shuler ML, Hickman JJ. TEER measurement techniques for in vitro barrier model systems. J Lab Autom. 2015;20(2):107-26.

163. Liang CC, Park AY, Guan JL. In vitro scratch assay: a convenient and inexpensive method for analysis of cell migration in vitro. Nat Protoc. 2007;2(2):329-33.

164. LeBoeuf RD, Raja RH, Fuller GM, Weigel PH. Human fibrinogen specifically binds hyaluronic acid. The Journal of biological chemistry. 1986;261(27):12586-92.

165. Greiling D, Clark RA. Fibronectin provides a conduit for fibroblast transmigration from collagenous stroma into fibrin clot provisional matrix. Journal of cell science. 1997;110 (Pt 7):861-70.

166. Clark RA, Lin F, Greiling D, An J, Couchman JR. Fibroblast invasive migration into fibronectin/fibrin gels requires a previously uncharacterized dermatan sulfate-CD44 proteoglycan. J Invest Dermatol. 2004;122(2):266-77.

167. Lin F, Ren XD, Doris G, Clark RA. Three-dimensional migration of human adult dermal fibroblasts from collagen lattices into fibrin/fibronectin gels requires syndecan-4 proteoglycan. J Invest Dermatol. 2005;124(5):906-13.

168. Brown LF, Lanir N, McDonagh J, Tognazzi K, Dvorak AM, Dvorak HF. Fibroblast migration in fibrin gel matrices. The American journal of pathology. 1993;142(1):273-83.

169. Svee K, White J, Vaillant P, Jessurun J, Roongta U, Krumwiede M, et al. Acute lung injury fibroblast migration and invasion of a fibrin matrix is mediated by CD44. J Clin Invest. 1996;98(8):1713-27.

170. Lewis KJR, Hall JK, Kiyotake EA, Christensen T, Balasubramaniam V, Anseth KS. Epithelial-mesenchymal crosstalk influences cellular behavior in a 3D alveolus-fibroblast model system. Biomaterials. 2018;155:124-34.

171. Hattori N, Degen JL, Sisson TH, Liu H, Moore BB, Pandrangi RG, et al. Bleomycin-induced pulmonary fibrosis in fibrinogen-null mice. J Clin Invest. 2000;106(11):1341-50.

172. Ploplis VA, Wilberding J, McLennan L, Liang Z, Cornelissen I, DeFord ME, et al. A total fibrinogen deficiency is compatible with the development of pulmonary fibrosis in mice. The American journal of pathology. 2000;157(3):703-8.

173. Thannickal VJ, Toews GB, White ES, Lynch JP, 3rd, Martinez FJ. Mechanisms of pulmonary fibrosis. Annu Rev Med. 2004;55:395-417.

174. Tomasek JJ, Gabbiani G, Hinz B, Chaponnier C, Brown RA. Myofibroblasts and mechano-regulation of connective tissue remodelling. Nat Rev Mol Cell Biol. 2002;3(5):349-63.

175. Leask A, Abraham DJ. TGF-beta signaling and the fibrotic response. FASEB journal : official publication of the Federation of American Societies for Experimental Biology. 2004;18(7):816-27.

176. Desmouliere A, Chaponnier C, Gabbiani G. Tissue repair, contraction, and the myofibroblast. Wound repair and regeneration : official publication of the Wound Healing Society [and] the European Tissue Repair Society. 2005;13(1):7-12.

177. Darby IA, Zakuan N, Billet F, Desmouliere A. The myofibroblast, a key cell in normal and pathological tissue repair. Cellular and molecular life sciences : CMLS. 2016;73(6):1145-57.

178. Tuan TL, Song A, Chang S, Younai S, Nimni ME. In vitro fibroplasia: matrix contraction, cell growth, and collagen production of fibroblasts cultured in fibrin gels. Exp Cell Res. 1996;223(1):127-34.

179. Rice JJ, Martino MM, De Laporte L, Tortelli F, Briquez PS, Hubbell JA. Engineering the regenerative microenvironment with biomaterials. Adv Healthc Mater. 2013;2(1):57-71.

180. Xu X, Jha AK, Harrington DA, Farach-Carson MC, Jia X. Hyaluronic Acid-Based Hydrogels: from a Natural Polysaccharide to Complex Networks. Soft Matter. 2012;8(12):3280-94.

181. Bell E, Ivarsson B, Merrill C. Production of a tissue-like structure by contraction of collagen lattices by human fibroblasts of different proliferative potential in vitro. Proceedings of the National Academy of Sciences of the United States of America. 1979;76(3):1274-8.

182. Reed MJ, Vernon RB, Abrass IB, Sage EH. TGF-beta 1 induces the expression of type I collagen and SPARC, and enhances contraction of collagen gels, by fibroblasts from young and aged donors. J Cell Physiol. 1994;158(1):169-79.

183. Mio T, Liu XD, Adachi Y, Striz I, Skold CM, Romberger DJ, et al. Human bronchial epithelial cells modulate collagen gel contraction by fibroblasts. The American journal of physiology. 1998;274(1 Pt 1):L119-26.

184. Nishiyama T, Tominaga N, Nakajima K, Hayashi T. Quantitative evaluation of the factors affecting the process of fibroblast-mediated collagen gel contraction by separating the process into three phases. Coll Relat Res. 1988;8(3):259-73.

185. Desmouliere A, Geinoz A, Gabbiani F, Gabbiani G. Transforming growth factor-beta 1 induces alpha-smooth muscle actin expression in granulation tissue myofibroblasts and in quiescent and growing cultured fibroblasts. J Cell Biol. 1993;122(1):103-11.

186. Abe R, Donnelly SC, Peng T, Bucala R, Metz CN. Peripheral blood fibrocytes: differentiation pathway and migration to wound sites. J Immunol. 2001;166(12):7556-62.

187. Wilson SE, He YG, Lloyd SA. EGF, EGF receptor, basic FGF, TGF beta-1, and IL-1 alpha mRNA in human corneal epithelial cells and stromal fibroblasts. Investigative ophthalmology & visual science. 1992;33(5):1756-65.

188. Cillo JE, Jr., Gassner R, Koepsel RR, Buckley MJ. Growth factor and cytokine gene expression in mechanically strained human osteoblast-like cells: implications for distraction osteogenesis. Oral Surg Oral Med Oral Pathol Oral Radiol Endod. 2000;90(2):147-54.

189. Khalil N, Bereznay O, Sporn M, Greenberg AH. Macrophage production of transforming growth factor beta and fibroblast collagen synthesis in chronic pulmonary inflammation. J Exp Med. 1989;170(3):727-37.

190. Hinz B, Mastrangelo D, Iselin CE, Chaponnier C, Gabbiani G. Mechanical tension controls granulation tissue contractile activity and myofibroblast differentiation. The American journal of pathology. 2001;159(3):1009-20.

191. Christiansen DL, Huang EK, Silver FH. Assembly of type I collagen: fusion of fibril subunits and the influence of fibril diameter on mechanical properties. Matrix Biol. 2000;19(5):409-20.

192. Vernon RB, Angello JC, Iruela-Arispe ML, Lane TF, Sage EH. Reorganization of basement membrane matrices by cellular traction promotes the formation of cellular networks in vitro. Lab Invest. 1992;66(5):536-47.

193. Hara M, Nakashima M, Fujii T, Uehara K, Yokono C, Hashizume R, et al. Construction of collagen gel scaffolds for mechanical stress analysis. Biosci Biotechnol Biochem. 2014;78(3):458-61.

194. Leung BM, Moraes C, Cavnar SP, Luker KE, Luker GD, Takayama S. Microscale 3D collagen cell culture assays in conventional flat-bottom 384-well plates. J Lab Autom. 2015;20(2):138-45.

195. Chung S, Sudo R, Vickerman V, Zervantonakis IK, Kamm RD. Microfluidic Platforms for Studies of Angiogenesis, Cell Migration, and Cell-Cell Interactions. Ann Biomed Eng. 2010;38(3):1164-77.

196. Huang GY, Zhou LH, Zhang QC, Chen YM, Sun W, Xu F, et al. Microfluidic hydrogels for tissue engineering. Biofabrication. 2011;3(1).

197. Cubaud T, Mason TG. Capillary threads and viscous droplets in square microchannels. Phys Fluids. 2008;20(5).

198. Ma SH, Natoli M, Liu X, Neubauer MP, Watt FM, Fery A, et al. Monodisperse collagen-gelatin beads as potential platforms for 3D cell culturing. J Mater Chem B. 2013;1(38):5128-36.

199. Hong SM, Hsu HJ, Kaunas R, Kameoka J. Collagen microsphere production on a chip. Lab on a chip. 2012;12(18):3277-80.

200. Yamada M, Hori A, Sugaya S, Yajima Y, Utoh R, Yamato M, et al. Cell-sized condensed collagen microparticles for preparing microengineered composite spheroids of primary hepatocytes. Lab on a chip. 2015;15(19):3941-51.

201. Liu F, Mih JD, Shea BS, Kho AT, Sharif AS, Tager AM, et al. Feedback amplification of fibrosis through matrix stiffening and COX-2 suppression. J Cell Biol. 2010;190(4):693-706.

202. Epa AP, Thatcher TH, Pollock SJ, Wahl LA, Lyda E, Kottmann RM, et al. Normal Human Lung Epithelial Cells Inhibit Transforming Growth Factor-beta Induced Myofibroblast Differentiation via Prostaglandin E2. PLoS One. 2015;10(8):e0135266.

203. Ulrich TA, Lee TG, Shon HK, Moon DW, Kumar S. Microscale mechanisms of agarose-induced disruption of collagen remodeling. Biomaterials. 2011;32(24):5633-42.

204. Li B, Wang JH. Fibroblasts and myofibroblasts in wound healing: force generation and measurement. J Tissue Viability. 2011;20(4):108-20.

205. Wang JH, Lin JS. Cell traction force and measurement methods. Biomech Model Mechanobiol. 2007;6(6):361-71.

206. Harley BA, Freyman TM, Wong MQ, Gibson LJ. A new technique for calculating individual dermal fibroblast contractile forces generated within collagen-GAG scaffolds. Biophysical journal. 2007;93(8):2911-22.

207. Jin T, Li L, Siow RC, Liu KK. A novel collagen gel-based measurement technique for quantitation of cell contraction force. J R Soc Interface. 2015;12(106).

208. Delvoye P, Wiliquet P, Leveque JL, Nusgens BV, Lapiere CM. Measurement of mechanical forces generated by skin fibroblasts embedded in a three-dimensional collagen gel. J Invest Dermatol. 1991;97(5):898-902.

209. Asmani M, Velumani S, Li Y, Wawrzyniak N, Hsia I, Chen Z, et al. Fibrotic microtissue array to predict anti-fibrosis drug efficacy. Nat Commun. 2018;9(1):2066.

210. Agarwal A, Coleno ML, Wallace VP, Wu WY, Sun CH, Tromberg BJ, et al. Two-photon laser scanning microscopy of epithelial cell-modulated collagen density in engineered human lung tissue. Tissue Eng. 2001;7(2):191-202.

211. Bravo DDC-R, T.; Chen, J.; Wang, J. An impedance-based cell contraction assay using human primary smooth muscle cells and fibroblasts. Journal of Pharmacological and Toxicological Methods. 2018;89:47-53.

212. Xu Q, Norman JT, Shrivastav S, Lucio-Cazana J, Kopp JB. In vitro models of TGF-beta-induced fibrosis suitable for high-throughput screening of antifibrotic agents. Am J Physiol Renal Physiol. 2007;293(2):F631-40.

213. Hu Q, Noor M, Wong YF, Hylands PJ, Simmonds MS, Xu Q, et al. In vitro anti-fibrotic activities of herbal compounds and herbs. Nephrol Dial Transplant. 2009;24(10):3033-41.

214. Chen CZ, Peng YX, Wang ZB, Fish PV, Kaar JL, Koepsel RR, et al. The Scar-in-a-Jar: studying potential antifibrotic compounds from the epigenetic to extracellular level in a single well. British journal of pharmacology. 2009;158(5):1196-209.

215. Hecker L, Logsdon NJ, Kurundkar D, Kurundkar A, Bernard K, Hock T, et al. Reversal of persistent fibrosis in aging by targeting Nox4-Nrf2 redox imbalance. Sci Transl Med. 2014;6(231):231ra47.

216. Yanai H, Shteinberg A, Porat Z, Budovsky A, Braiman A, Ziesche R, et al. Cellular senescence-like features of lung fibroblasts derived from idiopathic pulmonary fibrosis patients. Aging (Albany NY). 2015;7(9):664-72.

217. Mora AL, Rojas M, Pardo A, Selman M. Emerging therapies for idiopathic pulmonary fibrosis, a progressive age-related disease. Nat Rev Drug Discov. 2017;16(11):810.

218. Barkauskas CE, Noble PW. Cellular mechanisms of tissue fibrosis. 7. New insights into the cellular mechanisms of pulmonary fibrosis. Am J Physiol Cell Physiol. 2014;306(11):C987-96.

219. Campbell JD, McDonough JE, Zeskind JE, Hackett TL, Pechkovsky DV, Brandsma CA, et al. A gene expression signature of emphysema-related lung destruction and its reversal by the tripeptide GHK. Genome Med. 2012;4(8):67.

220. Cui H, Banerjee S, Xie N, Ge J, Liu RM, Matalon S, et al. MicroRNA-27a-3p Is a Negative Regulator of Lung Fibrosis by Targeting Myofibroblast Differentiation. American journal of respiratory cell and molecular biology. 2016;54(6):843-52.

221. Jin J, Togo S, Kadoya K, Tulafu M, Namba Y, Iwai M, et al. Pirfenidone attenuates lung fibrotic fibroblast responses to transforming growth factor-beta1. Respir Res. 2019;20(1):119.

222. Singh S, Tavana H. Collagen Partition in Polymeric Aqueous Two-Phase Systems for Tissue Engineering. Front Chem. 2018;6:379.

223. Rangarajan S, Kurundkar A, Kurundkar D, Bernard K, Sanders YY, Ding Q, et al. Novel Mechanisms for the Antifibrotic Action of Nintedanib. American journal of respiratory cell and molecular biology. 2016;54(1):51-9.